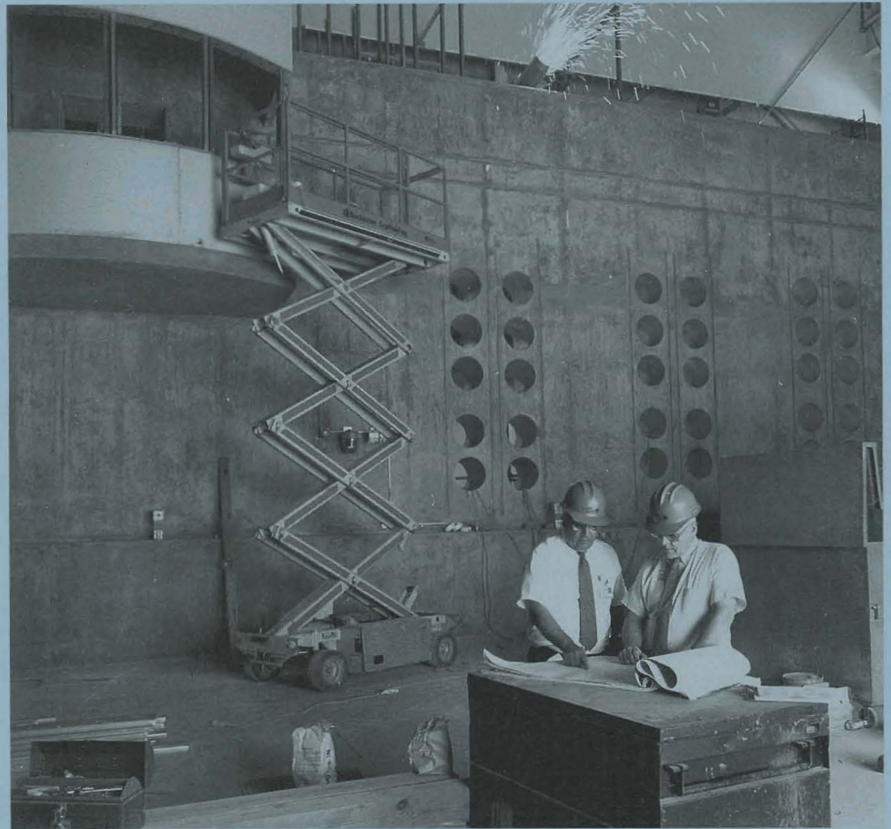


# LLE Review

## Quarterly Report



**April–June 1993**



Laboratory for Laser Energetics  
College of Engineering and Applied Science  
University of Rochester  
250 East River Road  
Rochester, New York 14623-1299

# LLE Review

## Quarterly Report

*Editor:* R. J. Hutchison  
(716) 275-5772

**April–June 1993**

---

Laboratory for Laser Energetics  
College of Engineering and Applied Science  
University of Rochester  
250 East River Road  
Rochester, New York 14623-1299



This report was prepared as an account of work conducted by the Laboratory for Laser Energetics and sponsored by New York State Energy Research and Development Authority, the University of Rochester, the U.S. Department of Energy, and other agencies.

Neither the above named sponsors, nor any of their employees, makes any warranty, expressed or implied, or assumes any legal liability or responsibility for the accuracy, completeness, or usefulness of any information, apparatus, product, or process disclosed, or represents that its use would not infringe privately owned rights.

Reference herein to any specific commercial product, process, or service by trade name, mark, manufacturer, or otherwise, does not necessarily constitute or imply its endorsement, recommendation, or favoring by the United States Government or any agency thereof or any other sponsor.

Results reported in the LLE Review should not be taken as necessarily final results as they represent active research. The views and opinions of authors expressed herein do not necessarily state or reflect those of any of the above sponsoring entities.

## IN BRIEF

This volume of the LLE Review, covering the period April–June 1993, contains articles on spectral features from argon-filled target implosions on OMEGA, and on the theory of an implicit difference scheme for the Fokker-Planck equation. The advanced technology section includes reports on a novel polymer liquid-crystal wave plate and a new scheme for phase conversion of the OMEGA Upgrade beams that results in greater, smoother energy deposition on fusion targets. Finally, reports on the as-designed configuration of the OMEGA Upgrade and on the newly configured glass development laser system are summarized.

Highlights of the research reported in this issue are

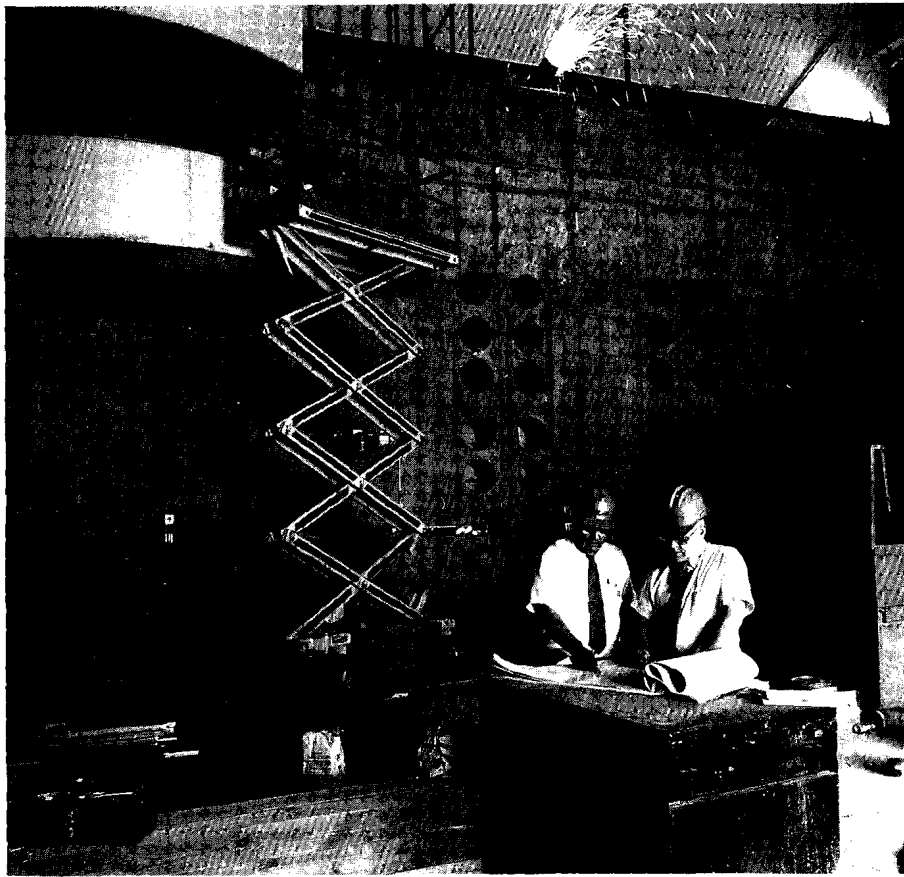
- The theoretical approach to a new, implicit, conservative finite-difference scheme for the Fokker-Planck equation, relating to Coulomb collisions between particles in a plasma is presented. This scheme provides an increase in computational efficiency by using time steps much larger than the thermal collision times, which simulate plasmas far from thermal equilibrium.
- Two types of target fills were used on the concluding series of OMEGA experiments prior to shutdown for the Upgrade: low-pressure argon mixed with deuterium and high-pressure argon. The results of these experiments are presented, showing new diagnostic features in the x-ray spectra produced by the implosions. The low-pressure implosions yielded

information on the peak core conditions, such as electron temperature and core density, while the high-pressure implosions yielded information on the cooler, peripheral layer of the core, such as its  $\rho\Delta R$ .

- A novel phase-conversion technique was developed using a Fourier grating as an optical kinoform. This technique has the advantage of providing very smooth beam profiles on a range of target planes, while avoiding the lossy sidelobes associated with two-level phase plates previously used on OMEGA.
- Liquid-crystal polarizer and wave-plate technology has been frequently reported in past LLE Reviews. This issue highlights a nematic *polymer* liquid-crystal wave-plate design for use at 1054 nm with high laser-damage threshold and potentially low cost. A single-substrate design, with very-low-cost possibility, is also presented.

# CONTENTS

	<i>Page</i>
IN BRIEF .....	iii
CONTENTS .....	v
Section 1 PROGRESS IN LASER FUSION .....	121
1.A Implicit and Conservative Difference Scheme for the Fokker-Planck Equation .....	121
1.B New Diagnostic Features in the Spectra of Recent Argon-Filled-Target Implosions on OMEGA .....	134
Section 2 ADVANCED TECHNOLOGY DEVELOPMENTS .....	146
2.A Phase Conversion of Lasers with Low-Loss Distributed Phase Plates .....	146
2.B Nematic Polymer Liquid-Crystal Wave Plate for High-Power Lasers at 1054 nm .....	157
Section 3 LASER SYSTEM REPORT .....	178
3.A GDL Facility Report .....	178
3.B The Upgrade to the OMEGA Laser System .....	179
PUBLICATIONS AND CONFERENCE PRESENTATIONS	



Stephen Loucks, Administrative Director of LLE and Manager of the OMEGA Upgrade building project, and Nelson Principio, Deputy OMEGA Upgrade Project Manager, discuss building plans in front of the new OMEGA Upgrade shield wall in the target bay. The shield wall, comprised of two million pounds of cement, is complete. Building construction is scheduled to be completed in August 1993, allowing LLE staff to continue with component integration for the OMEGA Upgrade.

# Section 1

## PROGRESS IN LASER FUSION

### 1.A Implicit and Conservative Difference Scheme for the Fokker-Planck Equation

The Fokker-Planck (FP) equation plays an important role in the investigation of electron transport processes in laser-produced plasmas.<sup>1,2</sup> Much of the progress in the numerical solution of the FP equation has been possible following the pioneering work of Chang and Cooper.<sup>3</sup> They proposed a practical differencing scheme that preserved particle number and allowed the distribution function to evolve through a series of quasi-equilibria, while maintaining positivity at all energy groups.

Recently, however, Larsen *et al.*<sup>4</sup> showed that although the Chang-Cooper scheme works well for linear problems, such as the scattering of test particles, it sometimes fails for general nonlinear problems involving the evolution of distribution functions far from equilibrium. Larsen *et al.*<sup>4</sup> generalized the Chang-Cooper method to allow for a more efficient solution of the nonlinear FP equation using larger time steps. Unfortunately, their approach relies on having analytic expressions for the collision coefficients, which are not generally available.

One important property of the FP equation not addressed by the above authors is energy conservation. Langdon<sup>5</sup> introduced this property to the Chang-Cooper scheme, for Coulomb scattering between like particles, by appropriately differencing the collision coefficients. This modification has been successfully tested by Kho<sup>6</sup> and found to ensure adequate energy conservation provided the distribution function does not change substantially over one time step.<sup>2</sup> For modeling thermal-transport problems in laser-produced plasmas, Epperlein *et al.*<sup>1</sup> found that energy conservation could be further improved through a

“predictor” step, whereby the collision coefficients are estimated by linearly extrapolating the distribution function in time. Berezin *et al.*<sup>7</sup> developed further numerical schemes that conserved not only particle energy and density but also maximized entropy. Unfortunately, their methods rely on explicit time integration and are thus of limited practical use.

In this article we develop a fully implicit finite-difference method for solving the FP equation for like-particle collisions in plasma that conserves both energy and number density *exactly*. The essence of our approach is to first linearize the FP equation, with the collision coefficients as defined by Langdon, and then apply the Chang-Cooper approach to difference the equation in velocity space. The conservative properties of the scheme are illustrated by considering the standard test problem<sup>6</sup> of the thermalization of a nearly monoenergetic electron distribution in a homogeneous plasma. It is shown that, whereas the conventional scheme is limited by energy conservation to time steps no larger than about 100 thermal collision times, there is no such limitation with the new scheme.

Although the numerical solution of the finite-difference equation in our proposed scheme requires the inversion of a full matrix rather than a tridiagonal matrix,<sup>3</sup> the relaxation in time-step constraints can sometimes far outweigh the extra computational effort. This is demonstrated by simulating the evolution of a laser-produced plasma using the *SPARK* FP code,<sup>1,2</sup> where we typically gain factors of greater than ten in computational speed.

In the next section the FP equation is described, and its basic conservation properties are reviewed. Then the numerical scheme is developed, and the test problem of electron thermalization in a homogeneous plasma is presented. In the last two sections we describe simulations of laser-produced plasmas using an FP code and summarize the main conclusions.

### The Fokker-Planck Equation and Its Conservation Properties

The FP equation describing Coulomb collisions of like particles in a homogeneous, fully ionized plasma is given by

$$\tau \frac{\partial f}{\partial t} = \frac{v_t^3}{N_0 v^2} \frac{\partial}{\partial v} \left[ C(f) + D(f) \frac{\partial}{\partial v} \right] f \equiv F(f), \quad (1)$$

where  $f(v, t)$  is the normalized particle distribution function, such that

$$N_0 = \int_0^{\infty} dv v^2 f(v, t = 0)$$

is the initial number density. The collision time between thermal particles is defined by

$$\tau = v_t^3 / \left[ 4\pi N_0 (e^2 / m)^2 \ln \Lambda \right],$$

where  $v_t = (T_0 / m)^{1/2}$  is the thermal velocity,  $T_0$  is the initial temperature,  $e$  is the charge,  $m$  is the mass, and  $\ln \Lambda$  is the Coulomb logarithm. The collision coefficients, describing friction and diffusion, are given by<sup>8</sup>

$$C(f) = \int_0^v duu^2 f(u, t) \quad (2)$$

and

$$D(f) = \frac{1}{3v} \int_0^v duu^4 f(u, t) + \frac{v^2}{3} \int_v^\infty duuf(u, t), \quad (3)$$

respectively. The equilibrium solution of Eq. (1) is a Maxwellian,  $f_M = (2/\pi)^{1/2} (N_0/v_i^3) \exp(-v^2/2v_i^2)$ .

Since the particle number density is

$$N(t) = \int_0^\infty dvv^2 f(v, t), \quad (4)$$

we can readily establish its conservation by taking the  $\int_0^\infty dvv^2$  moment of Eq. (1). This gives us

$$\tau \frac{\partial N}{\partial t} = \frac{v_i^3}{N_0} \left[ C(f)f + D(f) \frac{\partial f}{\partial v} \right] \Big|_0^\infty, \quad (5)$$

where the appropriate boundary conditions on  $f$  are that  $[Cf + D(\partial f/\partial v)]$  vanishes at  $v = 0$  and  $\infty$ .

Energy conservation can be verified by taking the  $(1/2)m \int_0^\infty dvv^4$  moment of Eq. (1), i.e.,

$$\tau \frac{\partial E}{\partial t} = \frac{1}{2} m \int_0^\infty dvv^4 F(f) = \frac{1}{2} m \int_0^\infty dvv^4 \left\{ \frac{v_i^3}{N_0 v^2} \frac{\partial}{\partial v} \left[ C(f)f + D(f) \frac{\partial f}{\partial v} \right] \right\}, \quad (6)$$

where  $E [= (3/2)NT]$  is the energy density. Integrating Eq. (6) by parts, and using the fact  $(vDf)$  vanishes at  $v = 0$  and  $\infty$ , we obtain

$$\tau \frac{\partial E}{\partial t} \propto - \int_0^\infty dvv \left( Cf + D \frac{\partial f}{\partial v} \right) = - \int_0^\infty dv \left[ vCf - \frac{\partial(vD)}{\partial v} f \right]. \quad (7)$$

From Eq. (2) and rewriting Eq. (3) as

$$\frac{\partial}{\partial v} (vD) = v^2 \int_v^\infty duuf, \quad (8)$$

we then have

$$\tau \frac{\partial E}{\partial t} \propto - \int_0^{\infty} dv \left[ v C f - \frac{\partial(vD)}{\partial v} f \right] = - \int_0^{\infty} dv v f(v) \int_0^v du u^2 f(u) + \int_0^{\infty} dv v^2 f(v) \int_v^{\infty} du u f(u). \quad (9)$$

By recognizing that the two double integrals on the right-hand side of this equation are identical, we thus have energy conservation.

### The Numerical Scheme

The conventional approach for solving Eq. (1) is to discretize in time such that  $\Delta t = (t^{n+1} - t^n)$  and use  $\partial f / \partial t \approx (f^{n+1} - f^n) / \Delta t$  to obtain<sup>3</sup>

$$\tau \frac{(f^{n+1,i+1} - f^n)}{\Delta t} = \frac{v_i^3}{N_0 v^2} \frac{\partial}{\partial v} \left( C^{n+1,i} f^{n+1,i+1} + D^{n+1,i} \frac{\partial f^{n+1,i+1}}{\partial v} \right), \quad (10)$$

where  $i = 0, \dots, I$  is an iteration index. At the beginning of each iteration, the nonlinear coefficients are then calculated with either  $f^{n+1,i=0} = f^n$  or  $f^{n+1,i=0} = 2f^n - f^{n-1}$  (i.e., a predictor step). However, as will be shown later, such iterative methods can lead to large energy-conservation errors when  $\Delta t \gg \tau$  for plasmas far from thermal equilibrium.

In this article we develop a noniterative, fully implicit method for solving Eq. (1) that conserves energy exactly for arbitrary values of  $\Delta t$ . The first step involves expanding  $F(f)$  by a truncated Taylor series,<sup>9</sup>

$$F^{n+1} = F^n + \left( \frac{\partial F}{\partial f} \right)^n (f^{n+1} - f^n) + O(\Delta t^2). \quad (11)$$

Substituting this equation back into Eq. (1), we then obtain

$$\left[ \frac{\tau}{\Delta t} - \left( \frac{\partial F}{\partial f} \right)^n \right] (f^{n+1} - f^n) = F^n, \quad (12)$$

where

$$\left( \frac{\partial F}{\partial f} \right)^n f^n = 2 F^n$$

and

$$\left( \frac{\partial F}{\partial f} \right)^n f^{n+1} = \frac{v_i^3}{N_0 v^2} \frac{\partial}{\partial v} \left( C^n f^{n+1} + D^n \frac{\partial f^{n+1}}{\partial v} \right) + \frac{v_i^3}{N_0 v^2} \frac{\partial}{\partial v} \left( C^{n+1} f^n + D^{n+1} \frac{\partial f^n}{\partial v} \right). \quad (13)$$

(a)

(b)

Here, we identify terms (a) and (b) as differential and integral operators on  $f^{n+1}$ , respectively. They represent the time rate of change of  $f$  resulting from the distribution of (a) test and (b) field particles at  $t^{n+1}$ . By neglecting the more cumbersome term (b), Eq. (12) reduces to Eq. (10) with  $C^{n+1,i} = C^n$  and  $D^{n+1,i} = D^n$ . However, even though terms (a) and (b) individually conserve number density, we will now show that term (b) is essential to ensure overall energy conservation.

Taking the  $(1/2)m \int_0^\infty dvv^4$  moment of Eq. (12), we find that

$$\frac{\tau}{\Delta t} (E^{n+1} - E^n) - \frac{1}{2} m \int_0^\infty dvv^4 \left( \frac{\partial F}{\partial f} \right)^n (f^{n+1} - f^n) = \frac{1}{2} m \int_0^\infty dvv^4 F^n. \quad (14)$$

Comparing Eq. (14) with Eq. (6) and noting that  $(\partial F / \partial f)^n f^n = 2F^n$  and  $\int_0^\infty dvv^4 F = 0$ , we are left with

$$\frac{\tau}{\Delta t} (E^{n+1} - E^n) = \frac{1}{2} m \int_0^\infty dvv^4 \left( \frac{\partial F}{\partial f} \right)^n f^{n+1}, \quad (15)$$

which can then be expanded (using the techniques described earlier) to

$$\frac{\tau}{\Delta t} (E^{n+1} - E^n) \propto - \int_0^\infty dvv f^{n+1}(v) \int_0^v duu^2 f^n(u) + \int_0^\infty dvv f^n(v) \int_0^v duu^2 f^{n+1}(u) \quad (a) \quad (16)$$

$$- \int_0^\infty dvv f^n(v) \int_0^v duu^2 f^{n+1}(u) + \int_0^\infty dvv f^{n+1}(v) \int_0^v duu^2 f^n(u) = 0. \quad (b)$$

Once again, terms (a) and (b) correspond to the differential and integral operators, as in Eq. (13). These terms cancel each other out and lead to exact energy conservation for arbitrary values of  $f^n$  and  $f^{n+1}$ . We do recall, however, that number-density conservation does not require the use of term (b).<sup>3</sup>

Our remaining task is to difference Eq. (12) in velocity space. We introduce  $f_j = f(v_j)$ , where the index  $j = 1, \dots, J$  denotes a cell center. The cell boundaries are defined by  $v_{j+1/2} = (v_j + v_{j+1})/2$ , where  $v_{1/2} = 0$  and  $v_{J+1/2} = v_{\max}$ , and the cell sizes (not necessarily uniform) are given by  $\Delta v_j = (v_{j+1/2} - v_{j-1/2})$  and  $\Delta v_{j+1/2} = (v_{j+1} - v_j)$ . Equation (12) now becomes (using the convention of summing over repeated indices)

$$\left[ \frac{\tau}{\Delta t} \delta_{jk} - \left( \frac{\partial F}{\partial f} \right)_{jk}^n \right] (f^{n+1} - f^n)_k = F_j^n, \quad (17)$$

where

$$\left(\frac{\partial F}{\partial f}\right)_{jk}^n = \frac{v_l^3}{N_0 v_j^2 \Delta v_j} (A_{jk}^n + B_{jk}^n). \quad (18)$$

The matrix elements, corresponding terms (a) and (b) of Eq. (13) are given, respectively, by

$$\begin{aligned} A_{jk}^n &= -\left(\frac{D_{j-1/2}^n}{\Delta v_{j+1/2}} + \frac{D_{j-1/2}^n}{\Delta v_{j-1/2}}\right) + C_{j+1/2}^n \delta_{j+1/2} - C_{j-1/2}^n (1 - \delta_{j-1/2}), \text{ for } j = k \\ &= \frac{D_{j+1/2}^n}{\Delta v_{j+1/2}} + C_{j+1/2}^n (1 - \delta_{j+1/2}), \text{ for } j+1 = k \\ &= \frac{D_{j-1/2}^n}{\Delta v_{j-1/2}} - C_{j-1/2}^n \delta_{j-1/2}, \text{ for } j-1 = k \\ &= 0, \text{ for } j-1 > k \text{ and } j+1 < k, \end{aligned}$$

and

$$\begin{aligned} B_{jk}^n &= \Delta v_j v_j^2 f_{j+1}^n + (\gamma_{j+1/2}^n - \gamma_{j-1/2}^n) \mu_j S_j, \text{ for } j = k \\ &= \mu_k \left[ \gamma_{j+1/2}^n \Delta v_j v_j^2 + (\gamma_{j+1/2}^n - \gamma_{j-1/2}^n) S_j \right], \text{ for } j < k \\ &= \Delta v_k v_k^2 \left[ f_{j+1/2}^n - f_{j-1/2}^n + (\gamma_{j+1/2}^n - \gamma_{j-1/2}^n) \delta_{k+1/2} v_{k+1/2} \Delta v_{k+1/2} \right] \\ &\quad + \mu_k (\gamma_{j+1/2}^n - \gamma_{j-1/2}^n) S_k, \text{ for } j > k, \end{aligned}$$

with

$$S_j = \sum_{l=1}^{j-1} \Delta v_l v_l^2, \quad \gamma_{j+1/2}^n = \frac{f_{j+1}^n - f_j^n}{v_{j+1/2} \Delta v_{j+1/2}}, \text{ and}$$

$$\mu_j = v_{j+1/2} \Delta v_{j+1/2} \delta_{j+1/2} + v_{j-1/2} \Delta v_{j-1/2} (1 - \delta_{j-1/2}).$$

Following the Chang-Cooper method, we use

$$f_{j+1/2} = (1 - \delta_{j+1/2})f_{j+1} + \delta_{j+1/2}f_j ,$$

where

$$\delta_{j+1/2} = \frac{1}{w_{j+1/2}} - \frac{1}{\exp(w_{j+1/2}) - 1}$$

and  $w_{j+1/2} = \Delta v_{j+1/2} C_{j+1/2} / D_{j+1/2}$ . This type of weighting has been designed to preserve positivity and provide the correct equilibrium solution for  $f$ .<sup>3</sup>

In order to comply with the energy-conservation relations discussed in this article, the collisional terms are calculated from Eqs. (2) and (8) as follows:<sup>5,6</sup>

$$C_{j+1/2} = \sum_{l=1}^j \Delta v_l v_l^2 f_l ,$$

$$(vD)_{j+1/2} = (vD)_{j-1/2} + \Delta v_j v_j^2 \sum_{l=j}^{J-1} \Delta v_{l+1/2} v_{l+1/2} f_{l+1/2} ,$$

and

$$(vD)_{3/2} = \Delta v_1 v_1^2 \sum_{l=1}^{J-1} \Delta v_{l+1/2} v_{l+1/2} f_{l+1/2} .$$

The appropriate boundary conditions give rise to

$$f_{1/2} C_{1/2} + \frac{D_{1/2}}{\Delta v_{1/2}} (f_2 - f_1) = f_{J+1/2} C_{J+1/2} + \frac{D_{J+1/2}}{\Delta v_{J+1/2}} (f_{J+1} - f_J) = 0 ,$$

$$\mu_1 = v_{3/2} \Delta v_{3/2} \delta_{3/2} , \quad \mu_J = v_{J-1/2} \Delta v_{J-1/2} (1 - \delta_{J-1/2}) ,$$

$$\gamma_{J+1/2} = 0 , \quad f_{J+1} = 0 , \quad \text{and} \quad f_{J+1/2} = 0 .$$

### Test Problem

We consider the thermalization of an approximately monoenergetic distribution of particles through small-angle Coulomb scattering. Figure 55.1 shows the typical evolution of such a distribution, obtained by solving Eq. (17). As expected from previous calculations (e.g., Ref. 5), the particles attain close to a Maxwellian distribution  $f_M$  of density  $N_0$  and temperature  $T_0$  in about five collision times.

For the case shown in Fig. 55.1, where the time step was taken to be  $0.1 \tau$ , both iterative and implicit approaches for solving the FP equation are found to be sufficiently accurate. So the question is—What happens to the solution when  $\Delta t \gg \tau$ ?

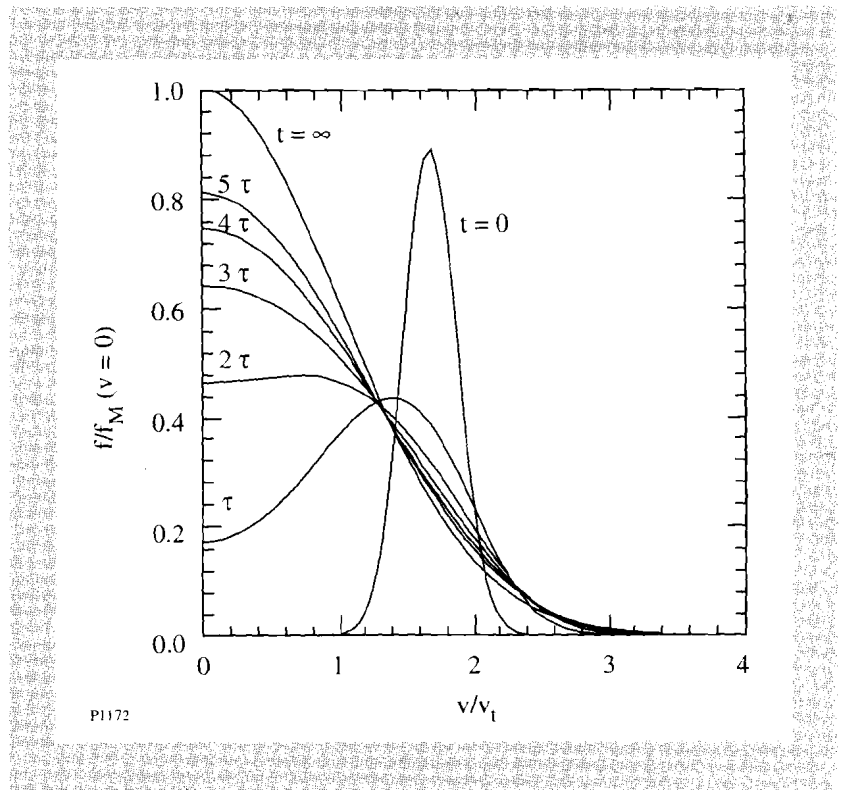


Fig. 55.1  
Plot of the distribution function  $f$  [normalized to  $f_M(v=0)$ ], as a function of velocity  $v$  (normalized to  $v_t$ ), at  $t = 0, \tau, 2\tau, 3\tau, 4\tau, 5\tau$ , and  $\infty$ .

Using the new implicit-conservative scheme we find that the distribution function evolves to the correct Maxwellian steady-state solution in about three time steps, while maintaining constant energy. With the iterative approach, however, the lack of exact energy conservation leads to Maxwellian distribution functions of different temperatures  $T$ . To characterize these results, we calculate the fractional temperature difference  $\left| \frac{T - T_0}{T_0} \right| \equiv \left| \frac{\delta T}{T_0} \right|$  as a function of  $\Delta t/\tau$ . These are plotted in Fig. 55.2, assuming either  $f^{n+1,i=0} = f^n$  or  $f^{n+1,i=0} = 2f^n - f^{n-1}$  (a predictor step). As observed, in the absence of further iterations and for  $\Delta t < 20\tau$ , considerable improvement can be achieved with the predictor step. For  $\Delta t > 20\tau$ , however, neither approach is satisfactory, and the predictor method leads to larger errors. In fact, for  $\Delta t \gg 100\tau$ , the predictor method has been found to produce negative distribution functions and numerical instabilities.

As expected, iterations are found to improve the accuracy of the solutions (see Fig. 55.2). These improvements, however, become less pronounced as  $\Delta t/\tau$  increases, and the energy errors still remain above 20% for  $\Delta t > 100\tau$ , even after ten iterations.

The results presented in Figs. 55.1 and 55.2 are not too sensitive to the initial spread in energy distribution about the most likely energy, though the closer the distribution is to equilibrium, the smaller the energy errors become.

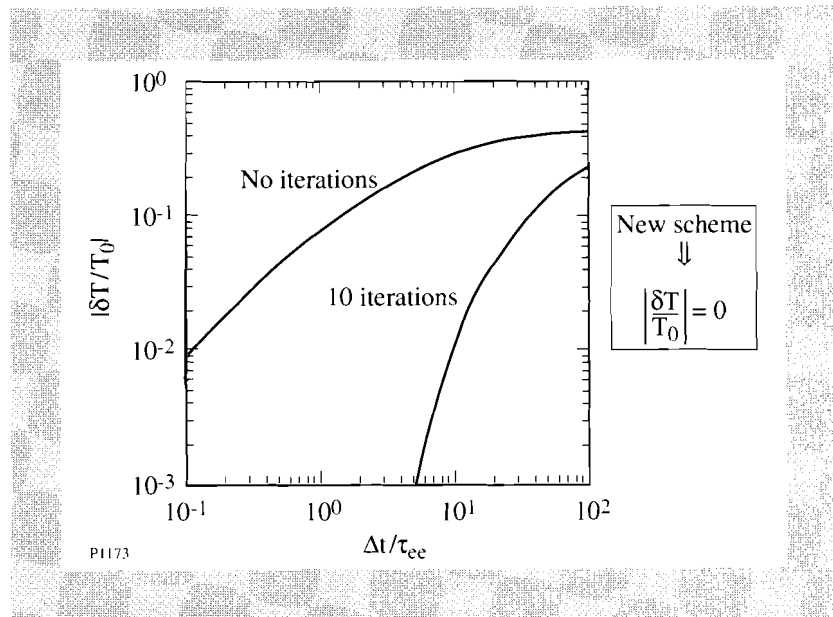


Fig. 55.2

Plot of fractional energy error  $|\delta T/T_0|$ , as a function of  $\Delta t/\tau$ , using either  $f^{n+1,i=0} = f^n$  (solid curves) or  $f^{n+1,i=0} = 2f^n - f^{n-1}$  (dashed curves), and with either no iteration ( $l = 0$ ) or ten iterations ( $l = 10$ ).

### Simulations of Laser-Produced Plasmas

The ablation of a target by a high-power laser, as envisaged in a laser-fusion scenario, has been routinely simulated using the *SPARK* FP code.<sup>1,2</sup> The code assumes fluid ions and solves for the electron-distribution function, including effects such as transport in configuration space, laser heating, and electron thermalization in velocity space. Since the last process is modeled by the same equation considered in this article, its method of solution can have an important impact on the computational efficiency of the code.

As discussed in the previous section, if the time step used in the code is much greater than  $\tau$  (where  $\tau = \tau_{ee}$  is now the thermal collision time between electrons), and the electron-distribution function is far from equilibrium, one might expect significant energy errors when using the standard iterative scheme for the electron-electron collision operator. To demonstrate this effect we simulate the evolution of a laser-produced plasma using *SPARK*.

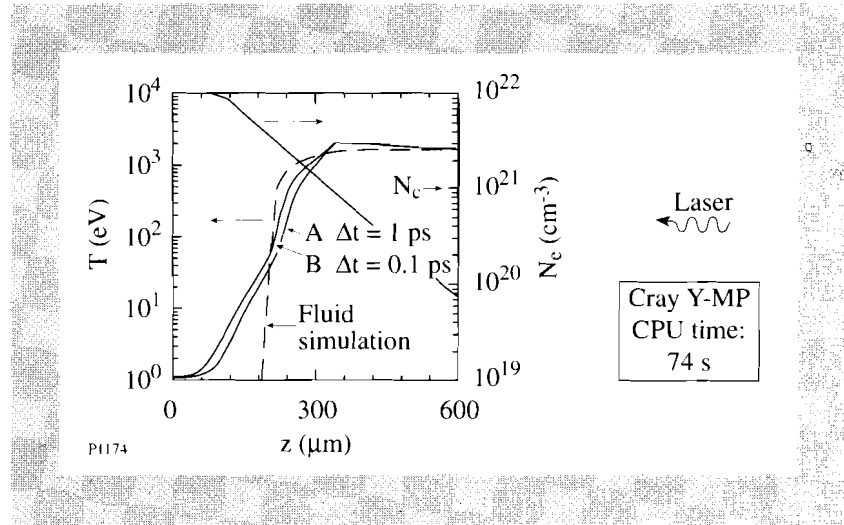
We first consider an idealized planar plasma of the type initially studied by Albritton.<sup>10</sup> The ions are assumed cold, immobile, and fully ionized, with an effective ionization number of  $Z = 10$ . Figure 55.3 shows the corresponding electron-number-density profile as a function of space  $z$ . A 1.06- $\mu\text{m}$  laser is incident from the right, with its energy being deposited via inverse-bremsstrahlung (up to the critical density,  $N_0 = N_c = 10^{21} \text{ cm}^{-3}$ ) at a constant intensity of  $10^{14} \text{ W/cm}^2$  over a period of 100 ps. Unlike Albritton, however, we assume a much lower initial electron temperature of 1 eV.

*SPARK* is run with 40 zones in  $z$  and 40 feathered zones in  $v$ , such that  $\Delta v_{j+1} / \Delta v_j = 1.11$  and  $v_{\text{max}} = 200 v_r$ . Using the implicit-conservative scheme we find that a constant time step of 0.1 ps provides a converged solution for the thermal heat front (shown in Fig. 55.3). The overall CPU time for this simulation is 74 s on a Cray Y-MP. To highlight the nonlocal nature of the electron transport, Fig. 55.3 also plots the temperature profile (dashed curve) based on a fluid description of the energy equation, using the Spitzer-Härm heat flow formula.<sup>11</sup>

This shows certain well-known features of nonlocal transport,<sup>10,1</sup> such as inhibition of the main heat front and preheat due to long-mean-free-path electrons coming from the corona.

Fig. 55.3

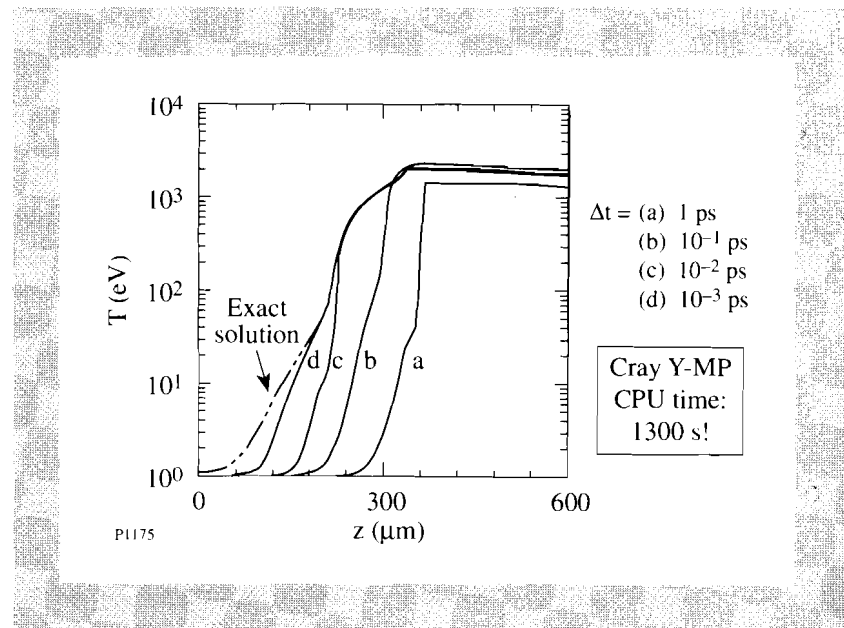
Plots of electron number density  $N$  (in  $\text{cm}^{-3}$ ) and temperature  $T$  (in eV), as functions of  $z$  (in  $\mu\text{m}$ ). Solid curves are obtained using the implicit-conservative scheme on SPARK, with (a)  $\Delta t = 1$  ps and (b)  $\Delta t = 0.1$  ps, and dashed curves are based on fluid model results. The critical density is identified by  $N_c$ .



The above simulations have been repeated using the conventional iterative method for the electron-electron collision operator. Figure 55.4 plots the resulting temperature profiles for  $\Delta t = 1, 10^{-1}, 10^{-2},$  and  $10^{-3}$  ps, assuming  $f^{n+1,i=0} = f^n$  (followed by one iteration). The corresponding CPU times are 1.3, 13, 130, and 1300 s. A comparison between Figs. 55.3 and 55.4 shows the slow convergence of the iterative scheme. This is specially true at high densities, where the preheat is occurring. Also, even though curve  $d$  (in Fig. 55.4) is not yet fully converged, it has already taken 18 times more computational effort than the corresponding curve  $b$  (in Fig. 55.3). The predictor scheme, which assumes that  $f^{n+1,i=0} = 2f^n - f^{n-1}$  (followed by one iteration), turns out to be impractical in this case since it leads to numerical instability for  $\Delta t > 10^{-3}$  ps.

Fig. 55.4

Plots of electron temperature  $T$  (in eV) as a function of  $z$  (in  $\mu\text{m}$ ). Results are based on the iterative scheme with one iteration and (a)  $\Delta t = 1$  ps, (b)  $\Delta t = 10^{-1}$  ps, (c)  $\Delta t = 10^{-2}$  ps, and (d)  $\Delta t = 10^{-3}$  ps (same conditions as in Fig. 55.3).



To understand the poor performance of the iterative scheme we must first realize that the electron-distribution function is far from a Maxwellian. This is shown in Fig. 55.5, which plots  $f$  as a function of electron kinetic energy  $(1/2)mv^2$  (in keV), corresponding to positions (A) and (B) in Fig. 55.3. Here we note the typical<sup>10</sup> double-Maxwellian nature of the electron distribution in the overdense region (A), where the “hot” tail shares the same temperature as the tail of the distribution at the critical density (B). Another important clue to the poor performance of the iterative scheme lies in the values of  $\tau_{ee}$ , which are plotted in Fig. 55.6 (for the same conditions as in Fig. 55.3). Together with the discussion in the “test problem” section, this figure shows why the convergence of the iterative scheme is so slow at high densities and low temperatures. Indeed, even for  $\Delta t = 10^{-3}$  ps, the high-density unheated plasma has a characteristic  $\tau_{ee} \sim 0.01 \Delta t$ .

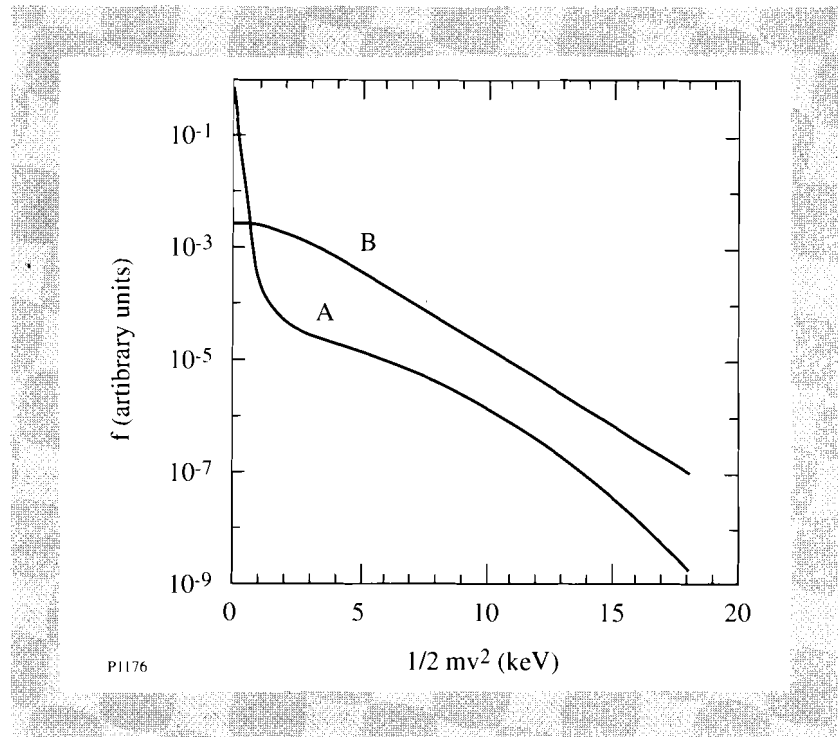


Fig. 55.5  
Plots of  $f$  (in arbitrary units) as a function of electron kinetic energy  $(1/2)mv^2$  (in keV). Curves correspond to positions A and B in Fig. 55.3.

To test the implicit-conservative scheme under less-idealized plasma conditions, we now consider the recent Rayleigh-Taylor experiments performed at Lawrence Livermore National Laboratories using the NOVA laser.<sup>12</sup> We attempt to model their plasma conditions by simulating the evolution of a CH foil, illuminated by 530-nm laser light with 1-ns linear rise time followed by a 2-ns flat section, at an intensity of  $5 \times 10^{13}$  W/cm<sup>2</sup>.

Our initial conditions correspond to a fully ionized, 18-mm CH plasma at a temperature of 0.5 eV and an electron number density of  $3.38 \times 10^{23}$  cm<sup>-3</sup>. The code is run in one-dimensional planar geometry on a Lagrangian mesh, assuming cold fluid ions. The configuration space mesh uses 50 zones, and the velocity mesh uses 35 feathered zones (where the mesh size increases at a constant ratio,  $\Delta v_{j+1} / \Delta v_j = 1.11$ ) and  $v_{\max} = 280 v_I$ .

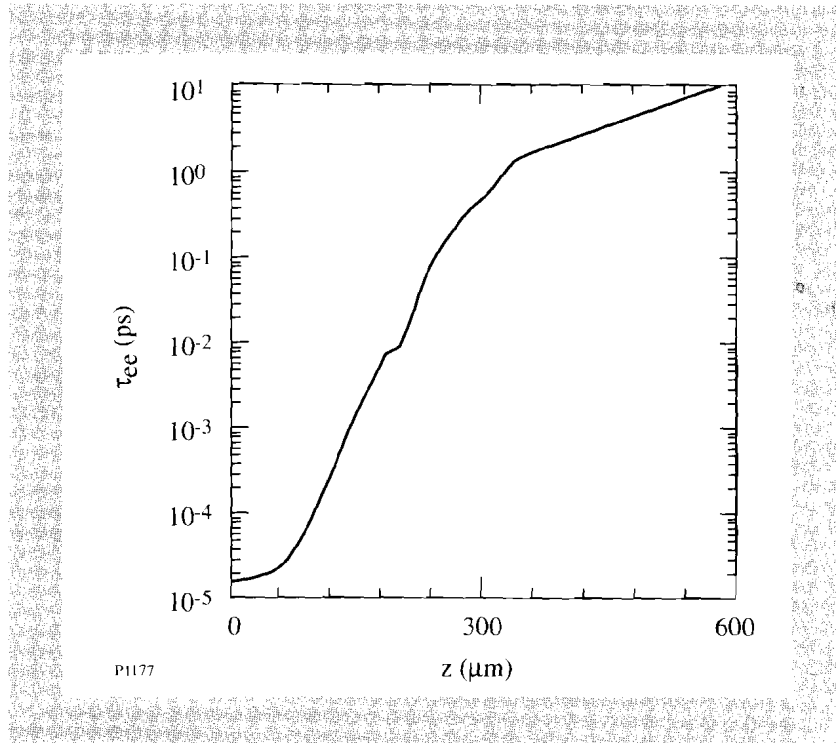


Fig. 55.6

Plot of  $\tau_{ee}$  (in picoseconds) as a function of  $z$  (in microns) (same conditions as in Fig. 55.3).

Figure 55.7 plots the electron temperature and number density as functions of space  $z$  at 3 ns. The implicit-conservative scheme has been used with a constant time step of 1 ps. The overall computation time of the simulation is 230 CPU sec on a Cray Y-MP.

In this case, to obtain a similarly accurate solution, the conventional iterative scheme (with one iteration) would require a prohibitively small time step of  $<10^{-5}$  ps. By using the predictor step (followed by one iteration), however, it has been possible to successfully reproduce the results in Fig. 55.7 with  $\Delta t = 0.01$  ps. (Unfortunately, this type of iterative scheme leads to numerical instabilities for  $\Delta t > 0.01$  ps.) This uses a total of 7200 CPU sec of computational time. So despite the fact that the implicit-conservative scheme requires three times more computational effort per  $\Delta t$ , the 100-fold increase in  $\Delta t$  has produced a 30-fold enhancement in computational speed.

It must be realized that many factors can affect the relative efficiency of using the implicit-conservative scheme. An obvious one is the value of  $\tau_{ee}$ , as demonstrated by the previous numerical simulations; another is the number of velocity groups  $J$ . Since the solution of Eq. (17) requires inversion of a full matrix rather than a tridiagonal matrix [as required by Eq. (10)], the computational effort scales approximately as  $J^2$  instead of  $J$ . This explains the larger computational effort (per time step) required by the implicit-conservative scheme. Although this can eventually limit the size of  $J$ , it is found that in practice one can alleviate this problem by judiciously feathering the velocity mesh (as done in the above simulations).

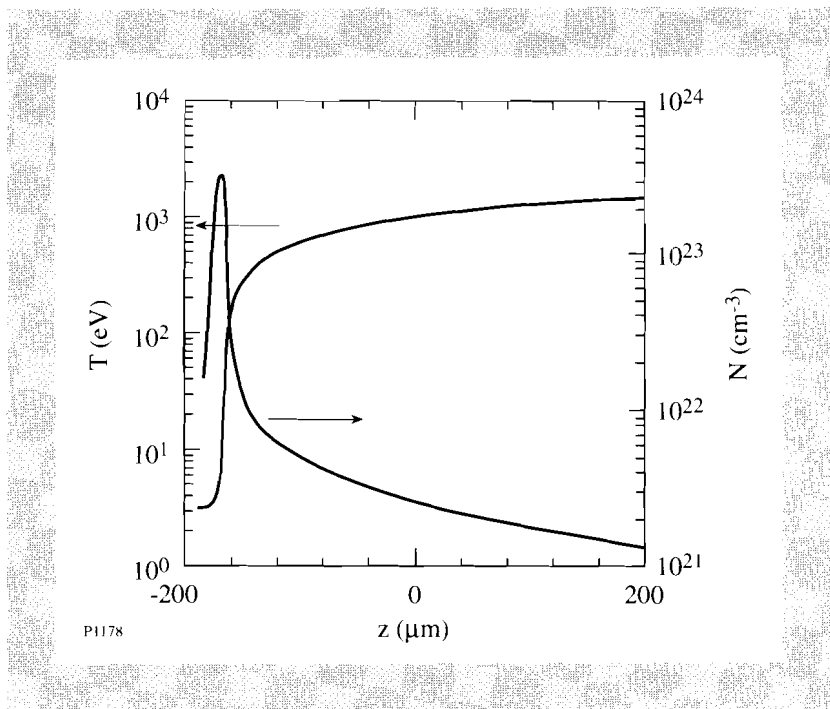


Fig. 55.7

Plots of electron number density  $N$  (in  $\text{cm}^{-3}$ ) and temperature  $T$  (in eV), as a function of  $z$  (relative to initial target position in microns), at  $t = 0$  and 3 ns. Results are obtained using the implicit-conservative scheme on *SPARK* with  $\Delta t = 1$  ps.

### Conclusions

In this article an implicit finite-difference scheme has been developed for solving the FP equation for like-particle collisions in plasmas. Unlike the currently available schemes, it enforces not only number-density conservation, but also exact-energy conservation. These properties have been demonstrated both analytically and numerically by considering the thermalization of an approximately monoenergetic distribution of particles. It is shown that even when the numerical integration time step is much larger than the thermal collision time, the correct steady-state solution is obtained. By comparison, numerical solutions based on conventional iterative approaches can yield unacceptably large energy errors.

The usefulness of the new implicit-conservative scheme has been demonstrated by implementing it in the laser-plasma transport code *SPARK*. Apart from improving the reliability of the code, the relaxation in time-step constraints has typically allowed for over an order of magnitude reduction in computational time.

### ACKNOWLEDGMENT

I wish to thank Dr. R. W. Short for many helpful discussions. This work was supported by the U.S. Department of Energy Office of Inertial Confinement Fusion under Cooperative Agreement No. DE-FC03-92SF19460, the University of Rochester, and the New York State Energy Research and Development Authority. The support of DOE does not constitute an endorsement by DOE of the views expressed in this article.

## REFERENCES

1. E. M. Epperlein, G. J. Rickard, and A. R. Bell, *Phys. Rev. Lett.* **61**, 2453 (1988); *Comput. Phys. Commun.* **52**, 7 (1988); E. M. Epperlein and R. W. Short, *Phys. Fluids B* **3**, 3092 (1991); **4**, 2211 (1992).
2. E. M. Epperlein, "Fokker-Planck Modeling of Electron Transport in Laser-Produced Plasmas" (to be published in *Laser and Particle Beams*).
3. J. S. Chang and G. Cooper, *J. Comput. Phys.* **6**, 1 (1970).
4. E. W. Larsen, C. D. Levermore, G. C. Pomraning, and J. G. Sanderson, *J. Comput. Phys.* **61**, 359 (1985).
5. A. B. Langdon, in *CECAM Report of Workshop on "The Flux Limiter and Heat Flow Instabilities in Laser-Fusion Plasmas"* (Universite Paris Sud, France, 1981), p. 69.
6. T. H. Kho, *Phys. Rev. A* **32**, 666 (1985).
7. Y. A. Berezin, V. N. Khudick, and M. S. Pekker, *J. Comput. Phys.* **69**, 163 (1987).
8. I. P. Shkarofsky, *Can. J. Phys.* **41**, 1753 (1963).
9. W. R. Briley and H. McDonald, *J. Comput. Phys.* **34**, 55 (1980).
10. J. R. Albritton, *Phys. Rev. Lett.* **50**, 2078 (1983).
11. L. Spitzer, Jr. and R. Härm, *Phys. Rev.* **89**, 977 (1953).
12. S. G. Glendenning *et al.*, *Phys. Rev. Lett.* **69**, 1201 (1992).

## 1.B New Diagnostic Features in the Spectra of Recent Argon-Filled-Target Implosions on OMEGA

Recent argon-filled-target implosions were performed for two kinds of target fills: (a) low-pressure argon in an Ar-DD mixture and (b) high-pressure argon. These experiments provide additional diagnostic signatures for comparison to code predictions. Generally, the measurements indicate deviations from predictions and can serve as indirect evidence of instability.

Targets of low argon-fill pressure have the distinction of low opacity of argon lines. This means that the observed line emission can yield information on the peak core conditions. In addition, we observe the free-bound continuum, which in high-pressure shots is indistinct due to opacity effects. This spectral feature provides additional information on the core electron temperature (through the continuum slope as well as the continuum jump) and on the core density (through the reduction in ionization energy).

Targets with high argon-fill pressure provide information on the cooler, peripheral argon layer of the core through the observation of absorption lines. In the past, absorption lines of 1s–2p transitions in argon ions with a partially filled *L* shell have been observed. Here, we also observe 1s–3p transitions in absorption. These lines provide information on the temperature and  $\rho\Delta R$  of that cooler region. However, the predicted strong absorption of helium-like argon lines has not been observed. This is interpreted as due to a cooler-than-predicted compressed core.

Table 55.I lists the experimental conditions for the shots used in the analysis. All targets were polymer shells, overcoated with a 0.05- $\mu\text{m}$  layer of Al (to protect against shinethrough), imploded by 600-ps OMEGA pulses. These shots were also part of an NLUF experiment performed by C. F. Hooper and colleagues from the University of Florida.

Table 55.I: Experimental conditions for the shots used in the analysis.

Shot No.	Target Diameter ( $\mu\text{m}$ )	Target Thickness ( $\mu\text{m}$ )	Fill Pressure		Laser Energy (J)
			DD (atm)	Ar (atm)	
24501	254	6	20	0.1	943
24498	248	6	0	20	976

### Low-Pressure Argon Experiments

Figure 55.8 shows the spectrum for shot 24501, emitted by a low-argon-pressure target. The argon lines are generally of low opacity for such low argon-fill pressure. We can predict this low opacity even without knowing the degree of target compression. To see that, we note that the opacity of a layer of areal density  $\rho\Delta R$  due to resonant line absorption is given by  $\tau_\nu = (\pi e^2 f / M_i mc) \rho\Delta R b P(\nu)$ , where  $\tau_\nu$  is the opacity at the frequency  $\nu$ ,  $f$  is the absorption oscillator strength,  $b$  is the fraction of all ions in the absorbing ground state,  $M_i$  is the ionic mass, and  $P(\nu)$  is the line profile in inverse-frequency units (normalized to unit area) at the frequency  $\nu$ . For Stark-broadened lines, the line width  $\Delta E$  is proportional to  $\rho^{2/3}$ , so that  $P(\nu) \sim \rho^{-2/3}$ . Strictly speaking, this is only true for the ion-broadening component of the profile; however, for lines like Lyman- $\beta$ , having no unshifted Stark component (hence, a central dip), this is practically true for the total profile. Since for a given target implosion  $\rho R = (3M / 4\pi)^{1/3} \rho^{2/3}$ , where  $M$  is the total argon mass, the line-center opacity depends only on the initial fill mass (or the fill pressure and radius) but not on the compression. For the Ar Lyman- $\beta$  line, the opacity at the two line peaks (straddling the central dip) becomes  $\tau_{\text{max}} \sim 0.1 b p^{1/3} R_0$ , where  $p$  is the fill pressure in atmospheres and  $R_0$  the initial radius in microns. For shot 24501, this becomes  $\tau_{\text{max}} \sim 2$ ; hence, opacity is small but not negligible.

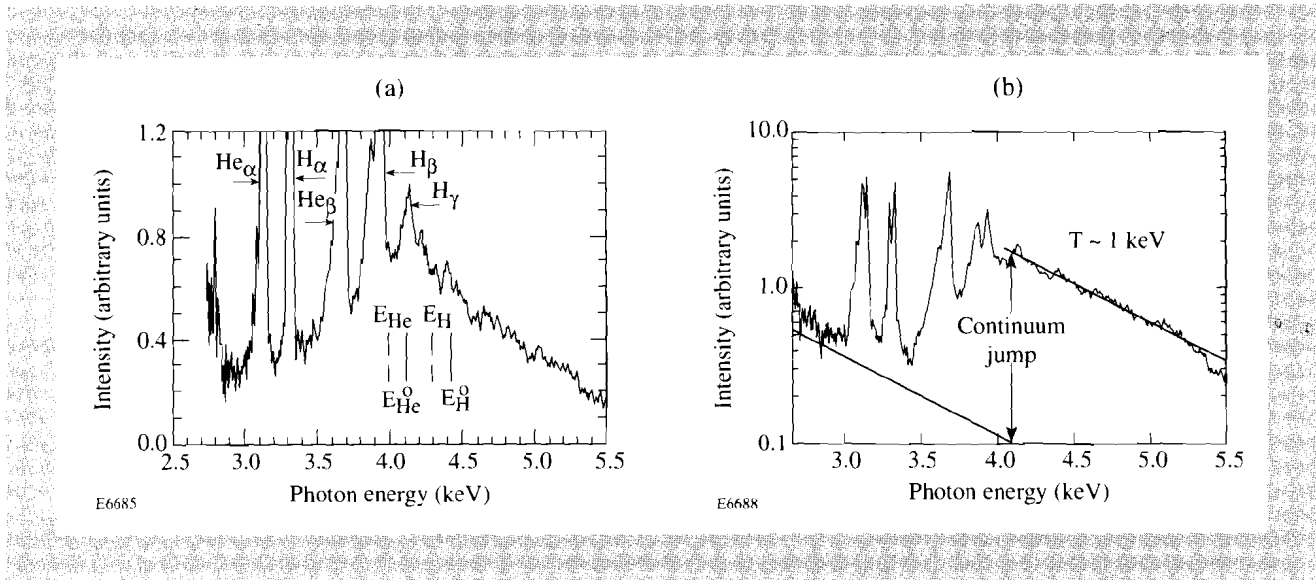


Fig. 55.8

Calibrated spectrum from a low-pressure argon target (shot 24501). The target was filled with a mixture of 0.1 atm argon and 20 atm deuterium. (a) The vertical bars show the unshifted positions of the hydrogen-like and helium-like  $K$  edges (o subscript), as well as the shifted positions, calculated from the experimentally determined density and temperature. H and He refer to  $\text{Ar}^{+17}$  and  $\text{Ar}^{+16}$ , respectively. (b) Determining the temperature from the continuum slope and a lower bound of the continuum jump (which yields an upper bound on the temperature). The line marking the continuum jump is arbitrarily placed near 4 keV.

We proceed to fitting theoretical Stark profiles calculated by Hooper<sup>1</sup> to the measured Lyman- $\beta$  profile of shot 24501, shown in Fig. 55.9. Note that these profiles correspond to the case of a very small admixture of argon in an otherwise deuterium plasma, as is the case in shot 24501. These profiles are somewhat narrower than the profiles for a pure argon plasma for the same electron density. For example, the simplified formula for the ion-broadening of hydrogenic lines<sup>2</sup> shows that for a given electron density, the linewidth is proportional to  $Z^{1/3}$ , where  $Z$  is the charge of the plasma ions (the perturbers). Before fitting to profiles of different densities, we show in Fig. 55.9(a) that Stark profiles are relatively insensitive to the temperature. The two Stark profiles shown are for the same electron density ( $N_e = 10^{23} \text{ cm}^{-3}$ ), but two different temperatures (200 and 800 eV). For an unknown temperature in the range of 200 to 800 eV, using a profile for an intermediate temperature, the deduced density can be in error of less than  $\pm 20\%$ . The Stark profile also depends slightly on the ion temperature (even before the Doppler broadening is folded in), and we used profiles calculated for  $T_i = T_e$ . Once we select a calculated profile closest to the measured one, final fitting is obtained by stretching or contracting the energy scale and noting that the profile width changes with density approximately like  $N_e^{2/3}$ . The Doppler broadening was also included in the calculated profiles. To account for the small opacity, we replace the actual profile  $P(\Delta E)$  by the expression  $1 - \exp[-\tau_{\text{max}} P(\Delta E) / P_{\text{max}}]$ , where  $P_{\text{max}}$  is the profile value at either peak and  $\tau_{\text{max}} = 2$ , as explained above. The best-fit profile corresponds to an electron density of  $0.7 \times 10^{24} \text{ cm}^{-3}$ , or  $\rho \sim 2.3 \text{ g cm}^{-3}$ . The assumed temperature for the theoretical profile was 1.0 keV, in anticipation of the results obtained below.

The spectrum in Fig. 55.8 provides an additional diagnostic feature, the free-bound continuum. Note that the intensity scale in Fig. 55.8(a) is linear, whereas in Fig. 55.8(b) it is logarithmic. This is the continuum due to recombination into the *K* shell, and it appears at energies above the *K* edge. There are two, close *K* edges here: (a) the  $\text{Ar}^{+17}$  edge, due to recombination of electrons and  $\text{Ar}^{+18}$  ions, at 4.426 keV, and (b) the  $\text{Ar}^{+16}$  edge, due to recombination of electrons and  $\text{Ar}^{+17}$  ions, at 4.120 keV. First, the electron temperature in the compressed core can be deduced from the slope of the free-bound continuum, which in Fig. 55.8(b) corresponds to  $T_e \sim 1.0$  keV. For the slope determination we look beyond the *K* edge of the first continuum ( $e^- + \text{Ar}^{+18}$ ), where the two continua simply add up. As described below, the edge is shifted into lower photon energies, which facilitates the slope measurement.

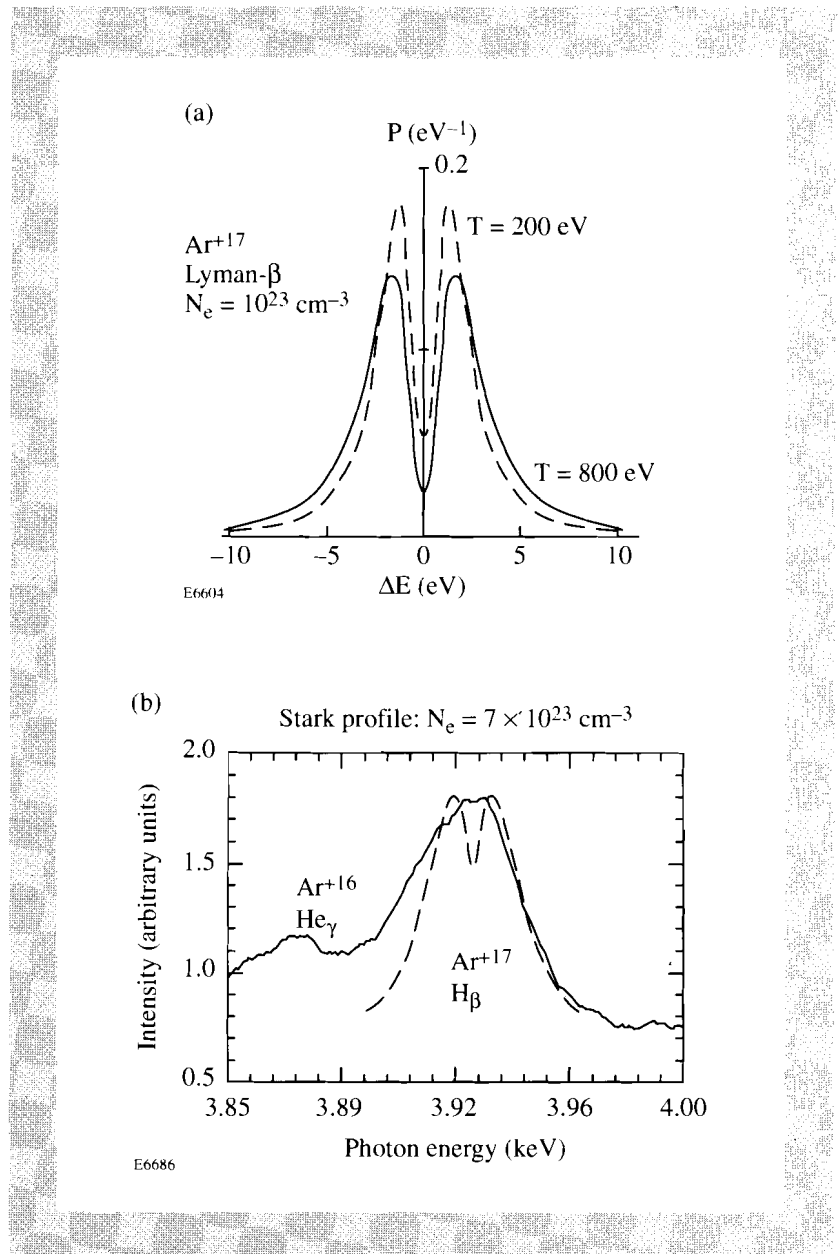


Fig. 55.9  
 (a) Calculated Stark profiles (from Ref. 1) for the same electron density but two different temperatures. For an unknown temperature in the range of 200 to 800 eV, the deduced density can be in error of less than  $\pm 20\%$ . (b) Fitting of a theoretical Stark profile to the measured Lyman- $\beta$  line of  $\text{Ar}^{+17}$  (at 3151 eV) for shot 24501.

An additional signature associated with the free-bound continuum is the reduction of ionization energy. As is evident from Fig. 55.8, the free-bound continua extend well into the low-energy side of the  $K$  edge before falling. This reduction is due to the interaction with neighboring ions (or the background plasma) and depends on the density and temperature. Because of the overlap of the  $\text{Ar}^{+17}$  edge with the  $e^- + \text{Ar}^{+17}$  continuum, it is easier to determine the measured shift of the  $\text{Ar}^{+16}$  edge. Generally, the effect increases with increasing density and decreasing temperature. Using the theory developed by Stewart and Pyatt,<sup>3</sup> we show in Fig. 55.10 the calculated reduction in ionization energy of helium-like argon ( $\text{Ar}^{+16}$ ) for the relevant parameter ranges. The calculation is for the same argon-to-deuterium ratio as in shot 24501 (1:200 in fill pressures). A similar calculation was done for hydrogen-like argon ( $\text{Ar}^{+17}$ ). As seen, the reduction depends on both temperature and density for the parameter ranges encountered here. There are two limiting expressions (defined by the number  $N_D$  of particles in the Debye sphere) that are sometimes used for the reduction in the ionization energy  $\Delta E_i$ :

$$\Delta E_i = e^2 / r_D \quad (\text{for } N_D \gg 1)$$

and

$$\Delta E_i = e^2 / a \quad (\text{for } N_D \ll 1), \quad (1)$$

where  $r_D$  is the Debye length and  $a$  is the ion-sphere radius; the first is given by the Debye-Huckel theory and the second by the ion-sphere model. As a rule, the Stewart-Pyatt model gives smaller energy shifts than either theory. In addition, the parameter ranges in Fig. 55.10 correspond to intermediate values of  $N_D$  ( $N_D \sim 1$ ). As a result,  $\Delta E_i$  in Fig. 55.10 does depend on the temperature, which is not the case for the ion-sphere model; however, the dependence on density is closer to that of the ion-sphere model ( $\sim \rho^{1/3}$ ) than to that of the Debye-Huckel model ( $\sim \rho^{1/2}$ ).

Using Fig. 55.10, we estimate the reduction in ionization energy in the experiment (shot 24501). We use the density value derived from the Stark broadening of the Lyman- $\beta$  line [Fig. 55.9(b)], and the temperature derived from the continuum slope [Fig. 55.8(b)]. The derived reduction for  $\text{Ar}^{+16}$  is  $\Delta E_i = 120$  eV, and for  $\text{Ar}^{+17}$  the reduction is 130 eV. The vertical bars in Fig. 55.8(a) show the unshifted positions of the hydrogen-like and helium-like  $K$  edges (o subscript), as well as the shifted positions, calculated from the experimentally determined density and temperature. As seen, the predicted reduction is generally consistent with the shape of the measured continuum. The shift of the hydrogen-like edge is not clearly seen because of a smaller continuum jump at this edge.

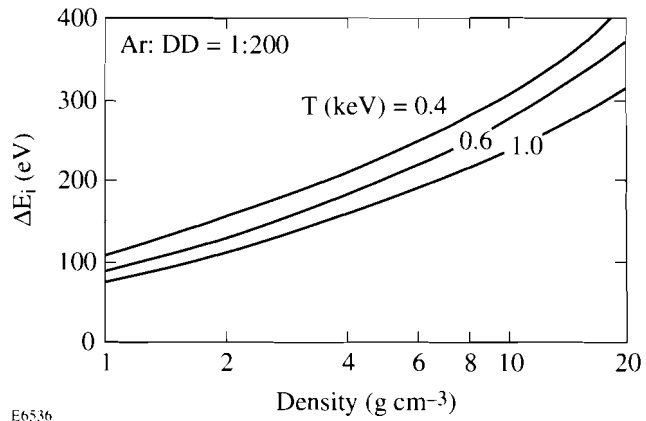


Fig. 55.10

Calculated reduction in ionization energy of Ar<sup>+16</sup> (helium-like argon) for the relevant parameter ranges, using the theory of Stewart and Pyatt (Ref. 3). The calculation is for the same argon-to-deuterium ratio as in shot 24501 (1:200 in fill pressures).

The electron temperature can be additionally estimated from the continuum jump. This is the intensity ratio ( $I^+/I^-$ ) between the continuum just to the high-energy side of the *K* edge and that to the low-energy side. The continuum on the low-energy side is due to recombination to higher levels (*L* shell, etc.) as well as due to bremsstrahlung. The continuum on the high-energy side of the edge is due to all these processes, in addition to recombination to the *K* shell. This jump decreases strongly with increasing temperature because recombination radiation at a given frequency varies like  $(kT)^{-3/2} \exp[(E_i - h\nu)/kT]$ , whereas bremsstrahlung varies like  $(kT)^{-1/2} \exp(-h\nu/kT)$ ; hence, the ratio of the first to the second varies like  $(kT)^{-1} \exp(E_i/kT)$ .

Since the dependence of both recombination and bremsstrahlung on electron density is the same ( $\sim N_e^2$ ), one would expect this dependence to cancel out and leave only a temperature dependence. This indeed is the case in a calculated curve of the continuum jump near the *K* edge of hydrogen-like ions.<sup>4</sup> In that curve, the density-independent continuum jump is monotonically decreasing with increasing temperature. However, we need to modify that curve in two ways. First, the density independence of the continuum jump due to a given species is only correct for a constant fraction of the relevant ion species. The *K*-edge jump of Ar<sup>+17</sup> will start to fall as the temperature decreases because recombination ( $e^- + \text{Ar}^{+18} \Rightarrow \text{Ar}^{+17}$ ) will reduce the number of available Ar<sup>+18</sup> ions. The effect of the varying fraction of Ar<sup>+18</sup> ions with temperature (which also depends on density) was not included in the calculation of Ref. 4. Thus, instead of one monotonically decreasing curve, the continuum jump as a function of temperature has a maximum at low temperatures, which is density dependent. Only at high enough temperatures do the curves for different densities approach each other. Second, we need to calculate the jump near the Ar<sup>+16</sup> (helium-like) edge since this jump is much more distinct than that near the

$\text{Ar}^{+17}$  edge and is easier to compare to the experiment. For this continuum jump, the curves at high temperature decrease faster with increasing temperature than in the hydrogen-like calculations because here ionization of the type  $\text{Ar}^{+17} \Rightarrow \text{Ar}^{+18} + e^-$  reduces the number of  $\text{Ar}^{+17}$  ions, just as recombination of the type  $(e^- + \text{Ar}^{+17} \Rightarrow \text{Ar}^{+16})$  reduces the jump at low temperatures.

We calculated the continuum emission for each ion species from Ref. 5, coupled with the ionic populations calculated with the collisional-radiative code *POPION*.<sup>6</sup> In Fig. 55.11 we show the calculated continuum jump for the *K* edge of  $\text{Ar}^{+16}$ , as a function of temperature, for two electron densities. As seen, the curves indeed have density-dependent maxima and only at sufficiently high temperatures become almost density independent. Using the same procedure, we calculated the jump near the  $\text{Ar}^{+17}$  edge. For the density and temperature values deduced here, that jump is only about 1.1. This jump is dominated by the ratio of  $\text{Ar}^{+18}$  to  $\text{Ar}^{+17}$  ion populations, which is much smaller than 1 for these conditions—the reason why this edge is indistinct in Fig. 55.8.

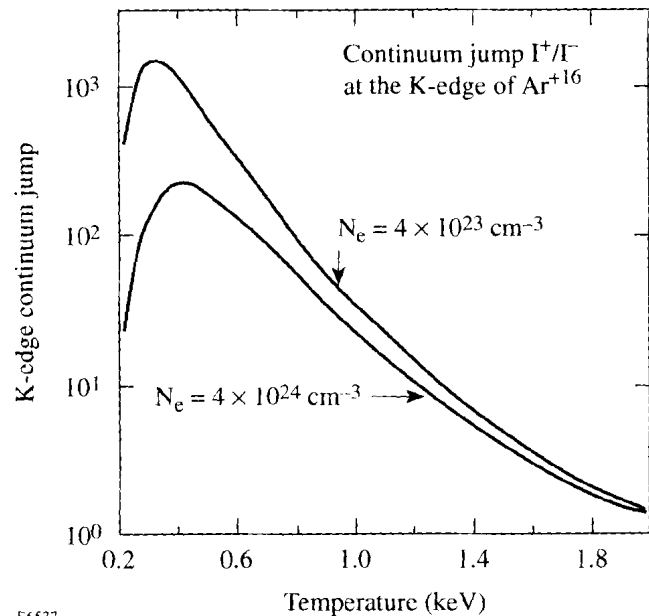


Fig. 55.11  
The calculated continuum jump for the *K* edge of  $\text{Ar}^{+16}$ , as a function of temperature, for two electron densities.

In Fig. 55.8, only a lower bound on the continuum jump can be estimated because the continuum level on the low-energy side of the edge ( $I^-$ ) is below the background level. To measure accurately the continuum jump as calculated here, we should have observed a continuum rising from the edge toward lower energies and having the same slope as the continuum above the edge (i.e., corresponding to  $T \sim 1$  keV). Such a rising continuum is only seen below  $\sim 3$  keV, and even then it is of a lower temperature. This means that the continuum of  $\sim 1$  keV below the edge is buried underneath the observed background, due to time integration, as well as radiation from, and attenuation by, cooler target regions. To obtain a lower bound on the continuum jump, we draw a line on the

semilog intensity plot [Fig. 55.9(b)] having a slope of 1 keV and going through the lowest observed continuum intensity. This yields a minimum jump of 14, which from Fig. 55.11 corresponds to  $T < 1.2$  keV. Note that we have arbitrarily placed the line marking the continuum jump near 4 keV. Because of the high sensitivity of the jump to temperature, only an approximate slope must be known to yield a reasonable temperature estimate.

As an additional diagnostic tool, we use the *RATION* code<sup>7</sup> to calculate the total line and continuum spectrum emitted by an argon plasma of a given temperature and density. *RATION* is a steady-state, non-LTE atomic physics code, which includes the transport of lines through the target using the escape-factor approximation, as well as Stark and Doppler broadening. We vary the temperature and density to achieve best correspondence with the experimental profile. The main value in applying this procedure is to test additional consistencies not checked in the foregoing analysis, such as intensity ratios between lines or lines and continuum, etc. A complete correspondence between calculated and time-integrated spectra is not expected unless most of the spectrum is emitted over time and space where the conditions do not change significantly. This can be expected to approximately be the case for emission from peak compression. Figure 55.12 shows the *RATION* spectrum corresponding to  $T = 1$  keV and  $N_e = 0.7 \times 10^{24} \text{ cm}^{-3}$  ( $\rho = 2.3 \text{ g cm}^{-3}$ ). The effect of opacity was included, assuming a 40- $\mu\text{m}$ -diam core. Also, an instrumental linewidth of 15 eV was included in the calculation. The predicted spectrum agrees with the measured spectrum in general, but not in all details. For example, the line-intensity ratios are somewhat different and indicate that the temperature in the experiment as measured by the line ratios is lower than 1 keV. The difference in  $T_e$  as determined by the lines and by the continuum is the result of integrating in time and space over emission from somewhat different temperatures.

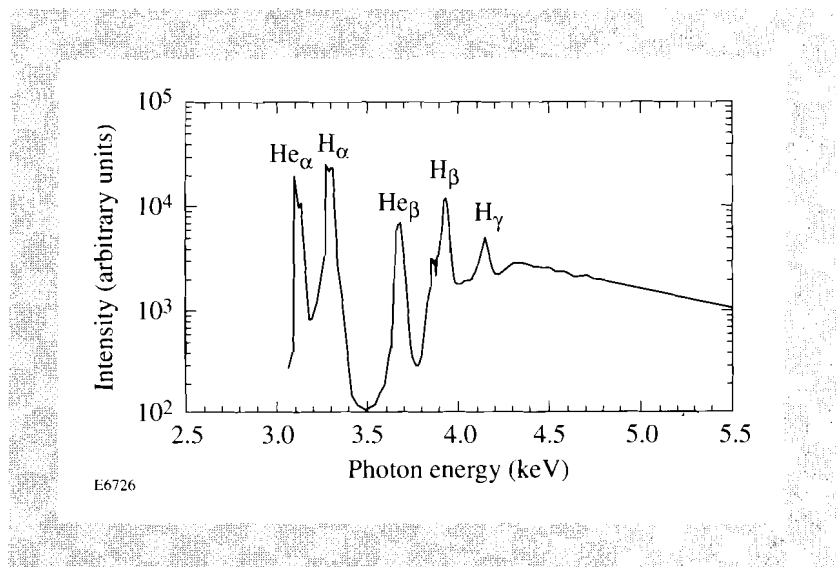


Fig. 55.12

The spectrum calculated by the code *RATION* with the following assumed parameters:  $T = 1$  keV and  $N_e = 0.7 \times 10^{24} \text{ cm}^{-3}$  ( $\rho = 2.3 \text{ g cm}^{-3}$ ).

### High-Pressure Argon Experiments

In Fig. 55.13 we show a comparison between the spectra from a high-pressure (shot 24498) and a low-pressure (shot 24501) argon target. As mentioned above, the high or low pressure refers here to the partial pressure of argon. This difference in pressure affects the resonant (self) absorption of argon lines and yields very different emergent spectra.

One issue needing clarification before analysis can be applied is the emission from the argon gas trapped in the polymer shell during the filling process. This gas is heated by the laser and emits argon lines from the ablated region. As such, it is not relevant to the diagnosis of the compressed core. However, these lines provide convenient spectral references because their broadening in the low-density ablated plasma is very small. Figure 55.13 shows that these narrow lines appear only in the high-pressure shot; the low-pressure shot shows Stark-broadened lines coming from the compressed core. This can be understood by the severe opacity of the argon lines in the high-pressure case. The lines from the core are absorbed on the way out within a cooler argon layer, and the narrow lines from the shell can be observed with no competition from the core lines. In the low-pressure case, the unabsorbed core lines dominate over the lines from the shell because the core argon gas has both higher total mass and higher density as compared to the argon gas in the shell. On the other hand, the intensity of the argon lines from the shell should be proportional to the fill pressure, which is consistent with Fig. 55.13.

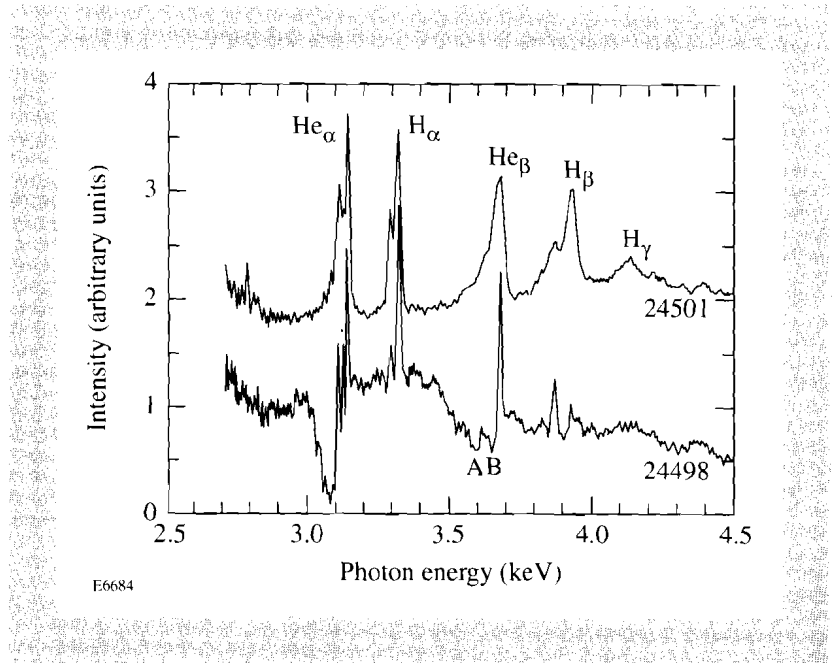


Fig. 55.13

Measured spectra at low and high argon-fill pressures. For shot 24501, the target was filled with 0.1 atm argon and 20 atm deuterium; for shot 24498 the target was filled with 20 atm argon. The scale on the left refers to shot 24498; the spectrum for shot 24501 is on the same intensity scale but was displaced upward for clarity. The A and B features are explained in the text.

The high-pressure spectrum shows no lines of helium-like ( $\text{Ar}^{+16}$ ) nor hydrogen-like ( $\text{Ar}^{+17}$ ) species from the core, as is the case for the low-pressure shots. The absence of these lines cannot be attributed solely to self-absorption (opacity) because under strong opacity conditions these lines should have appeared as absorption lines. This is indeed the case for lines of lower ionizations as seen in the high-pressure spectrum. There are two groups of such lines that appear in absorption. The first is on the low-energy side of the helium- $\alpha$  line ( $1s2p-1s^2$ ) at 3140 eV. The second appears on the low-energy side of the helium- $\beta$  line ( $1s3p-1s^2$ ) at 3683 eV. Whereas the first group has been studied extensively in the past,<sup>8-14</sup> the second group has been studied only recently<sup>15</sup> and has been observed only in emission.<sup>16</sup> The absorption lines in the first group are due to transitions of the type  $1s^2-1s2p$  in argon ions with partially filled  $L$  shells; likewise, the absorption lines in the second group are due to transitions of the type  $1s^2-1s3p, 1s3d$  in argon ions with partially filled  $L$  shells. These lines are thus absorbed in a cooler argon peripheral layer, where lower ionizations prevail. The area enclosed within these absorption lines is proportional to the  $\rho\Delta R$  of that cooler region.<sup>8</sup> However, in typical cases the first group of absorption features (near the helium- $\alpha$  line) has yielded only a lower limit on that quantity. The reason is that a relatively small value of  $\rho\Delta R$  is sufficient to absorb these lines almost completely. In Ref. 8, the flat-bottom absorption structure near the helium- $\alpha$  line yielded a lower bound of only  $\sim 5 \text{ mg/cm}^2$  for the  $\rho\Delta R$  of the cool, absorbing layer.

The interest in the absorption features near the helium- $\beta$  line is that their absorption probabilities are lower than for the comparable absorption lines near the helium- $\alpha$  line. As a result, the absorption near the helium- $\beta$  line in Fig. 55.13 is much weaker than that near the helium- $\alpha$  line. The former can thus yield a better estimate of the  $\rho\Delta R$  of the absorbing layer. Using the methods described in Ref. 8, we estimate for the  $\rho\Delta R$  of the absorbing layer of Fig. 55.13, using the absorption features near the helium- $\alpha$  line:  $\rho\Delta R > 5 \text{ mg/cm}^2$ . Applying the same procedure to the absorption features near the helium- $\beta$  line we obtain  $\rho\Delta R \sim 8 \text{ mg/cm}^2$ . In deriving this value we made use of the absorption oscillator strength in  $1s-3p$  transitions in hydrogen-like ions, which is 5.4 times lower than for  $1s-2p$  transitions. As in Ref. 8, the  $\rho\Delta R$  of the absorption layer consists of the sum of absorption due to successive charge states, which is proportional to the total area within the absorption structure.

The spectral features near the helium- $\beta$  line have been recently measured in emission (rather than in absorption) and extensively studied. A comparison of the spectra in the two cases shows a close similarity. In particular, the two features marked A and B in Fig. 55.13 correspond to the two features calculated in Ref. 15 as due to transitions of the type A:  $1s2l3l'-1s^22l$ , and type B:  $1s3l3l'-1s^23l$ . We note that in type A the "spectator" electron is in the  $n=2$  shell, whereas in type B it is in the  $n=3$  shell. When the lines appear in absorption, the absorbing (or initial) state in type A is the ground state of the relevant ion, whereas in type B it is an excited state. The fact that the A and B features in Fig. 55.13 have comparable areas indicates strong excitation of the absorbing ions. The excitation energy of the various ions contributing to the absorption varies from 200 eV for the lithium-like ion to 250 eV for the nitrogen-like ion.

Using these values in a collisional-radiative model, we estimate the temperature in the absorption region to vary in the range 80 to 160 eV. Other inner layers of argon fill gas can have a higher temperature; however, for much higher temperatures the population would have been dominated by helium-like ions. We know this is not the case since no helium-like absorption lines appear in the high-pressure spectrum of Fig. 55.13. Using this, we can obtain an upper limit on the temperature in the absorption layer:  $T < 600$  eV.

It is instructive to compare the high-pressure spectrum of Fig. 55.13 to code prediction. Figure 55.14 shows the spectrum calculated by the *LILAC* code coupled to an atomic physics post-processor. Here, strong absorption in helium-like lines is evident, contrary to the observed spectrum. It should be noted that the absorption features near the helium- $\beta$  line are not included in the code calculations, as are the absorption features near the helium- $\alpha$  line. In particular, the predicted strong absorption of the He $\beta$  line (at 3683 eV) is missing in the observed spectrum. The narrower He $\alpha$  line (at 3140 eV) overlaps the nearby lower-ionization absorption features, so it is not very clear whether the line is missing from the high-pressure spectrum. However, the much broader He $\beta$  line (especially its higher-frequency wing) is free from such overlap, and its absence from the measured spectrum is thus more definite. If the core temperature is nowhere higher than about 600 eV, no strong Ar $^{+16}$  lines would be emitted; however, these very lines could still appear in absorption due to continuum absorption on Ar $^{+16}$  transitions. The absence of such absorption lines can be explained by a combination of two factors: (a) cooler-than-predicted temperature and (b) lower-than-predicted  $\rho\Delta R$  for the absorption region and, by implication, for the whole core. The lower-than-predicted values could be the result of hydrodynamic instability, which degrades the compression and, thus, its resulting core heating.

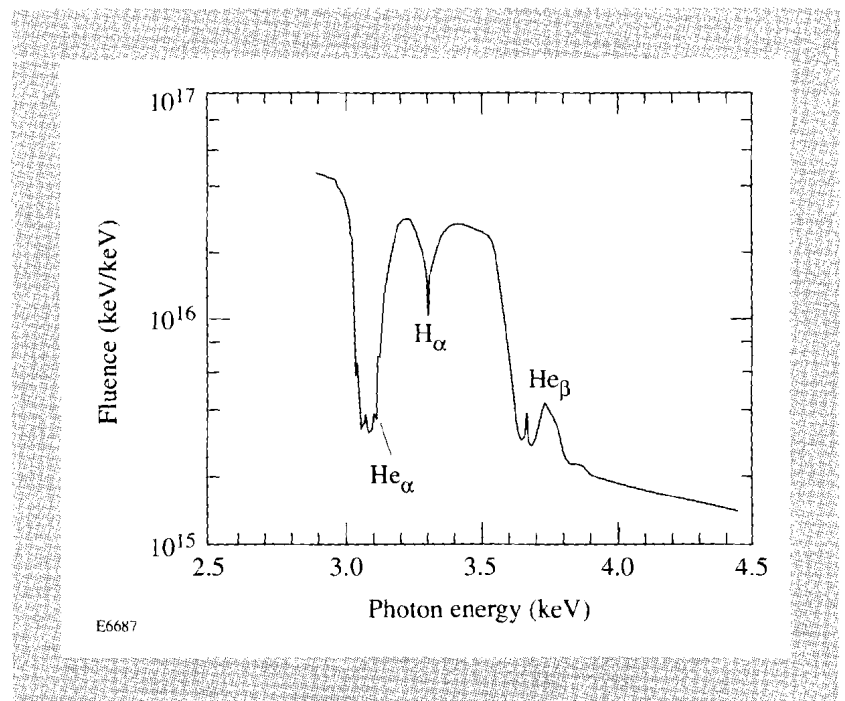


Fig. 55.14  
Time-integrated, code-predicted spectrum for shot 24498 (compare to Fig. 55.13).

## ACKNOWLEDGMENT

This work was supported by the U.S. Department of Energy Office of Inertial Confinement Fusion under Cooperative Agreement No. DE-FC03-92SF19460, the University of Rochester, and the New York State Energy Research and Development Authority. The support of DOE does not constitute an endorsement by DOE of the views expressed in this article.

## REFERENCES

1. C. F. Hooper (private communication).
2. H. R. Griem, *Spectral Line Broadening by Plasmas* (Academic Press, New York, 1974), Eq. (16), p. 8.
3. J. C. Stewart and K. D. Pyatt, Jr., *Astrophys. J.* **144**, 1203 (1966).
4. H. R. Griem, *Plasma Spectroscopy* (McGraw-Hill, New York, 1964), Chap. 13.
5. *ibid*, Chap. 5.
6. R. Epstein, S. Skupsky, and J. Delettrez, *J. Quant. Spectros. Radiat. Transfer* **35**, 131 (1986).
7. R. W. Lee (private communication).
8. LLE Review **49**, 1 (1991).
9. J. Delettrez, R. Epstein, D. K. Bradley, P. A. Jaanimagi, R. C. Mancini, and C. F. Hooper, Jr., in the *Proceedings of the International Workshop on Radiation Properties of Hot Dense Matter*, Sarasota, FL, 22–26 October 1990, p. 309.
10. L. A. Woltz, V. L. Jacobs, C. F. Hooper, Jr., and R. C. Mancini, *Phys. Rev. A* **44**, 1281 (1991).
11. R. Epstein, *Phys. Rev. A* **43**, 961 (1991).
12. R. C. Mancini, C. F. Hooper, Jr., J. A. Delettrez, R. Epstein, D. K. Bradley, P. A. Jaanimagi, and M. C. Richardson, in the *Proceedings of the International Workshop on Radiation Properties of Hot Dense Matter*, Sarasota, FL, 22–26 October 1990, p. 82.
13. R. C. Mancini and C. F. Hooper, Jr., *Rev. Sci. Instrum.* **61**, 27 (1990).
14. R. C. Mancini, C. F. Hooper, Jr., and R. L. Coldwell, to be published in *Journal of Quantitative Spectroscopy & Radiative Transfer*.
15. R. C. Mancini *et al.*, *Rev. Sci. Instrum.* **63**, 5119 (1992).
16. B. A. Hammel *et al.*, *Rev. Sci. Instrum.* **63**, 5017 (1992).

## **Section 2**

# **ADVANCED TECHNOLOGY DEVELOPMENTS**

### **2.A Phase Conversion of Lasers with Low-Loss Distributed Phase Plates**

An essential requirement for direct-drive laser fusion is the uniform irradiation of spherical targets that are located at the far field and quasi-far field of a laser system. Uniform absorption of laser light results in reduced Rayleigh-Taylor instabilities and improved spherical convergence of the target during high-density compression. A major impediment to achieving irradiation uniformity with high-power, solid-state laser systems is the presence of hot-spot structure in each of the frequency-converted beams at the target plane. The hot-spot intensity nonuniformities are caused by spatial variations in the near-field phase front of each laser beam. The central thrust of beam-uniformity studies involves controlling the beam profile presented to the target plane. Laser phase conversion provides a means to modify a laser beam's coherence properties, thereby changing its focusing characteristics.

Distributed-phase-plate (DPP) technology, previously deployed as two-level phase plates on the OMEGA laser system,<sup>1</sup> has been recently developed to efficiently increase the level of irradiation uniformity on target for the OMEGA Upgrade laser system. Phase conversion using two-level DPP's had provided a center-peaked energy distribution with high-order diffraction losses. However, specific profiles, such as super-Gaussian, inverse-quadratic, or cosinusoidal, do not possess undesirable diffraction losses. Target irradiation using these desired profiles increases the energy available to the target and reduces the threat of damage to target diagnostics. However, it is simultaneously required that an insensitivity to near-field wavefront errors be maintained.

Hence, the primary goal in the design of laser phase converters is to achieve lossless, wavefront-insensitive, phase conversion that allows flexible control of the laser-beam profile.

Another important goal for irradiation-uniformity research involves controlling the power spectrum and reducing the contrast of the initial speckle modulation produced by the process of phase conversion. The focusing of a spatially (phase) coherent laser beam produces a strongly modulated focal spot that contains medium- to low-frequency hot spots. On the other hand, the focusing of a phase-converted laser beam, using DPP's, produces a circularly shaped beam with a speckle distribution that contains higher frequency modulation with correspondingly higher peak irradiance. A laser-beam power spectrum, positioned somewhere between these two extremes, may provide a time instantaneous irradiation uniformity that less efficiently seeds the Rayleigh-Taylor instability. Since the validity of this assumption remains an important question, experimental investigation of this possibility, using flexible DPP technology, is warranted.

Over the past five years, lens arrays, Fourier gratings, and other diffractive optics have been developed as improvements to the two-level DPP used on the OMEGA system. Recent theoretical calculations and experimental demonstrations have shown that a large fraction of the energy, lost at the target by the two-level DPP, can now be regained by producing multibeamlet overlap with continuous DPP's that contain either an array of lenses or a two-dimensional grating-like structure. Extensive design and analysis of a new baseline DPP have been completed for the OMEGA Upgrade laser.

### **Phase-Plate Modeling**

The randomly assigned, binary-phase-encoded, ordered array (Fig. 55.15) has been used for the phase conversion of laser light together with various beam-smoothing schemes.<sup>1,2</sup> However, phase conversion with two-level DPP's is not optimized for efficient energy coupling or diffraction pattern flexibility. Previous DPP's were composed of an ordered array of transparent elements. For this variety of phase plate, the phase values of approximately 15,000 hexagons are randomly binned into two levels that differ in phase by  $\pi$  radians. The diffraction patterns of the hexagonal beamlets are collected and brought to focus for target irradiation. The diffracted laser light, due to each hexagonal element, observed at the focal plane of a lens resembles an Airy-disc pattern. The coherent addition of all the diffracted beamlets is also approximated by an Airy-disc pattern. The circled-energy curve shows that only a 75% energy efficiency is obtained when the 8% intensity contour is tangentially mapped to the target.

Alternatives to the two-level binary phase plate include the lenslet array, the random phase array, the Fourier grating, as well as numerous combinations of these basic forms. Each of these phase plates can be composed of either multilevel binary structures such as the optical kinoform<sup>3</sup> or a continuous-surface relief. In contrast to the two-level binary phase plate, the lenslet array<sup>4-6</sup> operates on a different principle. The lenslet array separates an incident laser beam into an array of beamlets made to overlap at the target plane by a focusing optic. The individual beamlets are directly mapped to the individual

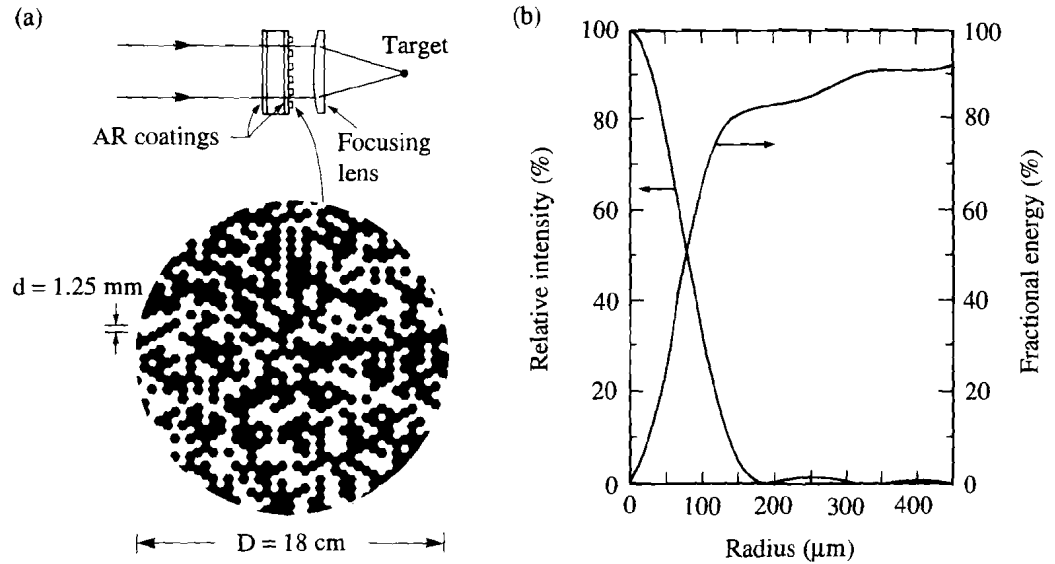


Fig. 55.15

(a) The randomly assigned, binary-phase-encoded, ordered array, referred to as a two-level distributed phase plate (DPP), was previously used for the phase conversion of the OMEGA laser to achieve smooth intensity distributions at the focal plane of a lens. Phase conversion with two-level DPP's is not optimized for energy efficiency or pattern flexibility as shown in the azimuthally averaged intensity profile (b).

elements of a Fourier plane array. Phase conversion with a lenslet array can provide high efficiency but suffers from envelope distortion and limited power spectrum flexibility. As another option for spatial phase conversion, the continuous random phase plate, characterized by a spatial correlation length and rms phase difference, uniformly increases the angular spectrum of an incident beam to form a single focal spot at the target plane. Phase conversion with a continuous random phase plate can provide high efficiency but only limited pattern flexibility.

Several new phase-plate designs are based on the simple Fourier grating.<sup>7-13</sup> Phase conversion with a Fourier grating can provide both high efficiency and pattern flexibility. The purpose of the Fourier grating is to diffract the collimated incident beam into multiple orders or multiple beamlets (Fig. 55.16). These orders are collected by a lens to form an array of foci at the Fourier plane of the lens. The lateral separation between the foci ( $d^*$ ) can be expressed in terms of the wavelength  $\lambda$  of light used, the  $f$ -number ( $f_{\#}$ ) of the focusing lens, and the number of grooves or elements in the grating,  $N$ :

$$d^* = \lambda f_{\#} N = \lambda f N / D, \quad (1)$$

where  $N$  is equal to the diameter of the grating ( $D$ ) divided by the groove spacing ( $d$ ):  $N = D/d$ . The Fourier grating separates an incident laser beam into a periodic angular spectrum of beams made to focus at the focal plane of a lens. In contrast

to the lenslet array, for the case of a Fourier grating, the entire laser beam is mapped to each of the individual elements of the foci array (Fig. 55.17). Placement of the target surface outside the focal plane of the lens causes an expansion and overlap of the foci. For a system with a 28-cm-diam beam, a 1.8-m focal length, and a 700- to 1000- $\mu\text{m}$  target diameter, the propagation distance beyond the focal plane ( $\Delta z$ ) is between 0 and 4 mm. The interference pattern associated with the overlap of the beamlets depends primarily on the phase-transfer-function of the distributed phase plate.

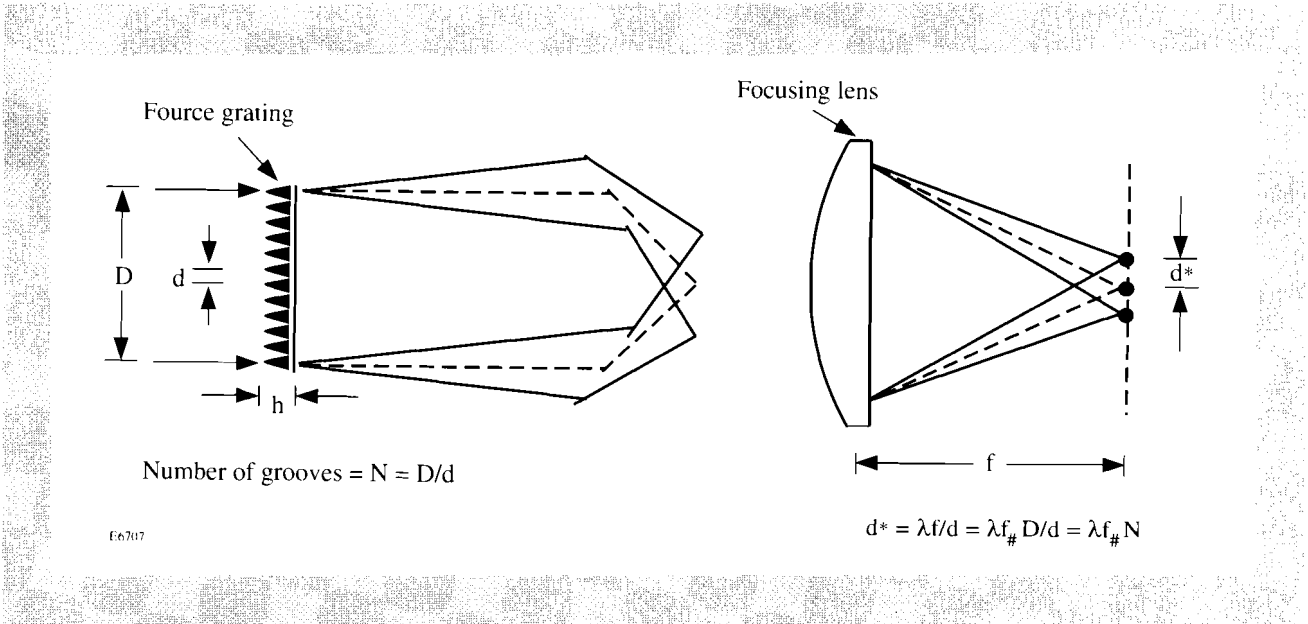


Fig. 55.16

A Fourier grating separates an incident laser beam into a periodic angular spectrum of beams brought together at the focal plane of a lens. The entire near field of the laser beam is simultaneously mapped to each of the elements of the foci array. Phase conversion with properly modified Fourier gratings can provide high efficiency and pattern flexibility.

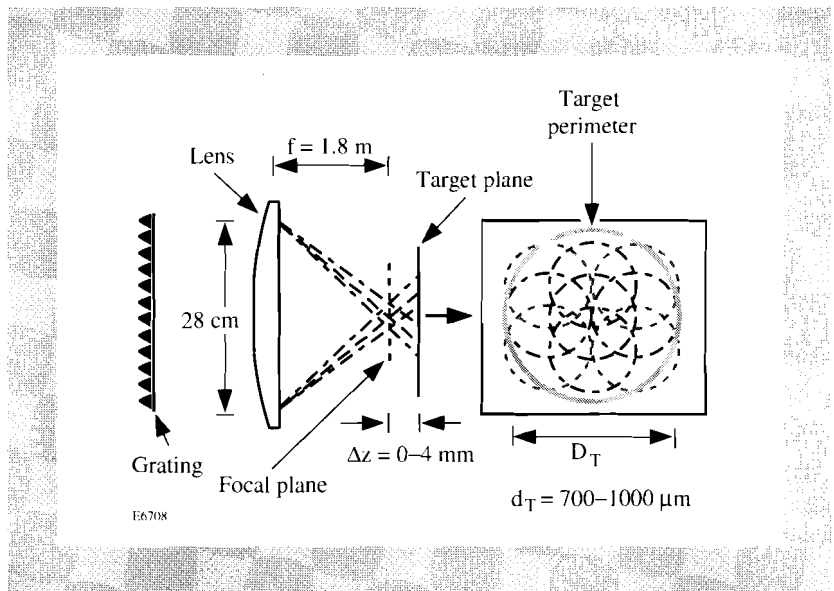


Fig. 55.17

The foci produced by a Fourier grating expand and overlap outside the focal plane of the lens. For a system with a 28-cm-diam beam, a 1.8-m focal length, and a 700- to 1000- $\mu\text{m}$  target diameter, the required propagation distance beyond the focal plane is approximately 4 mm.

The profile of a surface-relief Fourier grating, schematically represented in Fig. 55.18, can in the simplest case be composed of one sinusoidal component. This simple form does not generally meet the important requirements for phase conversion; however, it is useful in explaining the basic physics of continuous phase plates. Phase retardation is distributed over a two-dimensional surface by introducing optical path differences (OPD's) in the form of a thin film of varying thickness  $t(x,y)$  and material refractive index  $n$ . The exact amount of phase retardation  $\Phi$  experienced by a transmitted wavefront depends upon the wavelength ( $\lambda$ ) of light and is given by

$$\phi = \frac{2\pi}{\lambda}(\text{OPD}) = \frac{2\pi}{\lambda} [t(x,y)(n-1)] . \quad (2)$$

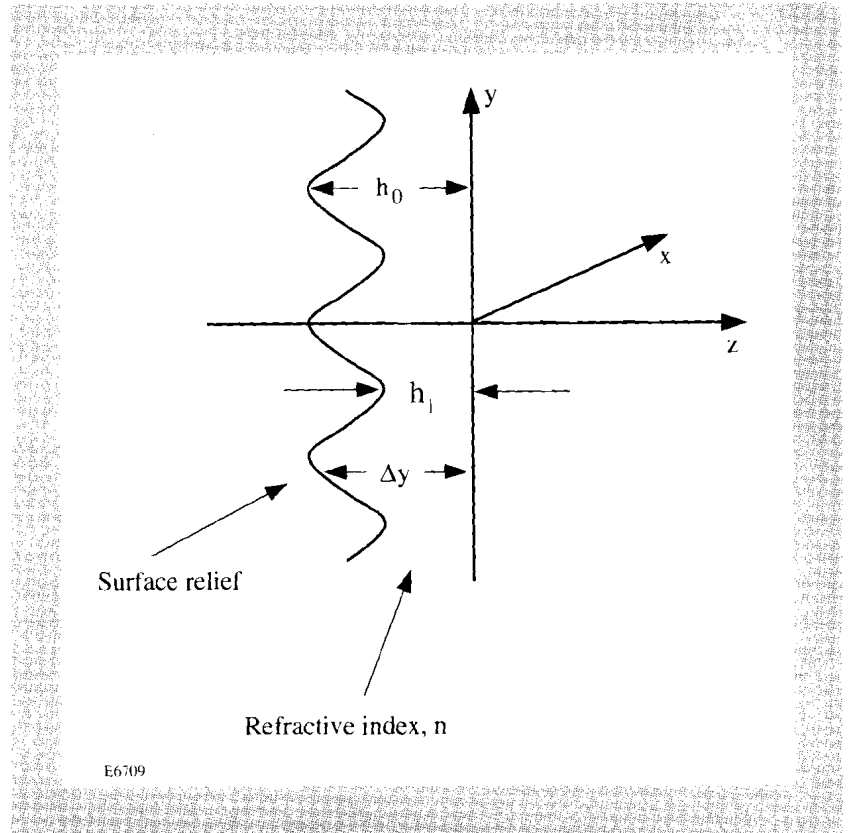


Fig. 55.18  
The optical path profile of a surface-relief diffractive structure is characterized by its spatially varying surface height (thickness  $t$ ) and its material index of refraction ( $n$ ). These phase plates typically have a height variation of several microns and a spatial scale of several millimeters.

The complex amplitude transmittance of the two-dimensional Fourier grating is defined as

$$t(\alpha, \beta) = e^{i2kh_0} e^{ik(n-1)} \left\{ \left[ (h_0 - h_1) \cos(2\pi\alpha/d) + (h_0 + h_1) \right] / 2 \right\} \\ \times e^{ik(n-1)} \left\{ \left[ (h_0 - h_1) \cos(2\pi\beta/d) + (h_0 + h_1) \right] / 2 \right\} . \quad (3)$$

The complex amplitude distribution of the laser beam, prior to being transmitted through the phase plate, is given by

$$a_L(\alpha, \beta) = \Psi_L(\alpha, \beta) e^{i\Phi_L(\alpha, \beta)} , \quad (4)$$

where  $L$  designates the laser beam.

The amplitude distribution of the laser light after transmission through the mask is a product of Eqs. (3) and (4):

$$\begin{aligned}
 a(\alpha, \beta) &= a_L(\alpha, \beta)t(\alpha, \beta) \\
 &= \Psi_L(\alpha, \beta)e^{i\Phi_L(\alpha, \beta)} \cdot e^{i2kh_0} e^{ik(n-1)\left\{\left[(h_0-h_1)\cos(2\pi\alpha/d)+(h_0+h_1)\right]/2\right\}} \\
 &\quad \times e^{ik(n-1)\left\{\left[(h_0-h_1)\cos(2\pi\beta/d)+(h_0+h_1)\right]/2\right\}} . \quad (5)
 \end{aligned}$$

Sinusoidal phase modulation within the exponent gives rise to a series of Bessel functions that, in the case of a solid-state laser beam, correspond to a series of aberrated point-spread functions that exist at the focus of a lens:

$$\begin{aligned}
 a(\alpha, \beta) &= \Psi_L(\alpha, \beta)e^{i\Phi_L(\alpha, \beta)} \cdot e^{i2kh_0} e^{i2k(n-1)(h_0+h_1)/2} \\
 &\quad \sum_l i^l J_l \left[ k(n-1)(h_0-h_1)/2 \right] e^{i2\pi\alpha/d} \text{rect}(\alpha/Nd) \\
 &\quad \sum_m i^m J_m \left[ k(n-1)(h_0-h_1)/2 \right] e^{im2\pi\beta/d} \text{rect}(\beta/Nd) . \quad (6)
 \end{aligned}$$

The resulting amplitude distribution located at the focal plane of a lens is given by the Fourier transform relation,

$$A(\epsilon, \eta) = \frac{e^{i2kf}}{i\lambda f} \iint a(\alpha, \beta) e^{-i2\pi(\alpha\epsilon + \beta\eta)} d\alpha d\beta , \quad (7)$$

where  $a(\alpha, \beta)$  is the complex amplitude distribution and  $\epsilon = \alpha/\lambda f$ ,  $\eta = \beta/\lambda f$  are the spatial-frequency variables. The input amplitude is a product of the laser-beam amplitude and the amplitude transmittance of the DPP.

Since the transform of a product is equal to the convolution of the individual transforms,  $A(\epsilon, \eta)$  can be conveniently expressed as

$$\begin{aligned}
 A(\epsilon, \eta) &= A_L(\epsilon, \eta) ** N^2 d^2 \left( e^{i2kf} / i\lambda f \right) e^{i2kh_0} e^{ik(n-1)(h_0+h_1)} \\
 &\quad \sum_l i^l J_l \left[ k(n-1)(h_0-h_1)/2 \right] \text{sinc} \left[ (l/d - \epsilon)Nd \right] \\
 &\quad \sum_m i^m J_m \left[ k(n-1)(h_0-h_1)/2 \right] \text{sinc} \left[ (m/d - \eta)Nd \right] , \quad (8)
 \end{aligned}$$

where  $A_L(\epsilon, \eta)$  is the Fourier transform of the laser-beam amplitude.

The above expression represents a two-dimensional convolution (denoted by \*\*) between the far-field amplitude distribution of the laser beam,  $A_L(\epsilon, \eta)$ , and the individual series components. This expression indicates the effect that the laser beam has on each individual Fourier component.

The focal irradiance distribution located at the Fourier plane of a lens is given by

$$I(\epsilon, \eta) = |A(\epsilon, \eta)|^2$$

$$\propto \left| A_L(\epsilon, \eta) ** \sum_l i^l J_l \left[ k(n-1)(h_o - h_l)/2 \right] \text{sinc}[(l/d - \epsilon)Nd] \right.$$

$$\left. \times \sum_m i^m J_m \left[ k(n-1)(h_o - h_l)/2 \right] \text{sinc}[(m/d - \eta)Nd] \right|^2. \quad (9)$$

The array of foci, representing the Bessel function series associated with sinusoidal phase modulation, is shown in Figs. 55.19(a) and 55.19(b). This irradiance distribution is itself not useful for laser-fusion experiments; however, accurate control of its power spectrum is important and can, in part, be achieved by specifying a particular set of Fourier components. Non-sinusoidal spatial phase modulation is required to achieve the desired intensity pattern flexibility on target. A DPP can be designed using one of many iterative phase retrieval algorithms.<sup>14-17</sup> However, optimum phase plates can also be designed using specific analytic functions that represent the beam's phase. This latter approach best utilizes Fourier-intuition and experimental ingenuity. Computationally intensive iterative algorithms can then be used to complete a specific DPP design after the basic concept is established.

A continuous DPP can consist of a specific combination of a Fourier grating plus a continuous random phase plate to achieve both high efficiency and pattern flexibility at the target plane (Fig. 55.20). Phase conversion with a continuous DPP can meet these design requirements over a sufficiently long depth of focus to accommodate a wide range of target diameters. Phase-plate designs consisting of a Fourier grating together with a continuous random phase distribution can produce desirable envelopes. The irradiance distribution from the combined phase plate, as described by a cross-section through the center [Fig. 55.21(a)] and a false, three-dimensional representation [Fig. 55.21(b)], looks qualitatively similar to that of the continuous random phase plate but it is less center-peaked. The random irradiance variations associated with speckle, which obeys negative exponential statistics, is the dominant visual characteristic for both of these phase plates. In both of these cases an energy transfer greater than 95% is delivered to the target plane. The combined phase plate produces a focal spot that encircles a 700- $\mu\text{m}$  target with an intensity contour of approximately 8% of the peak irradiance. Adjustments in the shape of the envelope at its center and edge

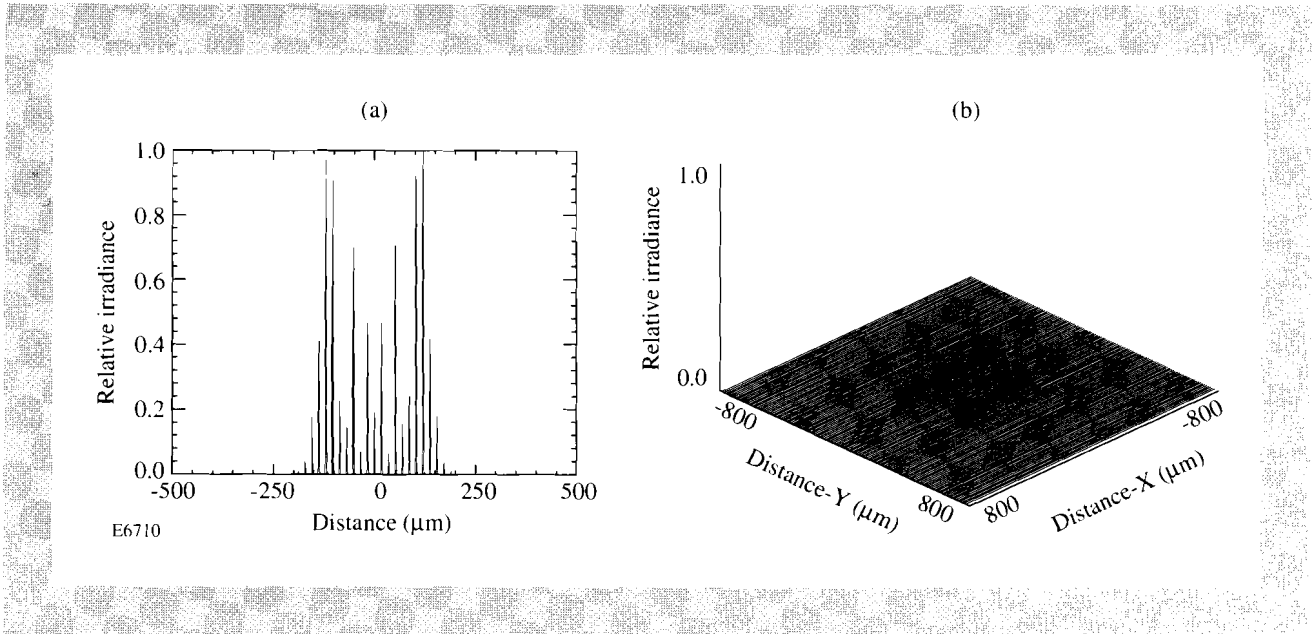


Fig. 55.19

The irradiance distribution at the focal plane of a lens contains an array of foci representing the Bessel function series associated with sinusoidal phase modulation. Figure 55.19(a) shows an intensity cross section while Fig. 55.19(b) shows the full two-dimensional distribution. This distribution is used for first-order DPP design but in itself is not useful for laser-fusion experiments. Nonsinusoidal spatial phase modulation is required to achieve the desired intensity pattern flexibility on target.

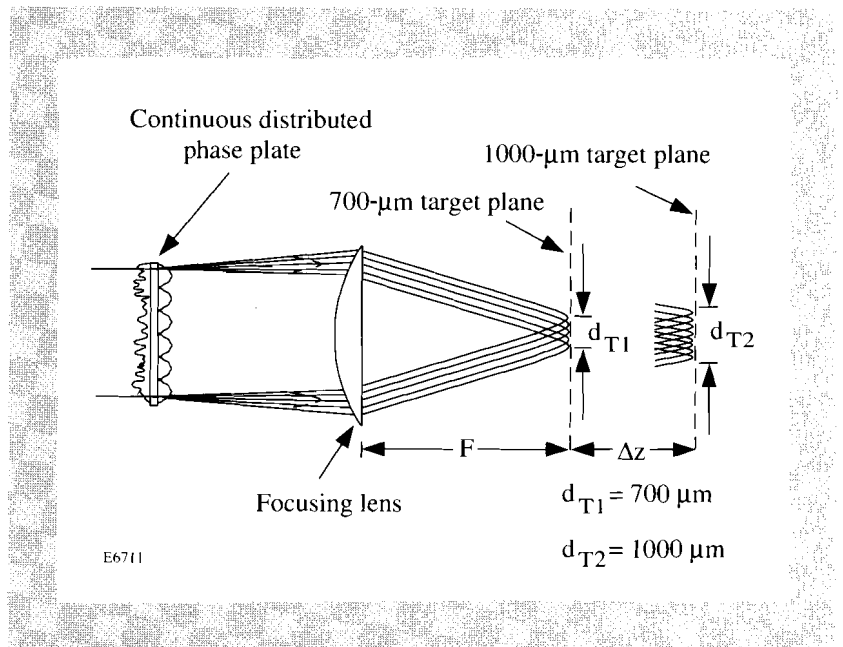


Fig. 55.20

A continuous DPP can consist of a combination of a Fourier grating and a continuous random phase plate to achieve both high efficiency and pattern flexibility at the target plane. Efficient phase conversion with a continuous DPP can be achieved over a sufficiently long depth of focus to accommodate a wide range of target diameters.

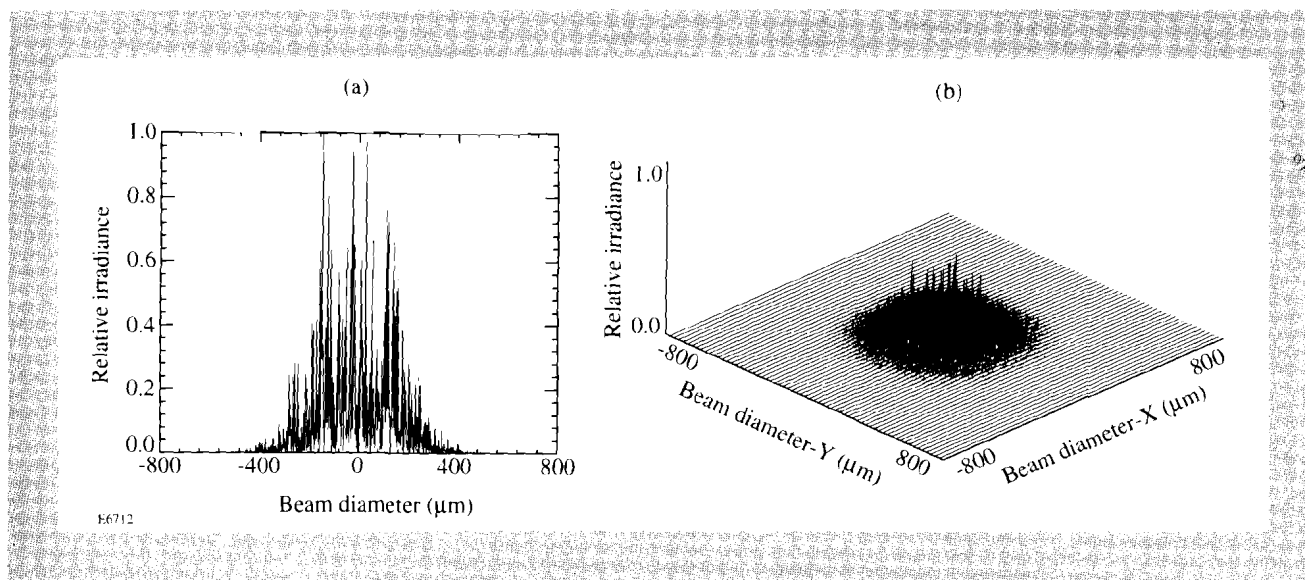


Fig. 55.21

The irradiance distribution from a continuous DPP, as described by a cross-sectional intensity scan through the beam center (a) and a false 3-D representation (b), looks qualitatively similar to that produced by a continuous random phase plate. The random irradiance variations, associated with speckle that obeys negative exponential statistics, is the dominant visual characteristic for both phase plates.

are made possible by varying the rms phase and correlation length of the random phase screen and also by varying the amplitude and frequency of the Fourier grating. Irradiation of larger targets can be accomplished with this same phase plate by placing the target outside the focal plane [Figs. 55.22(a) and 55.22(b)]. A typical axial shift from the focal plane, required to irradiate a 1000- $\mu\text{m}$  target, is approximately 4 mm. Figure 55.23 shows the azimuthally averaged, energy-normalized, intensity profiles at the focal plane (solid) and a 3-mm defocused plane (dotted). The dashed curve is an azimuthally averaged intensity profile of a Gaussian beam provided for reference. Additional modeling has shown that laser-beam phase errors, as severe as twice the OMEGA UV phase error, do not significantly alter the performance of these new continuous DPP's.

The advantage of placing the phase plate before the final focusing lens is that subsequent extraction or replacement is relatively simple. However, since diffraction occurs over the distances between the phase plate and the focusing lens and between the focusing lens and the vacuum window, high intensities can be created that potentially exceed the bulk damage threshold of the fused silica windows. For this reason, certain phase-plate designs, particularly the binary-phase variety, cannot be considered at locations prior to the focusing lens on the OMEGA Upgrade laser system. The results of diffraction calculations, shown in Figs. 55.24(a) and 55.24(b), indicate that very-low-intensity modulation is created by the continuous DPP considered for use in the OMEGA Upgrade laser. In contrast to this design achievement, the two-level binary phase plate, previously used on the OMEGA laser system, creates unacceptable high-intensity modulation. If used in future experiments, binary phase plates must be placed at the vacuum window to prevent laser damage.

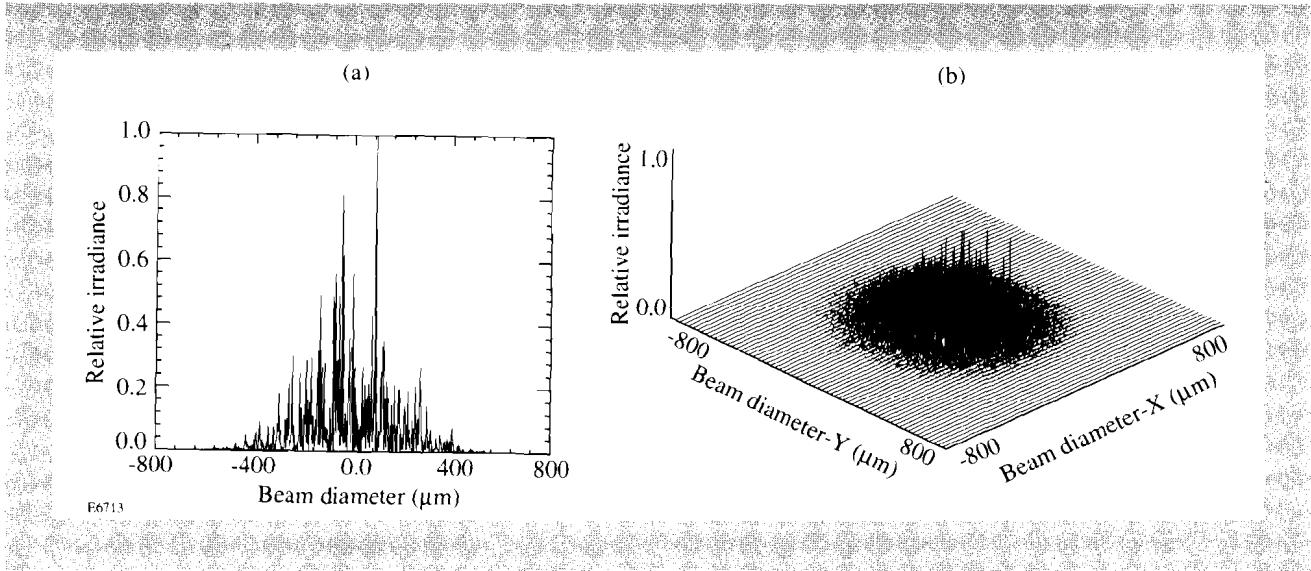
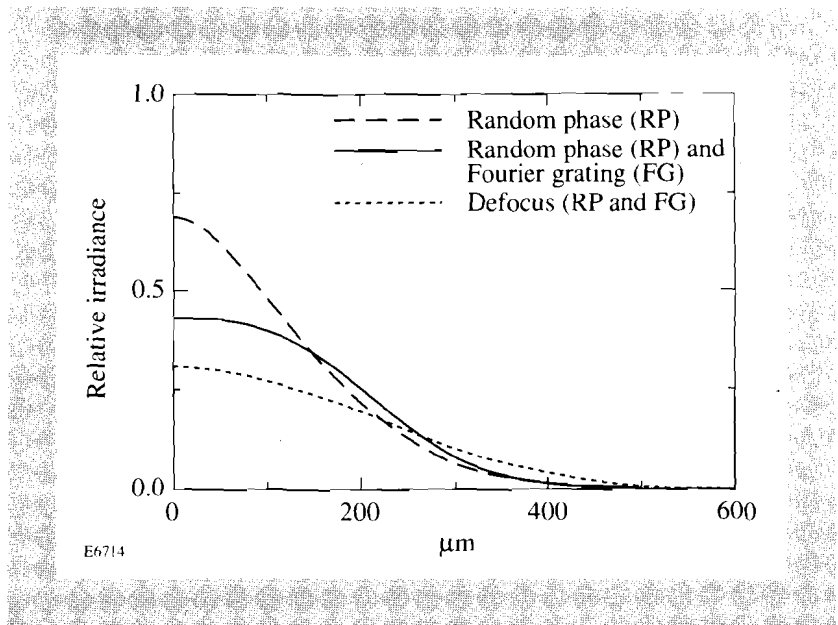


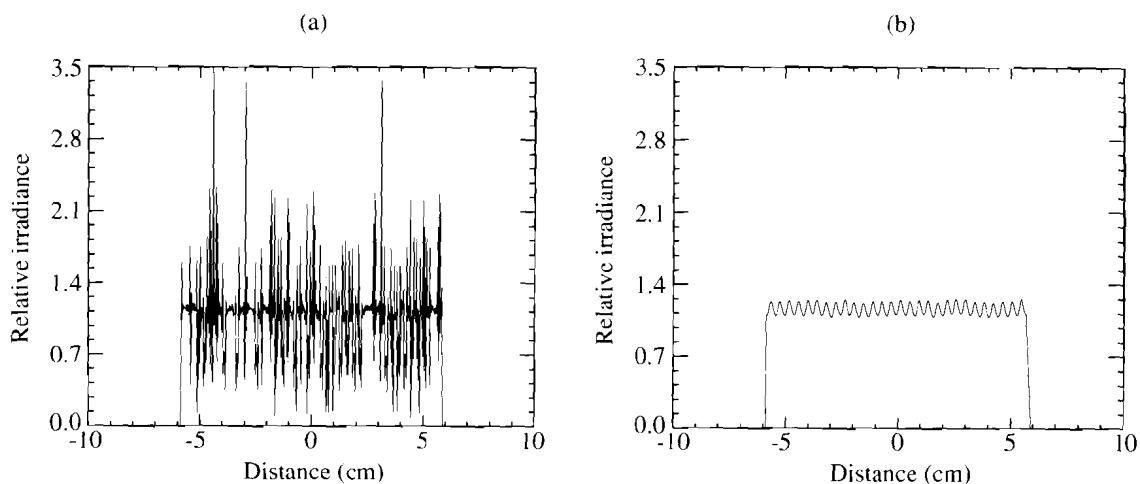
Fig. 55.22  
Larger targets can be uniformly irradiated with a similar intensity envelope and speckle distribution, using the same DPP, by defocusing several millimeters along the optical axis. A cross-sectional intensity scan (a) and a 2-D intensity plot (b) illustrate the similarity to the profile obtained at the focal plane of a lens.

Fig. 55.23  
The azimuthally averaged, energy-normalized profiles of the target-plane intensity distribution show that a DPP consisting of a Fourier grating and a continuous random phase plate (solid) is less center peaked than a Gaussian profile (dashed). Irradiation of larger targets using the same DPP is accomplished by placing the target outside the focal plane (dotted). In each case an energy transfer of 95% is delivered to the target plane.



**Experimental Activities**

Optical lithography has been chosen as the primary means of generating complex surface-relief structures in materials that are compatible with UV laser light. Both mask fabrication and photoresist patterning have been successfully demonstrated, using a combination of photographic and photolithographic techniques, by fabricating nearly full-scale, continuous DPP's. A major research effort at LLE currently involves the transfer and/or replication of a continuous DPP into one of the candidate UV materials. Characterization of the new DPP's involves assessment of the surface-relief transfer process and accurate measurement of the



E6715

Fig. 55.24

Diffraction occurs over the distances between the phase plate, focusing lens, and vacuum window, causing high intensities that potentially exceed the bulk damage threshold of fused silica windows. The two-level binary phase plate, previously used on the OMEGA laser system, creates unacceptable high-intensity modulation (a); however, very-low-intensity modulation is created by the new continuous DPP (b).

target-plane irradiance. Experimental investigation of the effects that the new DPP has on laser-beam alignment to the target is also critical to overall performance of the phase plate. It is anticipated that future studies of target performance and irradiation uniformity will provide the necessary requirements for optimum phase conversion of the OMEGA Upgrade laser system.

### Conclusions

A new variety of DPP, characterized as deep, surface-relief, continuous phase plates, has been invented for use within the OMEGA Upgrade laser system. These DPP's can perform nearly lossless phase conversion of high-power laser beams, thus delivering up to 25% more energy directly to the fusion capsule. Specific DPP designs can provide the desired intensity envelope and speckle distribution (power spectrum) over the full 700- to 1000- $\mu\text{m}$  range of target diameters envisioned for the future experimental target physics program at LLE. In addition, these new phase plates offer substantially less concern for optical damage due to diffraction-induced intensity ripples in the near field of the laser beams. An extensive experimental program is now underway to fabricate and characterize large-aperture, ultraviolet, continuous DPP's. These DPP's possess both unity efficiency and high damage threshold, meeting the design requirements for the OMEGA Upgrade laser system.

### ACKNOWLEDGMENT

This work was supported by the U.S. Department of Energy Office of Inertial Confinement Fusion under Cooperative Agreement No. DE-FC03-92SF19460, the University of Rochester, and the New York State Energy Research and Development Authority. The support of DOE does not constitute an endorsement by DOE of the views expressed in this article.

## REFERENCES

1. LLE Review **33**, 1 (1988).
2. Y. Kato *et al.*, Phys. Rev. Lett. **53**, 1057 (1984).
3. L. B. Lesem, P. M. Hirsch, and J. A. Jordan, Jr., IBM J. Res. Develop. **13**, 150 (1969).
4. X. Deng *et al.*, Appl. Opt. **25**, 377 (1986).
5. P. Langois and R. Beaulieu, Appl. Opt. **29**, 3434 (1990).
6. T. Jitsuno *et al.*, presented at CLEO '92, paper CThI2.
7. H. Dammann and K. Görtler, Opt. Commun. **3**, 312 (1971).
8. J. Jahns *et al.*, Opt. Eng. **28**, 1267 (1989).
9. U. Krackhardt, J. N. Mait, and N. Streibl, Appl. Opt. **31**, 27 (1992).
10. N. Streibl, J. Mod. Opt. **36**, 1559 (1989).
11. D. Daly, S. M. Hodson, and M. C. Hutley, Opt. Commun. **82**, 183 (1991).
12. P. Ehbets *et al.*, Opt. Lett. **17**, 908 (1992).
13. D. Prongué *et al.*, Appl. Opt. **31**, 5706 (1992).
14. R. W. Gerchberg and W. O. Saxton, OPTIK **35**, 237 (1972).
15. J. R. Fienup, Appl. Opt. **21**, 2758 (1982).
16. K. Ichikawa, A. W. Lohmann, and M. Takeda, Appl. Opt. **27**, 3433 (1988).
17. P. E. Keller and A. F. Gmitro, submitted to Applied Optics.

## 2.B Nematic Polymer Liquid-Crystal Wave Plate for High-Power Lasers at 1054 nm

Liquid-crystalline materials capable of replacing traditional crystalline solids in the production of wave plates are becoming more desirable due to the high cost of the solid crystals typically used,<sup>1</sup> including natural and synthetic mica, quartz, sapphire, magnesium fluoride, and KDP (potassium dihydrogen phosphate). The laborious and often expensive process of high-precision optical polishing of plates fabricated from these crystals makes their use still less feasible for large-aperture requirements. In addition, the range of available retardance values is limited, and the laser-damage thresholds are not always known.

Low-molecular-weight liquid-crystal monomers (LMLC's) have overcome the cost disadvantages of typical solid crystals. LMLC's are particularly successful in meeting specific retardance needs and can exhibit high resistance to pulsed-laser damage in IR and UV regimes.<sup>2</sup> Despite their many successes, LMLC's introduce some difficulties of their own—the use of thick glass substrates to support the LC without bowing and the epoxy sealing of these substrates without long-term transmitted-wavefront distortion due to the sealant.<sup>3</sup>

Polymer liquid crystals (PLC's) potentially meet the same needs as monomeric LMLC's but without their difficulties. PLC's generally have a high isotropic transition temperature. At and above this temperature, PLC's can be manipulated like LMLC's. At lower temperatures, the polymers become viscous enough to maintain their chosen configuration. The polymer also acts as its own substrate sealant, eliminating the need for epoxies.<sup>4</sup>

Here, we examine the properties of a nematic PLC (NPLC) aligned using a buffed nylon<sup>5</sup> 6/6 layer. Properties studied include viscosity (temperature dependence), birefringence (dispersion and temperature dependence), and laser-damage resistance. We describe three techniques to construct NPLC wave plates and evaluate the uniformity and transmitted wavefront quality of several 50-mm-diam devices.

### Properties of Nematic Polymer Liquid Crystal

#### 1. Structure and Physical Properties

The liquid-crystal polymer used for this study, LC360N, is a side-chain polymer with polysiloxane backbone<sup>6</sup> (see Fig. 55.25). The polymer's glass transition temperature and clearing temperature are 23°C and 88°C, respectively. Its viscosity at room temperature (22°C) is greater than  $3 \times 10^8$  cp ( $3 \times 10^5$  Pa-s), making it sticky to the touch. Since its dielectric anisotropy is nearly zero, it does not afford alignment by application of an electric field.

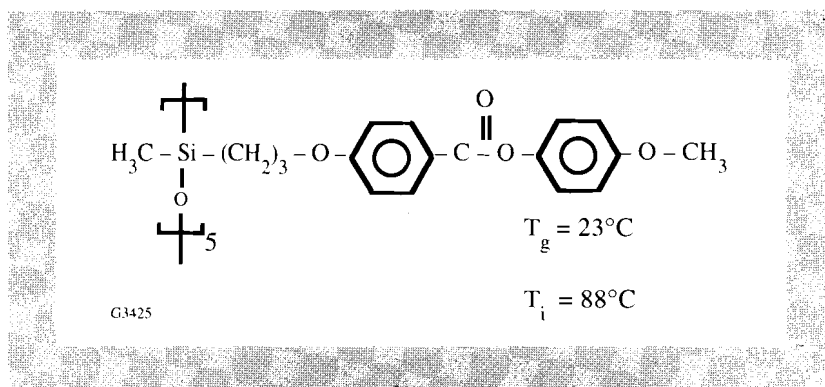


Fig. 55.25

Structure of the NPLC LC360N. The polysiloxane backbone is shown on the left.

#### 2. Viscosity

For a PLC to be useful in optical devices like wave plates, it must have a high viscosity at the temperature at which the device is to be used to ensure device stability. The PLC must also have a low enough viscosity at some convenient temperature to facilitate both alignment and device construction. LC360N meets both of these requirements as determined by a viscosity/temperature measurement.

Viscosity was measured using a commercial digital viscometer equipped with a helipath accessory.<sup>7</sup> The viscometer rotated a spindle and measured the force required to maintain a chosen rotational speed against the viscous drag of the sample; this force was directly related to the viscosity. The sample container had an inner diameter of 1.8 cm and the sample volume was 12 ml. For LC360N, at low temperatures ( $T < 80^\circ\text{C}$ ), a T-bar-type spindle (1.09-cm crossbar length) was used with helical path action. A stand raised and lowered the sample at a rate of 2.22 cm/min through a distance of 2.3 cm around the rotating spindle to ensure

that the spindle continuously encountered fresh polymer, i.e., not previously grooved. At high temperatures ( $T > 80^{\circ}\text{C}$ ), the usual disc-type spindle (1.46-cm diam) without the helipath accessory was used. As a result, there was a wider range of measured values for the higher viscosities (lower temperatures) due to the action of raising and lowering the spindle. Rotational speed was varied from 0.5 to 100 rpm. Since a different speed was optimum at each temperature, the viscosity reading was used when the digital reading was 10% of the maximum range available for the given spindle/speed combination. (Results are shown in Fig. 55.26.) The data were fitted empirically to give the relationship

$$\ln(\eta/\eta_i) = 1.03 \times 10^7 (1/T)^2 - 4.69 \times 10^4 (1/T) + 51.33, \quad (1)$$

where  $\eta$  is the viscosity in centipoise,  $\eta_i$  is the viscosity in centipoise at the isotropic temperature, and  $T$  is the absolute temperature ( $^{\circ}\text{K}$ ). The temperature was maintained using a circulating-water jacket;<sup>8</sup> the water-bath temperature supplying the jacket was controllable to  $\pm 0.01^{\circ}\text{C}$  accuracy. Our results showed no sharp change in viscosity at the nematic/isotropic transition, as has been reported by others for lyotropic polymers<sup>9</sup> and for thermotropic LMLC's.<sup>10</sup> At the N/I transition, the apparent viscosity was  $6.78 \pm 0.25 \times 10^3$  cp ( $6.78 \pm 0.25$  Pa-s). At room temperature ( $22^{\circ}\text{C}$ ), the empirical fit projects an apparent viscosity of  $3 \times 10^8$  cp ( $3 \times 10^5$  Pa-s), comparable to taffy. These data confirm that flow and alignment can be accomplished at elevated temperatures with the alignment "frozen in" at a glass transition at or above room temperature.

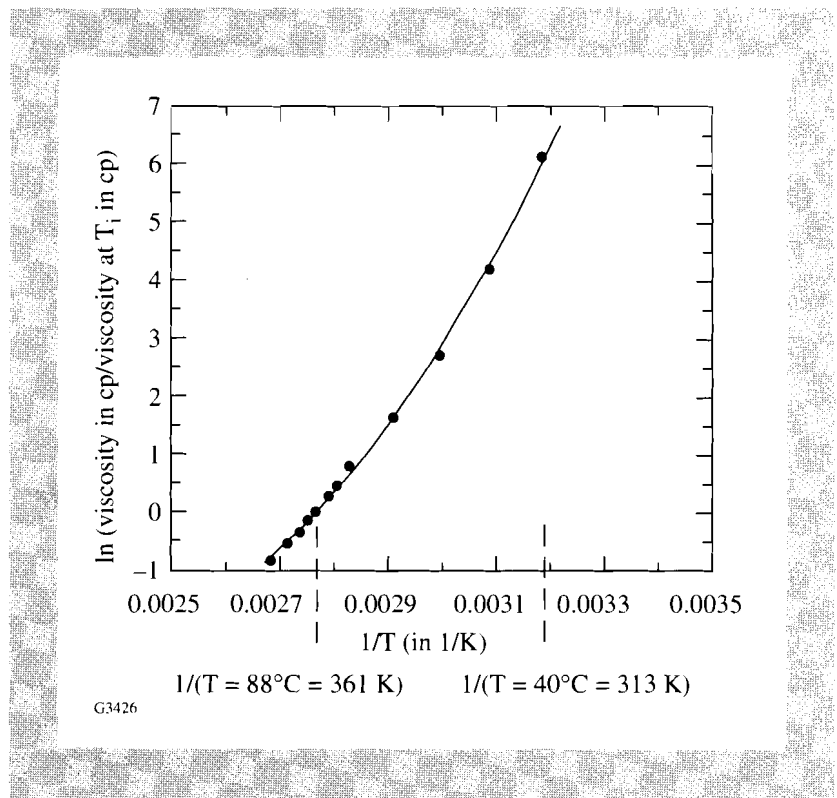


Fig. 55.26  
Temperature dependence of NPLC viscosity. Viscosity is determined as a function of temperature using a rotating-spindle-type viscometer. Measurements for temperatures below  $80^{\circ}\text{C}$  are made using a T-bar spindle with helical path action. Measurements for temperatures at and above  $80^{\circ}\text{C}$  are made using a disc-type spindle and no helical action.

### 3. Birefringence Measurement: Method and Results

The birefringence of the NPLC must be accurately known to construct a wave plate with the desired retardance. Measurements of the ordinary and extraordinary refractive indices were performed using a commercial Abbe refractometer.<sup>11</sup> The refractometer was calibrated<sup>12</sup> with a fused-silica standard at each wavelength/temperature combination used. Due to the high viscosity of LC360N at room temperature, placing it directly on the refractometer stage is inconvenient, and polymer alignment is difficult. For this side-chain polysiloxane, the side chains are responsible for the birefringence. Without an alignment layer on the substrate, the side chains align homeotropically. When a rubbed alignment layer is used, the side chains align along the rub direction.<sup>13</sup> We chose the latter configuration since alignment quality could be checked quickly by viewing between crossed polarizers. The refractive indices were determined with a cell constructed by sandwiching the NPLC between  $S_1$ , a high-index glass plate (SF4,  $n_D = 1.76$ ), and  $S_2$ , a low-index glass plate (microscope slide,  $n_D = 1.5$ ) [see Fig. 55.27(a) inset], both of which had been prepared with a nylon 6/6 alignment layer in the following manner:

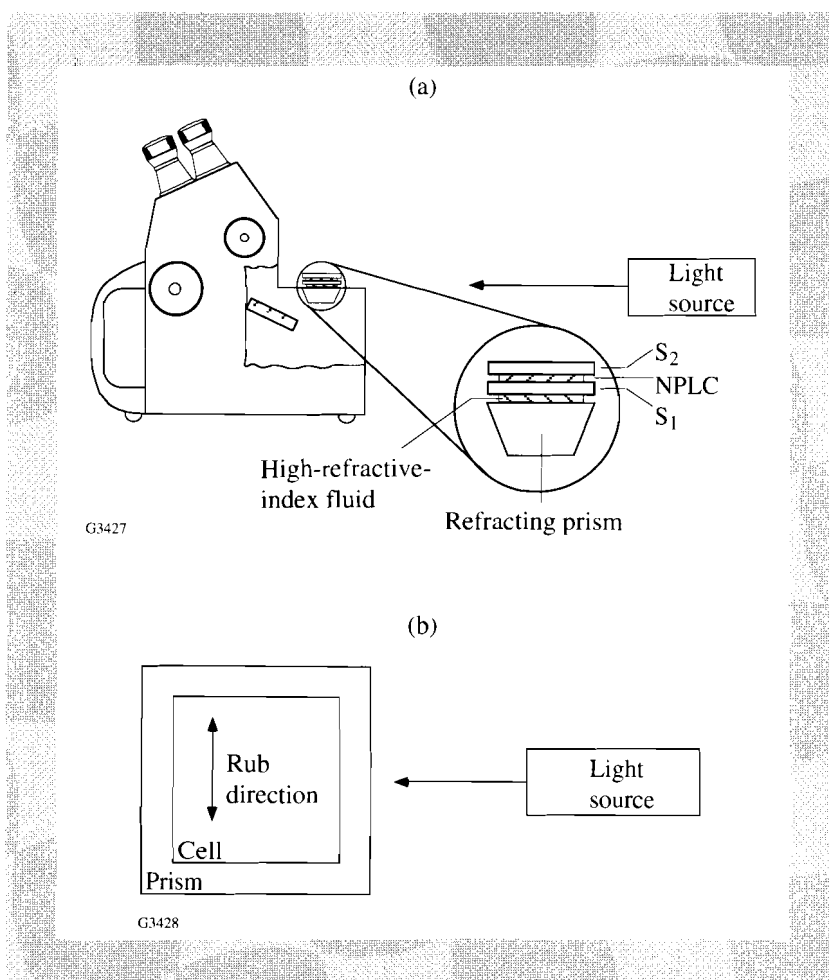
The glass substrate surfaces intended for contacting the NPLC were covered with 88% (reagent grade) formic acid for 30 s, spun at 1900 rpm for 60 s, then covered with a 0.2% solution of nylon 6/6 in 88% formic acid for 60 s and spun at 1900 rpm for 2 min. The coated substrates were heated on a programmable hotplate<sup>14</sup> at 115°C (15°C above the boiling point of formic acid to ensure complete evaporation of the solvent) for 1½ h and allowed to cool to room temperature. The coated substrate was buffed by a device developed in-house (at LLE). It consisted of a spinning (2000 rpm) cylinder, 25 cm long and 10 cm in diameter and covered with a polyaramide fiber sheet.<sup>15</sup> The substrate was held to a platform by vacuum and then passed beneath the rotating cylinder. The height of the roller was adjusted until passing the substrate under the stationary roller just caused light behind the roller to be extinguished. The direction of buffing was defined as the direction of the roller motion (same as movement of the platform for first pass). The substrate was passed forward and backward under the spinning roller four times.

The NPLC and the SF4 plate were heated to 100°C. The NPLC was dabbed by microspatula onto the SF4 plate and covered with the unheated, low-index plate so that the rub directions of the substrates were antiparallel. No spacers were used. This cell was placed directly on a hotplate, held at 88°C ( $T_i$ ) for 24 h, and then cooled from 88°C to 20°C at a rate of 1°C/h. Using a contact micrometer,<sup>16</sup> the thickness of the NPLC layer was determined to be approximately 20 µm. The same sandwich cell was used for all birefringence measurements.

$S_1$  was mounted on the very-high-index ( $n_D = 1.92$ ) refractometer prism with a fluid whose refractive index was  $n_D = 1.81$ .<sup>17</sup> The Abbe refractometer and sample arrangement are shown in Fig. 55.27(a). Although the flatness of substrates  $S_1$  and  $S_2$  was poorer than  $4\lambda$  at 633 nm, the NPLC alignment quality was sufficient for the measurements. The index of  $S_2$  was not critical. (If the index of  $S_2$  happened to be higher than the NPLC,  $S_2$  would not couple light into the sandwich cell, and the existence of  $S_2$  would simply not register.) The cell was

Fig. 55.27

Schematic diagram of Abbe refractometer and sample. (a) The refracting prism has the highest refractive index; index-matching fluid has a refractive index between  $S_1$  and the refracting prism;  $S_1$  is a high-index glass substrate; NPLC is the nematic polymer liquid crystal aligned by thermal annealing between substrates prepared with a rubbed polymer alignment layer;  $S_2$  is a glass substrate of arbitrary refractive index. Source light is directed through the sample onto a mirror and then to the observer. The mirror is rotated to detect the critical angle used to calculate the refractive index. (b) The sample cell is oriented on the Abbe prism with the direction of buffing orthogonal to the incoming light beam.



oriented on the refractometer stage such that the light from the source would sample both the ordinary and extraordinary indices. The rub direction was orthogonal to the incoming light beam [see Fig. 55.27(b)]. Both  $n_o$  and  $n_e$  measurements were read in this configuration; five trials of each were averaged.

The ordinary and extraordinary refractive indices were measured at  $20^\circ\text{C}$  for various wavelengths. The indices, their average values

$$\left\{ n_{\text{av}} = \left[ \frac{2n_o^2 + n_e^2}{3} \right]^{1/2} \right\}$$

and the birefringence values are shown with their standard deviations,  $\sigma_{N-1}$ , in Table 55.II. The light sources used were sodium lamp, mercury lamp, HeNe laser, and Nd:YLF laser. The sodium and mercury sources were unpolarized. The polarized HeNe and Nd:YLF beams were passed through a diffuser to randomize the polarization. The Abbe refractometer makes use of the critical-angle relationship of the sample with the refractometer prism. The observer sees a split light-field, darker where the critical angle for a given sample index is exceeded. The lighter part of the field of view is illuminated by the light source. To see the split field when using an IR source, a hand-held IR scope<sup>18</sup> was held at the

Table 55.II: Refractive indices of NPLC at 20°C.

Source	Wavelength (nm)	$n_o$	$n_e$	$\Delta n$	$n_{av}$
Hg	546.1	1.5320±0.0002	1.6960±0.0004	0.1640±0.0006	1.5885±0.0003
Na	589.6	1.5269±0.00005	1.6864±0.0003	0.1595±0.00035	1.5819±0.0001
HeNe	632.8	1.5251±0.0002	1.6816±0.0003	0.1565±0.0005	1.5790±0.0002
Nd:YLF	1054	1.5132±0.0002	1.6584±0.0002	0.1452±0.0004	1.5631±0.0002

eyepiece, and measurements were then made in the usual manner. Three points ( $\lambda = 546.1, 632.8,$  and  $1054$  nm) were used to fit these data to the Cauchy equation:

$$n = A + B/\lambda^2 + C/\lambda^4 \quad (2)$$

The coefficients for  $n_o$  and  $n_e$  are shown in Table 55.III. The individual curves in Fig. 55.28(a) were subtracted point by point to give the birefringence dispersion curve in Fig. 55.28(b). The birefringence dispersion of crystalline quartz,<sup>19</sup> shown in Fig. 55.28(b) for comparison, is approximately 15 times smaller than that of LC360N.

The refractive indices were determined at 1054 nm for various temperatures. Temperature was maintained using a circulating-water bath<sup>8</sup> around the refracting prism. These indices are listed in Table 55.IV. The temperature dependence of the ordinary and extraordinary indices is shown in Fig. 55.29(a). The temperature dependence of the birefringence of our NPLC (LC360N) and that of several other LC's are listed in Table 55.V and plotted on Fig. 55.29(b). Other LC's shown are another NPLC (methylstilbene PLC<sup>20</sup>) but at 589.6 nm, an LMLC (K15<sup>21,22</sup>) at 1054 nm, an LLE mixture (60% 18523 and 40% 14627<sup>3,22</sup> by weight) at 1047 nm, and an LMLC (E200<sup>22</sup>) at 1047 nm.

Table 55.III: Coefficients of Cauchy equation for dispersion of ordinary and extraordinary indices of refraction for NPLC at 20°C.

	A	B	C
$n_o$	1.5071	$6.6064 \times 10^3$	$2.4866 \times 10^8$
$n_e$	1.6474	$1.1344 \times 10^4$	$9.3661 \times 10^8$

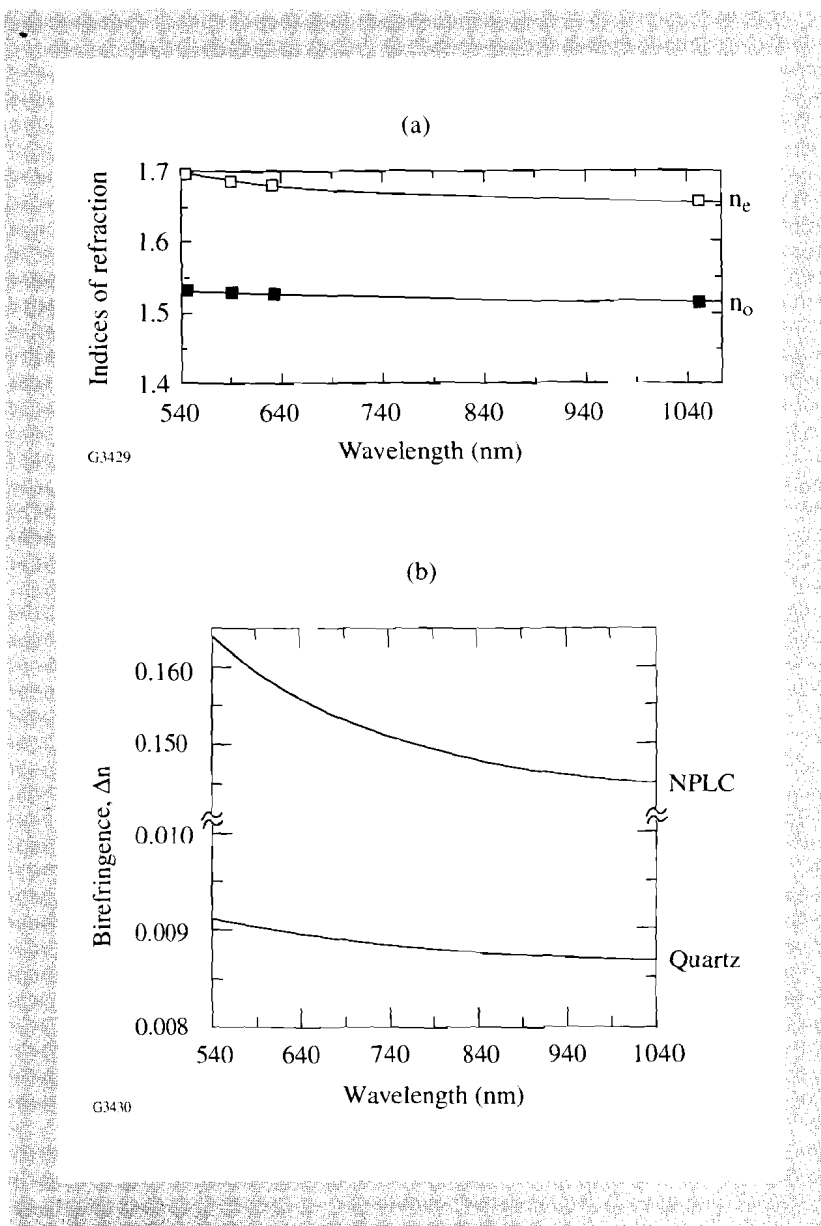


Fig. 55.28 Dispersion of refractive index of NPLC. (a) The ordinary and extraordinary refractive indices of the NPLC are fitted separately to the Cauchy equation. (b) The ordinary and extraordinary indices curves are subtracted point by point to yield the dispersion curve. All index dispersion measurements are determined at 20°C. Birefringence dispersion for crystalline quartz<sup>19</sup> is shown for the same range.

For LC360N, an empirical second-order polynomial fit of birefringence versus temperature (°C) yields a  $d(\Delta n)/dT$  at 20°C of  $(-).00003/^\circ\text{C}$ . At room temperature, the birefringence change per degree is within the standard deviation of the birefringence value. A wave plate made with this NPLC would show a variation in retardance at room temperature of only 0.3 nm/°C per micron of polymer thickness. In a zero-order half-wave plate, this represents a retardance

change per °C of only 0.15 nm. By comparison, the methylstilbene polymer shows a variation in retardance of 0.03 nm/°C/μm but, due to its lower birefringence, would require a thicker cell to produce the same retardance as our NPLC. The LMLC's show a wide variation of the temperature dependence of birefringence. The LMLC K15 exhibits a very large birefringence change with temperature at 20°C. This is to be expected since its clearing temperature is approximately 33°C and the  $d(\Delta n)/dT$  of every LC increases sharply near its own isotropic temperature. The second example of an LMLC is an in-house (LLE) wave-plate mixture (60% 18523 and 40% 14627). This mixture has been used for LC optical devices at LLE and has proven to be convenient for conventional LC cell construction. The mixture does, however, show a higher birefringence change with temperature than does the NPLC LC360N and, for half-wave-plate construction at 1054 nm, would exhibit a slightly higher retardance change

Table 55.IV: Temperature dependence of refractive indices of NPLC at  $\lambda = 1054$  nm.

Temperature (°C)	$n_o$	$n_e$	$\Delta n$	$n_{av}$
20	1.5132±0.0002	1.6584±0.0002	0.1452±0.0004	1.5631±0.0002
30	1.5127±0.0002	1.6523±0.0002	0.1396±0.0004	1.5606±0.0002
40	1.5115±0.0001	1.6447±0.0002	0.1332±0.0003	1.5572±0.0001
50	1.5113±0.0003	1.6364±0.0002	0.1251±0.0005	1.5541±0.0003
60	1.5116±0.0002	1.6270±0.0001	0.1154±0.0003	1.5510±0.0002
70	1.5120±0.0001	1.6105±0.0004	0.0985±0.0005	1.5455±0.0002

with temperature. Finally, a newer LMLC, E200, shows a  $d(\Delta n)/dT$  at 20°C of (-)0.00009/°C, an order of magnitude smaller than our NPLC. A zero-order half-wave plate made of this LMLC would show only one-third the birefringence change of LC360N, but such a cell would require an external epoxy seal. Our NPLC shows promise for providing temperature-stable retardance in a thin, self-sealing cell.

### Wave-Plate Construction

This section describes the fabrication of NPLC wave plates using various substrate and spacer arrangements. All work with formic acid was performed in a Class 10 fume hood in a Class 1000 clean room. All cell construction, excluding degassing, was performed in a Class 10 laminar flow hood in a Class 1000 clean room.

For the double-substrate wave plates, our target retardance using an 18-μm-thick path length was 2614 nm. This provided a second-order retardance of 506 nm, i.e., a second-order half-wave plate at 1054 nm.

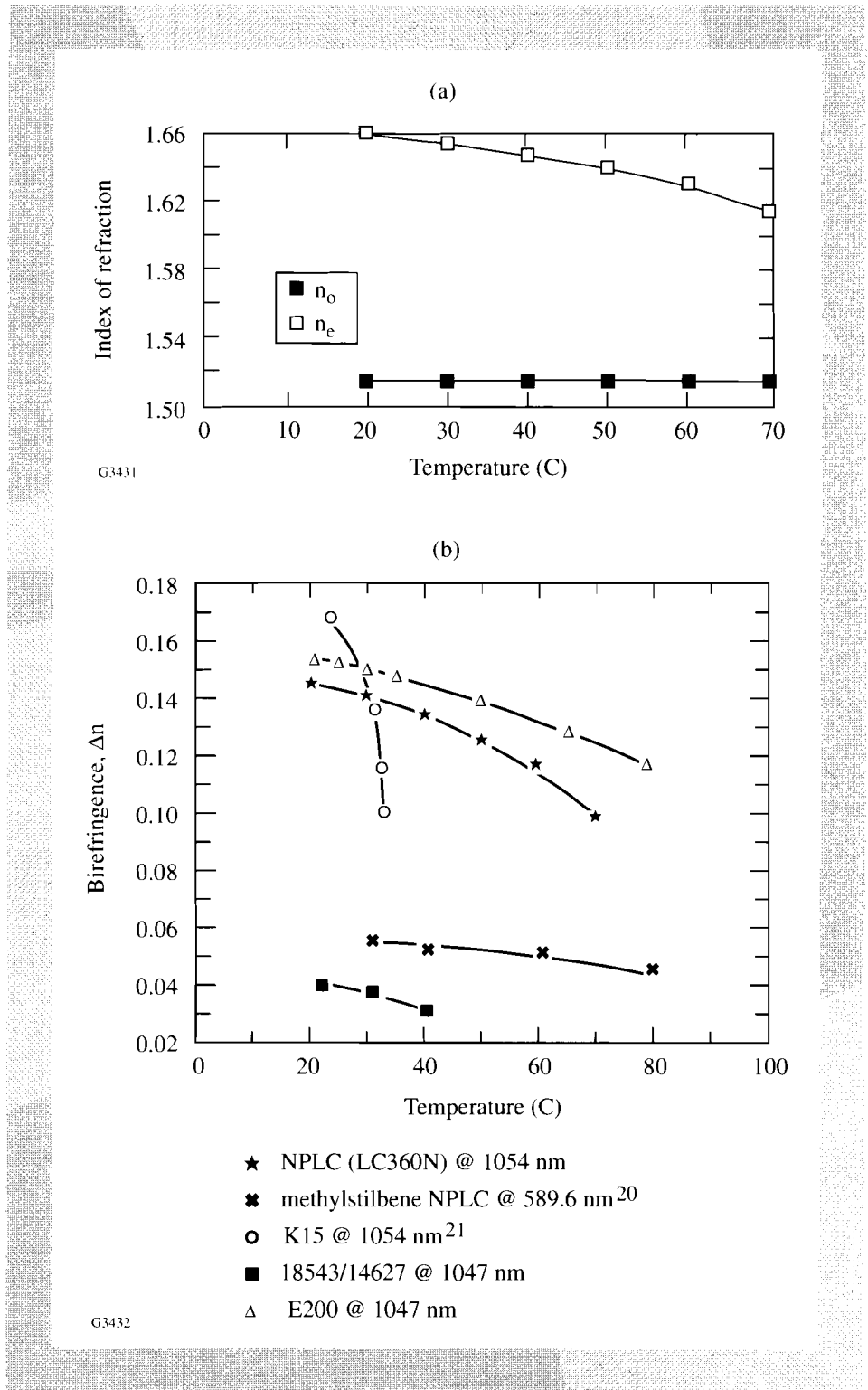


Fig. 55.29

Temperature dependence of refractive index for NPLC. (a)  $n_e$  and  $n_o$  between  $T = 20^\circ\text{C}$  and  $T = 70^\circ\text{C}$ . (b)  $\Delta n$  between  $T = 20^\circ\text{C}$  and  $T = 70^\circ\text{C}$ , compared to literature and measured data for several other LC compounds.

Table 55.V: Comparison of temperature dependence of birefringence of LC360N with other LC materials.

Material	LC360N	methylstilbene PLC	K15	60%18523 + 40% 14627	E200
Form	NPLC	NPLC	LMLC	LMLC	LMLC
$T_i$	88°C	~100°C	33°C	~50°C	88.5°C
$\lambda$	1054 nm	589.6 nm	1054 nm	1047 nm	1047 nm
$\Delta n$ at 20°C	0.1452	0.057	0.168	0.042	0.152
$d(\Delta n)/dT$ at 20°C (1/°C)	$-2.755 \times 10^{-4}$	$-2.970 \times 10^{-5}$	$\sim -4.18 \times 10^{-3}$	$-3.35 \times 10^{-4}$	$-9.492 \times 10^{-5}$
$d(t\Delta n)/dT$ per $\mu\text{m}$ at 20°C (nm/°C/ $\mu\text{m}$ )	-0.2755	-0.0297	$\sim -4.18$	-0.335	-0.0942
$d(t\Delta n)/dT$ for $t = 527$ nm and 20°C (nm/°C/ $\mu\text{m}$ )	-0.1452	---	-2.202	-0.1766	-0.0496
Reference	---	20	21, 22	3, 22	22

### 1. Double-Substrate, Fiber-Spacer Homogeneous Distribution

The thickness of the NPLC layer was fixed using commercially available glass fiber spacers<sup>23</sup> mixed into the polymer. The fiber-spacer diameters were  $18 \pm 0.3 \mu\text{m}$  and lengths varied from 20 to 100  $\mu\text{m}$ . The fiber spacers were added to the polymer for a calculated yield of approximately 150 spacers in the completed cell (0.8 mg of fibers to 3.2 g of polymer). Homogeneous distribution of the fibers was achieved by heating the mixture to 100°C and stirring mechanically for 15 min. A small amount of the mixture was removed with a stirring rod and smeared onto a bare microscope slide. This smear was checked under a light microscope for homogeneous distribution (i.e., no clumping) of the fibers. Stirring introduced bubbles into the mixture, so it was degassed at 100°C and <1 Torr until bubbles were no longer visible (about 1 h for the given mass of polymer). The vacuum was applied gradually, 250 Torr every 15 min, to prevent excessive foaming of the NPLC.

The wave-plate substrates were two 50-mm-diam, 7-mm-thick borosilicate glass (BK7) discs polished to a surface flatness of better than  $\lambda/10$  P-V at 633 nm. Both were coated with a nylon 6/6 alignment layer using the procedure described under "3. Birefringence Measurement . . .". One substrate was heated to 100°C.

The polymer was separately heated to 100°C and scooped onto the substrate using a metal microspatula. The other substrate was kept at room temperature so that it could be lowered by hand onto the polymer. The rub directions of the substrates were antiparallel. The constructed cell was degassed at 100°C and <1 Torr for 24 h to remove trapped air bubbles. The cell was placed on a 5-mm-thick silica square, loaded onto a hotplate, covered with a Pyrex glass dish, held at 88°C for 24 h, and then cooled from 88°C to 20°C at 1°C/h. This was the same annealing protocol used for the birefringence measurement cell.

The completed cell had approximately 75 fibers distributed over the full aperture. There was little distortion of the NPLC alignment around these fibers as shown by viewing at 100X magnification between crossed polarizers [see Fig. 55.30(a)]. Annealing removed all evidence of fluid flow around the spacers.

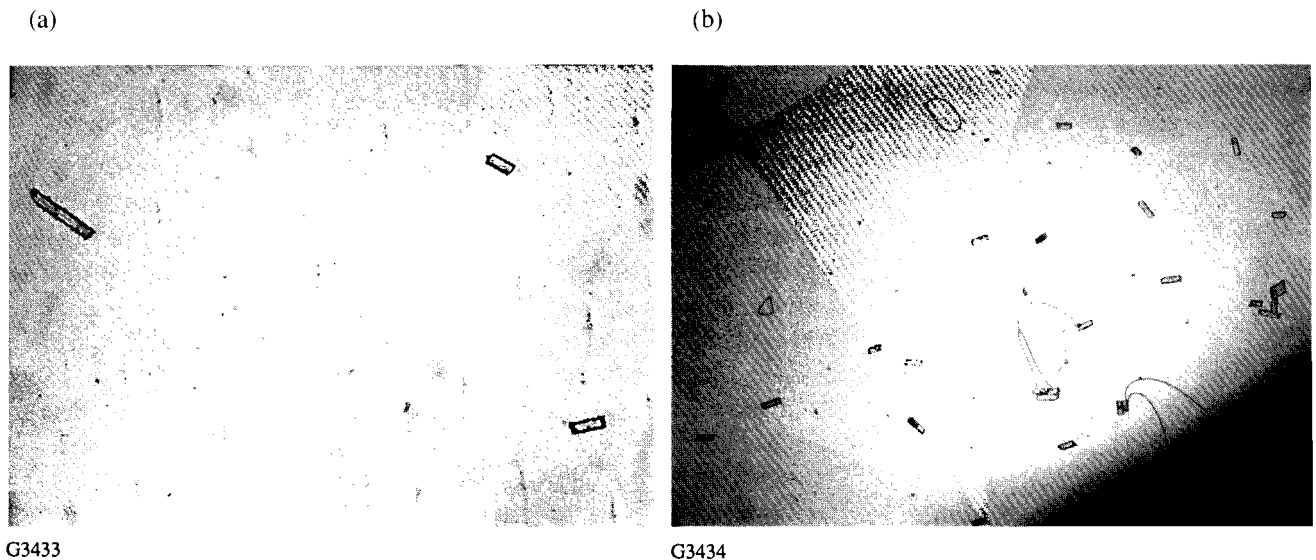


Fig. 55.30

Glass fiber spacers (18- $\mu\text{m}$  diam) in double-substrate wave plates. (a) Photograph at 100X magnification between crossed polarizers shows three fibers in a 0.8-mm<sup>2</sup> area in the double-substrate wave plate with homogeneous fiber distribution. There are no apparent disclinations. (b) Photograph at 50X magnification between crossed polarizers shows fibers in a 3-mm<sup>2</sup> area in double-substrate wave plate with fiber-spacer annulus. These fibers and the disclinations surrounding them are outside the clear aperture of the wave plate. Other features in both photomicrographs may be attributed to dirt or buffing marks.

## 2. Double-Substrate, Fiber-Spacer Annulus

An alternative technique was employed to keep the fiber spacers out of the wave plate's clear aperture where they might otherwise provide sites for laser damage or contribute to gradients in the transmitted optical wavefront. The fibers were applied in an annulus after the alignment layer had been applied and buffed. For 50-mm-diam BK7 substrates, a 32-mm-diam glass mask was placed over the clear aperture. The fibers were applied by dipping a cotton swab into the fibers, tapping them off above the substrate, and removing the mask; then the NPLC was applied by scooping it at 100°C onto the clear aperture of the substrate also held

at 100°C. As described in the preceding subsection, the procedure then continued with construction of the double-substrate cell. Both parallel and antiparallel construction were tested. Retardance values of the parallel and antiparallel cells were comparable, but total tilt angle varied [see “2. Wave-Plate Evaluation” in the next section].

The density of fibers in the annular region was high. Figure 55.30(b) (photograph taken at 50X magnification between crossed polarizers) shows a density of approximately 15 fibers per mm<sup>2</sup>. This contributed to the formation of lines of disclination, but this effect was confined to the annulus outside of the clear aperture and did not affect transmitted-wavefront quality or measured retardance.

### 3. Single Substrate

In addition to the methods described above for sandwich-type NPLC wave plates, we developed a method for producing single-substrate wave plates. Since a large proportion of the cost of any high-quality LC device is attributed to the substrates, a single-substrate wave plate essentially halves the expense of the device. A single substrate was prepared with an alignment layer as described previously. The single substrates used here were 12 mm thick.

The first procedure tested was spin-coating a solution of the NPLC in chloroform solvent (5% w/w) onto the buffed substrate. Solvent alone was dripped by syringe onto the substrate and allowed to sit for 30 s. The substrate was then spun at 1800 rpm while dripping solvent (1 ml) onto the substrate for a total spin of 60 s. Then the 5% solution was dripped by syringe onto the substrate, allowed to sit for 60 s, spun at room temperature at 1800 rpm again dripping 1 ml of the solution for the initial part of the spin, for a total spin of 120 s. The single substrate was annealed under the same protocol as the double-substrate cells. Viewing between crossed polarizers showed alignment and visual transmission/extinction contrast; however, retardance measurements by laser ratiometer were within the system noise levels, suggesting that the NPLC layer was too thin to measure. Microscopic examination showed beading of the NPLC along the rub direction. Higher concentrations did not spin on uniformly.

A second method was attempted that involved dripping the NPLC/chloroform solution onto the buffed substrate and allowing the solvent to evaporate, leaving behind the NPLC layer. Low concentrations (<7%) evaporated so rapidly that the NPLC was deposited in uneven patches. Evaporation of higher-concentration solutions left a polymer-layer barrier at the air/solution interface that precluded further evaporation.

Consequently, the NPLC had to be applied directly to the buffed substrate in the following way: The substrate was placed on a silica square and heated to 100°C. NPLC at 100°C was scooped along one edge to form a crescent. A stainless steel rod of wound stainless steel wire,<sup>24</sup> designed to give a thickness of 6 μm, was used to stroke the NPLC across the substrate either parallel or perpendicular to the buff direction for a given trial. To prevent sliding of the substrate, glass tacks were epoxied at one corner of the silica square. The cell was transferred to a plain silica square, held in an oven at 88°C for 1 h, then allowed

to cool to room temperature (average rate of cooling was  $\sim 20^{\circ}\text{C}/\text{h}$ ). Longer heating (2 h) with slower annealing ( $3^{\circ}\text{C}/\text{h}$ ) showed no improvement in uniformity or alignment. There was no significant difference in uniformity or alignment between single-substrate cells made with flat ( $PV < \lambda/10$ ) and nonflat ( $PV \sim 5\lambda$ ) substrates, nor for stroking of NPLC with the steel rod perpendicular versus parallel to the rub direction. Neither the bulk NPLC nor that on the substrate was degassed since previous experiments with degassing showed no improvement in appearance.

All trials showed a residual outline of the original crescent-shaped NPLC application region. Partial removal of this nonuniformity was achieved by using a combination of application techniques. A buffed substrate sitting on a silica square with glass tacks at one corner was heated to  $100^{\circ}\text{C}$ . The NPLC, also at  $100^{\circ}\text{C}$ , was scooped onto the center of the substrate. A small brush was used to spread the NPLC smoothly over the surface. Brush strokes were either parallel or perpendicular to the buff direction for a given trial. As described above, the warmed rod was drawn across the surface to promote uniform thickness. This cell was held at  $110^{\circ}\text{C}$  for 15 min. The hot cell was then spun at 4000 rpm for 30 s to evenly distribute the NPLC over the substrate and to remove any residual brush or rod lines. (This process step dictated the use of thick, single substrates. Their large heat capacity ensured that the NPLC was warm enough to flow during the entire spin.) This cell was held in an oven as before at  $88^{\circ}\text{C}$  for 1 h, then allowed to cool to room temperature. The brush did introduce some air bubbles, but they disappeared during the 1 h of heating.

### Wave-Plate Evaluation

The optical quality of a wave plate depends on undistorted wavefront transmission over the clear aperture and on accuracy and uniformity of retardance. Constructed wave plates were first viewed between crossed polarizers for uniformity of transmission and extinction.

Table 55.VI gives transmitted-wavefront distortion with and without the NPLC; retardance; tilt angle at center and over the clear apertures (75% of the hard apertures); and thickness calculated from total retardance and tilt angle<sup>25</sup> for all three types of wave plates.

#### 1. Transmitted Wavefront

Transmitted wavefront was measured using a Fizeau interferometer<sup>26</sup> at  $\lambda = 633 \text{ nm}$ . To establish a transmitted-wavefront reference, the substrates ultimately used in the double-substrate configuration were first assembled with  $5\text{-}\mu\text{m}$  Mylar<sup>27</sup> spacers and index-matching fluid<sup>17</sup> ( $n_D = 1.516$ ). Three external glass tacks, epoxied across the sides of the substrates, maintained the cell structure for interferometry. The transmitted-wavefront quality of this “mock” cell was used as a standard of comparison for the double-substrate cell subsequently assembled. The reference for the single substrate was the substrate itself.

Transmitted-wavefront distortion for all three types of cells varied from 2 to 4 times that of the blank cell. One double-substrate cell, stored vertically for one month, showed transmitted-wavefront improvement of about  $0.1 \lambda$ . Such

Table 55.VI: Results of wave-plate evaluations.

Wave Plate	Double-Substrate, Homogeneous Fiber Distribution	Double-Substrate, Fiber Annulus	Single Substrate
@ 633 nm			
Transmitted wavefront distortion, no NPLC (reference)	$0.073 \pm 0.015 \lambda$	$0.073 \pm 0.015 \lambda$	$0.781 \pm 0.043 \lambda$
Transmitted wavefront distortion, NPLC	$0.404 \pm 0.050 \lambda$	$0.382 \pm 0.048 \lambda$	$1.544 \pm 0.237 \lambda$
@ 1054 nm			
Retardance design goal	$506 \pm 40$ nm (second order)	$506 \pm 40$ nm (second order)	----
Measured average retardance	$496.9 \pm 11.3$ nm (second order)	$510 \pm 28$ nm (second order)	$416 \pm 42$ nm (first order)
Tilt angle (single spot)	$2.36 \pm 0.31^\circ$	$0.37 \pm 0.15^\circ$	$0.5 \pm 0.5^\circ$
Average tilt angle (nine spots)	$1.31 \pm 0.95^\circ$	$0.11 \pm 0.09^\circ$	$0.6 \pm 0.3^\circ$
Thickness based on retardance and tilt angle	$17.95 \pm 0.08 \mu\text{m}$	$18.03 \pm 0.19 \mu\text{m}$	$10.13 \pm 0.28 \mu\text{m}$

improvement might be desirable but points out the susceptibility of an NPLC like LC360N to flow under the influence of gravity when the glass transition temperature is too near room temperature.

## 2. Retardance

a. Value and variation. Retardance was measured using a laser ratiometer with a Soleil-Babinet compensator<sup>28</sup> between crossed Glan-Thompson calcite polarizers. The approximate laser-beam diameter at the cell location was 2 mm. The retardance order was established by the fiber-spacer diameter. Nine spots were measured and averaged. Single-spot retardance was measured five times at the center to establish reproducibility. Variation was no more than  $\pm 5$  nm for all types of wave plates.

Both types of double-substrate wave plates showed excellent agreement of expected and average measured retardance values. Due to the near-room-temperature glass transition of the NPLC, any manipulation of the cell by hand contributed to some degradation of retardation uniformity. Retardance uniformity was most dependent on fiber-spacer distribution. In the homogeneous distribution

type, as few as 75 spacers over the aperture provided excellent gap uniformity [see Fig. 55.31(a)]. In the fiber annulus distribution type, the density of fibers was more difficult to control. Regions of excessive fiber deposition led to more severe gap wedges [see Fig. 55.31(b)]. More uniform and reproducible gaps were obtained by swabbing fibers directly onto the exposed substrate around the mask than by tapping from a swab. However, direct swabbing scratched the nylon alignment layer, creating regions of scattering that sometimes extended into the clear aperture.

The single-substrate wave plate showed fairly good uniformity over most of the clear aperture. Variations in thickness, i.e., wedge, were commonly caused by unevenness of stroking with the hand-coater rod [see Fig. 55.31(c)].

For use in a laser system, a retardance deviation of no more than  $\pm 10\%$  of the calculated value is desirable.<sup>29</sup> All three types of wave plates showed this accuracy when averaged over the aperture. However, this specification presumes uniformity across the clear aperture. Only the double-substrate wave plate, having fiber spacers in homogeneous distribution, showed sufficient uniformity for use in a high-peak-power laser system. Improved uniformity of other wave-plate types may be expected with refinements in the application of (a) fibers, in the case of the annular-distribution double-substrate wave plate, or (b) NPLC, in the case of the single-substrate wave plate.

**b. Tilt angle.** Tilt angle is the angle that the side chains of the NPLC make with respect to the substrate surface. The tilt angle was measured at the center of the cell for reproducibility tests and at nine spots for uniformity tests using a phase-retardation method<sup>25</sup> in which the cell is rotated around an axis perpendicular to the incident beam in a laser ratiometer.

Because the tilt-angle measurement is an average through the cell, parallel construction of the double-substrate cells yielded tilt-angle measurements of almost zero, whereas antiparallel construction led to tilt-angle measurements of  $2^\circ$ – $3^\circ$ . This is consistent with the induced tilt angle being the same at both inner surfaces.<sup>30</sup> The tilt of the side chains at the first surface induces a slight retardance on the incident beam. In parallel construction, this beam then encounters side chains at the second surface that are tilted in the opposite direction compensating for the retardance. As the cell is rotated around an axis perpendicular to the incident-beam, a minimum in transmission indicates a matching of the incident-beam polarization with the side-chain tilt. For the parallel cell, this minimum occurs at normal incidence, where retardance of one surface just compensates the other. In antiparallel construction, no such compensation takes place, in which case a minimum in transmission occurs at an off-normal angle if side-chain tilt exists. Table 55.VI reports the tilt angles for (1) a double-substrate wave plate with homogeneous distribution of fibers and antiparallel construction and (2) a double-substrate wave plate with fibers in an annular distribution and parallel construction. The tilt angle of the NPLC on the single substrate was negligible.

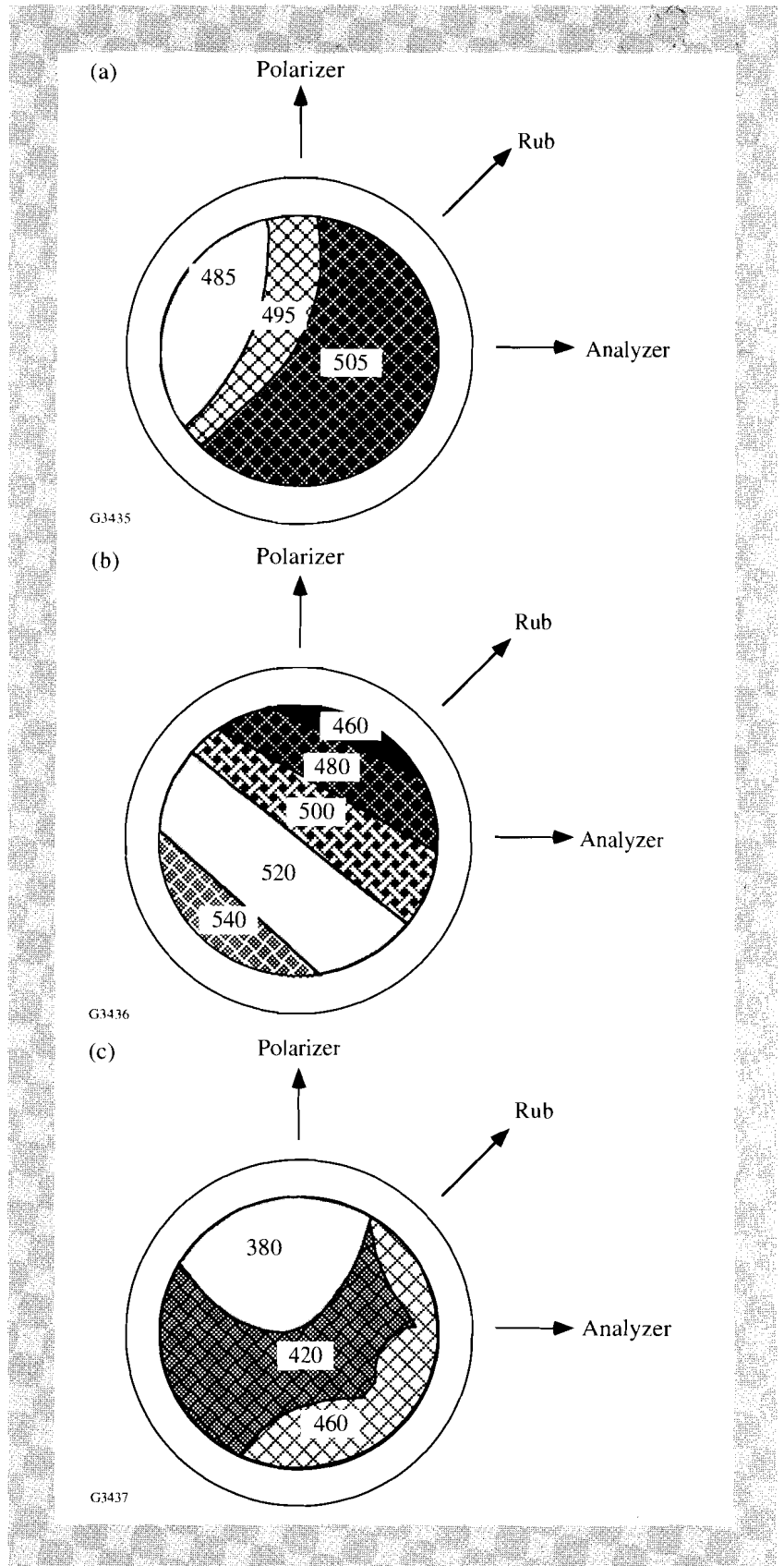


Fig. 55.31 Wave-plate retardance contour maps. Retardance is measured using a Soleil-Babinet compensator. (a) Double-substrate homogeneous fibers—values shown represent  $\pm 5$  nm of second-order retardance within the indicated region; (b) double-substrate fiber annulus—values shown represent  $\pm 10$  nm of second-order retardance within the indicated region; (c) single substrate—values shown represent  $\pm 20$  nm of first-order retardance within the indicated region.

**c. Thickness.** Since there was a range in diameters of fiber spacers used for the double-substrate cells, total retardance was used to calculate the thickness of the NPLC, and the fiber thickness was used to establish the order of retardance. The retardance used for thickness calculations had to be corrected for that retardance due to tilt angle.<sup>25</sup> The thicknesses shown in Table 55.VI are based on these corrected total-retardance values. Even without the correction, measured thickness values of the NPLC layer were well within the range established by the fiber-spacer diameter. This result implies that the fibers maintained the cell gap without trapping any NPLC between the fiber and the substrate.

### **Laser-Damage Resistance**

The NPLC wave plates constructed and evaluated above provide numerous advantages over both traditional crystalline solids and low-molecular-weight liquid crystals for typical optical uses. However, the particular NPLC used for this study provided yet another advantageous property—high laser-damage resistance.

The laser-damage resistance of the LC360N was measured at 1054 nm by a technique described in greater detail elsewhere.<sup>2</sup> The NPLC was dissolved in toluene (at 2% w/w solids content) and sprayed by airbrush onto the small face of a 30-60-90 BK7 prism, the geometry of which prevents back reflection and subsequent interference effects. Both 1-on-1 and *N*-on-1 tests were made. In 1-on-1 tests, a single laser pulse is incident on a previously nonirradiated site. The energy within the pulse is gradually increased at each new location until damage is seen. In *N*-on-1 testing, laser pulses of increasing energy are incident on the same site at 5-s intervals until damage is seen. The laser used was a Nd:glass, mode-locked, feedback-controlled, Q-switched oscillator, whose 1054-nm pulses could be frequency-tripled to 351 nm using KDP. Pulses were  $1 \pm 0.1$  ns in duration in the IR (3 J/pulse). Damage was diagnosed as the appearance, within the 3-mm-diam irradiation spot size, of a bubble that scattered light. Under Nomarski microscopic inspection [Fig. 55.32(a)], the NPLC exhibited apparent multiple-clustered pitting.

The original brown sample of LC360N was contaminated with traces of a polymerization catalyst believed to be colloidal metallic platinum with considerable potential for causing laser damage. After purification to 1 ppm Pt by column chromatography (purification carried out by Wacker Chemie), the clear, colorless polymer showed a much-improved laser-damage resistance, and the laser-damage sites showed far less severe pitting [see Fig. 55.32(b)].

The laser-damage test data are reported in Table 55.VII. The films used in damage testing were 2.5 times thicker than the NPLC in the second-order wave plates and 13 times thicker than an NPLC layer required for a zero-order wave plate. Since laser-damage resistance can be expected to improve for thinner layers, damage thresholds for NPLC wave plates in a working system would likely be even higher than those reported here. The laser-damage measurements of a nylon alignment layer,<sup>3</sup> buffed under both hard and light conditions, show resistance of 5 to 10 J/cm<sup>2</sup> (Table 55.VII). Damage-resistance levels of several J/cm<sup>2</sup> are compatible for use in many high-peak-power laser applications. The components of an NPLC wave plate with a nylon alignment layer meet this specification.

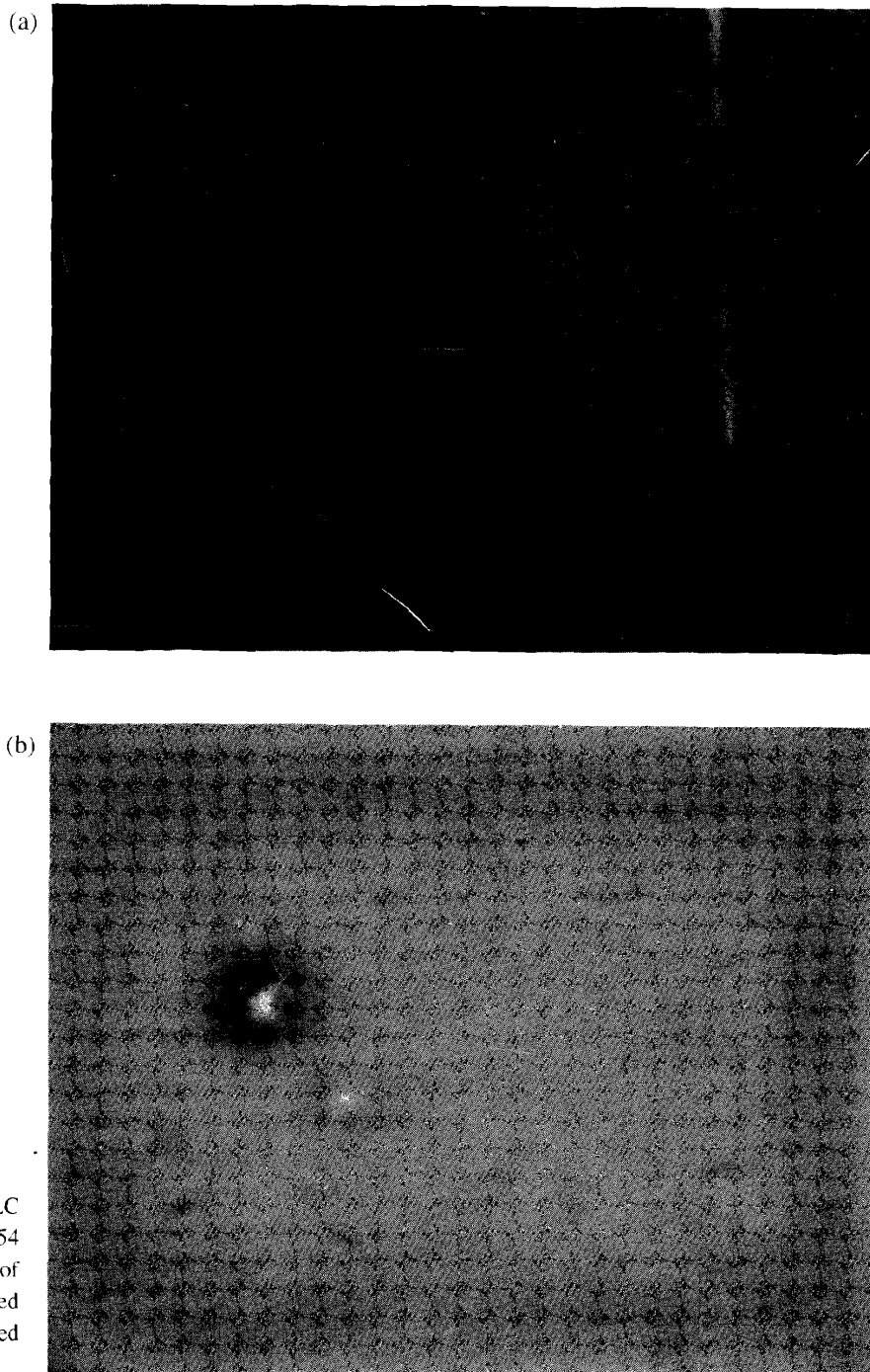


Fig. 55.32  
Nomarski photomicrographs (100X) of NPLC after irradiation with a 1-ns laser pulse at 1054 nm. (a) Extensive pitting in a 16- $\mu\text{m}$  layer of unpurified material (39 ppm Pt). (b) Reduced incidence of damage in a 45- $\mu\text{m}$  layer of purified material (1.0 ppm Pt).

G3438

### Summary

We have developed techniques for using a nematic polymer liquid crystal in the construction of a wave plate. These techniques include measurement of the birefringence of the highly viscous NPLC and alignment by thermal annealing against a buffed nylon 6/6 aligning layer. We were able to construct three types of wave plates—double substrate with fiber spacers distributed homogeneously;

Table 55.VII: Laser-damage resistance of nematic polymer LC360N and nylon 6/6.

Pattern	Material	Damage Threshold (J/cm <sup>2</sup> ) @ 1 ns, 1054 nm
I-on-I	16- $\mu$ m film, unpurified	1.0 $\pm$ 0.1
N-on-I		0.8 $\pm$ 0.1
I-on-I	45- $\mu$ m film, purified to 1 ppm Pt	1.4 $\pm$ 0.2
N-on-I		3.2 $\pm$ 0.3
I-on-I	nylon 6/6, light buff	5.5 $\pm$ 0.9
	nylon 6/6, hard buff	6.57 $\pm$ 0.07
N-on-I	nylon 6/6, light buff	9.5 $\pm$ 0.4
	nylon 6/6, hard buff	5.9 $\pm$ 0.8

double substrate with fiber spacers distributed in an annulus; and single substrate. The viscosity/temperature behavior of the NPLC allowed alignment at higher temperatures but configuration stability at lower (room) temperature. The NPLC acted as its own adhesive to seal the confining substrates together. The high laser-damage resistance of the NPLC indicates that it and similar materials will prove useful for high-peak-power laser applications.

The wave plates showed promising uniformity and transmitted-wavefront quality as well as the capability of meeting specific retardance requirements at a cost determined mainly by the glass substrates. Further improvements in device stability could be obtained by using an NPLC with a higher glass-transition temperature (>40°C to ensure a "locked-in" configuration at room temperature, to allow greater ease of handling, and to eliminate long-term flow under the influence of gravity). If the NPLC had a positive dielectric anisotropy ( $\Delta\epsilon$ ), molecular alignment would be facilitated by allowing annealing in the presence of an electric field.

#### ACKNOWLEDGMENT

The authors wish to thank Mark J. Guardalben for providing photographs of damaged NPLC; Kenneth L. Marshall for discussions regarding NPLC alignment and manuscript preparation; and Semyon Papernov for discussion of damage-testing methodology. This work was supported by the U.S. Department of Energy Office of Inertial Confinement Fusion under Cooperative Agreement No. DE-FC03-92SF19460, the University of Rochester, and the New York State Energy Research and Development Authority. The support of DOE does not constitute an endorsement by DOE of the views expressed in this article.

## REFERENCES

1. S. D. Jacobs, K. A. Cerqua, K. L. Marshall, A. Schmid, M. J. Guardalben, and K. J. Skerrett, *J. Opt. Soc. Am. B* **5**, 1962 (1988).
2. M. Guardalben, A. Bevin, K. Marshall, A. Schmid, and F. Kreuzer, in *Laser Induced Damage in Optical Materials: 1988*, Natl. Inst. Stand. Technol. (U.S.), Spec. Publ. 775 (U.S. Government Printing Office, Washington, DC, 1989), pp. 462–469.
3. A. L. Rigatti, D. M. Dudek, R. G. Carnes, L. D. Lund, K. L. Marshall, S. Papernov, A. W. Schmid, D. J. Smith, and S. D. Jacobs, presented at CLEO '93, Baltimore, MD, 2–7 May 1993.
4. S. D. Jacobs, K. L. Marshall, and K. A. Cerqua, U. S. Patent No. 5,054,888 (8 October 1991).
5. Nylon 6/6 (polyhexamethylene adipamide) pellets, Polysciences, Inc., Warrington, PA 18976, Cat. #6557.
6. LC360N, nematic polymer liquid crystal provided through F. Kreuzer in association with Wacker Chemie, Munich.
7. Brookfield Digital Viscometer Model DV-II equipped with Helipath Stand. The T-bar-type spindle used was T-F, #96; the disc spindle was RV6.
8. Lauda Refrigerating Circulator, Model RMS6, Brinkman Instruments, Inc., Cantiague Road, Westbury, NY 11590.
9. M. C. Muir and R. S. Porter, *Mol. Cryst. Liq. Cryst.* **169**, 83 (1989).
10. G. Marrucci, in *Liquid Crystallinity in Polymers: Principles and Fundamental Properties*, edited by A. Ciferri (VCH Publishers, New York, 1991), Chap. 11.
11. Bellingham and Stanley Model 60/HR Abbe Refractometer, Bellingham and Stanley Limited, Longfield Road, North Farm Industrial Estate, Tunbridge Wells, Kent TN2 3EY, England.
12. Bellingham and Stanley Calibration Tables for Abbe Refractometer Model 60/HR.
13. J. Kelly Houghton (unpublished research results).
14. Dataplate Digital Hot Plate/Stirrer, PMC Industries, Inc., 6335 Ferris Square, San Diego, CA 92121-3208.
15. TexTech Industries, Main Street, North Monmouth, ME 04265.
16. Digimatic Indicator IDC Series 543, Mitutoyo Corporation, 31-19, Shiba 5-chome, Minato-ku, Tokyo 108, Japan.
17. R. P. Cargille Laboratories, Inc., Cedar Grove, NJ.
18. Find-R-Scope, FJW#84499 (maximum range of wavelength sensitivity is 1.2  $\mu\text{m}$ ), FJW Optical Systems, Inc., 629 South Vermont Street, Palatine, IL 60067.

19. J. M. Bennett and A. T. Glassman, in *CRC Handbook of Laser Science and Technology, Section 1.4: Optical Materials*, edited by M. J. Weber (CRC Press, Boca Raton, FL, 1986), Vol. IV, Part 2: Properties, p. 227.
20. N. A. Vaz *et al.*, *Mol. Cryst. Liq. Cryst.* **198**, 305 (1991).
21. K. C. Chu, C. K. Chen, and Y. R. Shen, *Mol. Cryst. Liq. Cryst.* **59**, 97 (1980).
22. Nematic LMLC's, EM Industries, Inc., Advanced Chemical Division, 5 Skyline Drive, Hawthorne, NY 10532.
23. Ultra Precision Glass Fibers, EM Industries, Inc., Advanced Chemical Division, 5 Skyline Drive, Hawthorne, NY 10532. 18- $\mu$ m fiber spacers - Cat. #111357.
24. K Hand Coater, RK Print-Coat Instruments Ltd., South View Laboratories, Litlington, Royston, Herts SG8 0QZ.
25. H. L. Ong, *J. Appl. Phys.* **71**, 140 (1992).
26. Zygo Mark IVxp, Zygo Corporation, Laurel Brook Road, P.O. Box 448, Middlefield, CT 06455-0448.
27. Mylar (polyethylene terephthalate), DuPont Company, Electronics Department, MYLAR Customer Service, Barley Mill Plaza, P.O. Box 80019, Wilmington, DE 19880-0019.
28. Soleil-Babinet Compensator Model 8-400, Special Optics, 101 E. Main Street, P.O. Box 163, Little Falls, NY 07424.
29. C. Cotton (private communication).
30. G. Baur, V. Wittwer, and D. W. Berreman, *Phys. Lett.* **56A**, 142 (1976).

## **Section 3**

# **LASER SYSTEM REPORT**

### **3.A GDL Facility Report**

During the second quarter of FY93 the refurbished GDL was activated in the infrared. As part of the activation, the new GDL produced 1 kJ of IR energy at a 20-cm aperture on 1 April 1993. The system is presently configured with 15- and 20-cm disk-geometry amplifiers, which were the prototypes for the OMEGA Upgrade, as the penultimate and ultimate amplifiers. These two final stages are driven by conventional-design OMEGA rod-geometry amplifiers.

The refurbished GDL also features a new front-end driver line, which consists of an optical-fiber-fed, regenerative amplifier that drives a large-aperture (40-mm) ring amplifier (LARA). This architecture provides improved reliability over conventional master-oscillator, power-amplifier (MOPA) designs in a very compact package. GDL will ultimately have two of these driver lines to implement co-propagation.

Plans for the third quarter of FY93 include testing co-propagation in the infrared portion of the laser system. Construction of the GDL facility will also continue. One of two KDP plates that will convert the infrared pulse to the ultraviolet is in-house in preparation for coating. Components for the final spatial filter and alignment sensor package are slated to be assembled early in the third quarter. During the third quarter the old OMEGA target chamber, which has been installed on a new base in GDL, will be outfitted with vacuum components; the remainder of integration will continue throughout the fourth quarter.

### 3.B The Upgrade to the OMEGA Laser System

The upgrade to the OMEGA laser system will provide a unique capability to validate high-performance, direct-drive laser-fusion targets. The ultimate goal of the experimental program on the OMEGA Upgrade is to study the physics of hot-spot formation under near-ignition conditions (ignition scaling), using cryogenic targets whose hydrodynamic behavior scales to that of high-gain targets. Specific performance goals of these experiments are the achievement of a convergence ratio ( $C_R$ )  $\geq 20$ , an ion temperature ( $T_i$ ) of 2 to 3 keV, and a total fuel areal density ( $\rho R$ ) in excess of  $0.2 \text{ g/cm}^2$  for targets whose Rayleigh-Taylor growth factors are in excess of 500. In this article, the top-level specifications required for these experiments will be presented along with the constraints they place on the laser system. The configuration of the laser system and the target-irradiation facility will be reviewed, as will the control system.

#### System Specifications

The conceptual design for the OMEGA Upgrade was completed in 1989 and resulted in a preliminary design document (Title I).<sup>1</sup> Since completion of that document, a number of changes have been made to the laser system to optimize the configuration and performance. This article will describe the most recent configuration of the laser system and explain its design.

The total energy, uniformity, and pulse-shaping requirements for the proposed ignition-scaling experiments call for a 60-beam system, which will produce 30 kJ on target in temporally shaped pulses with peak powers in excess of 40 TW. The upgraded system will fit into the existing building, will allow for maximum use of existing hardware, and will satisfy budgetary constraints. The top-level performance requirements for this system are given in Table 55.VIII.

A key parameter of this system is the number of beams on target. The 60-beam configuration has been adopted as it provides a significant improvement of uniformity over the existing 24-beam system with minimal additional complexity. The 60 beams are sufficient to meet theoretical uniformity requirements, and compared to systems with fewer beams, the 60-beam system provides a lower sensitivity to individual beam characteristics. In addition, the beam aperture required to supply 30 kJ in 60 beam lines is sufficiently small that beam segmentation can be avoided, allowing the use of optical components with reasonable cost per unit area.

#### Co-Propagation and Pulse Shaping

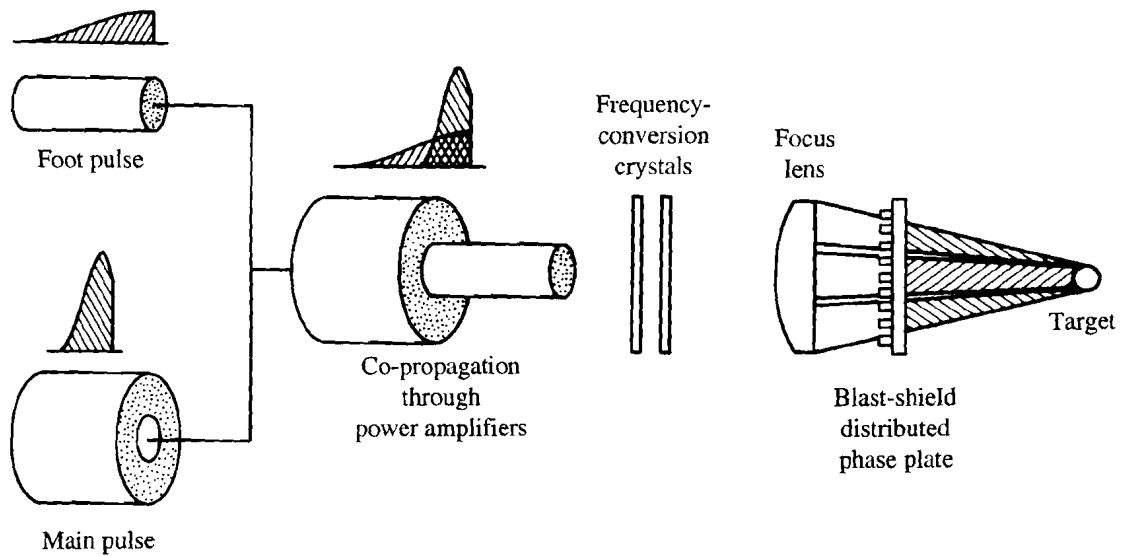
The shaped pulse required for an efficient ablative target implosion presents a significant problem because of the limited dynamic range of practical frequency-tripling schemes. The solution incorporated into the upgrade design is the co-propagation, through the laser system, of two spatially separated pulses. In this design, a small-diameter foot pulse, of circular cross section, co-axially propagates inside an annular main pulse (Fig. 55.33). The two pulses are separated by a null zone that has no laser light propagating in it. By concentrating the low-power portion of the pulse in the foot, the intensity of both the main and foot pulses can

be matched for efficient frequency conversion. While this benefit in conversion efficiency is about equal to the losses inherent in the null zone, co-propagation will be used in the upgrade because it offers attractive opportunities for pulse shaping and laser-uniformity schemes.

Table 55.VIII: OMEGA Upgrade design goals.

Energy on target	Up to 30 kJ (pulse shaped)
Wavelength	351 nm (third harmonic of Nd:glass)
Lasing medium	Nd-doped phosphate glass
Number of beams	60
On-target irradiation uniformity	1%–2% rms
Diagnostic solid angle	$\pi$ sr
Repetition rate	1 shot/h

G3499



TC2691

Fig. 55.33  
Schematic of the co-propagated main- and foot-pulse beams for the OMEGA Upgrade.

Figure 55.34 is a scale drawing of the beam's cross section at the frequency-conversion crystals; the dark areas represent the nominal beam areas (where the beam is approximately flat topped), and the lighter shading indicates the transition regions where the intensity of each beam falls to zero, roughly as an order-eight super-Gaussian. The null zone, which contains no laser energy, is maintained between the pulses to allow for their separate diagnosis, to prevent constructive interference that could result if the beams were to overlap, and to minimize the risk of inadvertent damage to the system. It is important to note that this co-propagation configuration can be used to irradiate fusion targets only because distributed phase plates (DPP's) are used at the focus lenses: since each DPP element irradiates the whole target, the locations of the foot and main beams in the near field are immaterial.

Co-propagation begins at the front end of the laser system, where two oscillator pulses are first amplified in separate laser drivers and then appropriately apodized and combined into a single beam. This coaxial combination of separate pulses is maintained through the remainder of the laser system. The size of the UV beam and its aspect ratio are chosen so that the UV energy loading, multiplied by a safety factor to accommodate intensity modulations, does not exceed the damage threshold of the high-reflectance and anti-reflection coatings in the UV beam transport system.

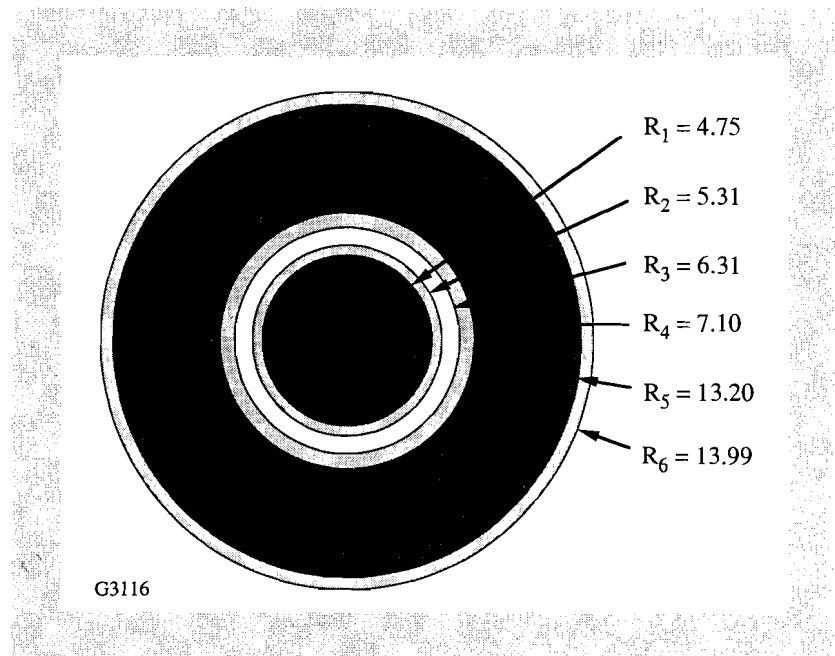


Fig. 55.34  
Cross section of beams at frequency-conversion crystals. All radii are given in centimeters; the null-zone thickness is 1 cm.

Each of the laser drivers will produce the applicable portion of the total pulse so that the desired shape results when the two are combined at the target. The base-line pulses needed for experiments are the picket-fence [Fig. 55.35(a)] and continuous [Fig. 55.35(b)] pulses. For picket-fence pulses it is natural to assign the final picket to the main beam and the other pickets to the foot. For the continuous pulse, there is flexibility in the definition of the split; Fig. 55.35(b) shows one possible division. The choice is made by balancing the need for higher foot-pulse intensity for frequency conversion with limits on the foot-pulse

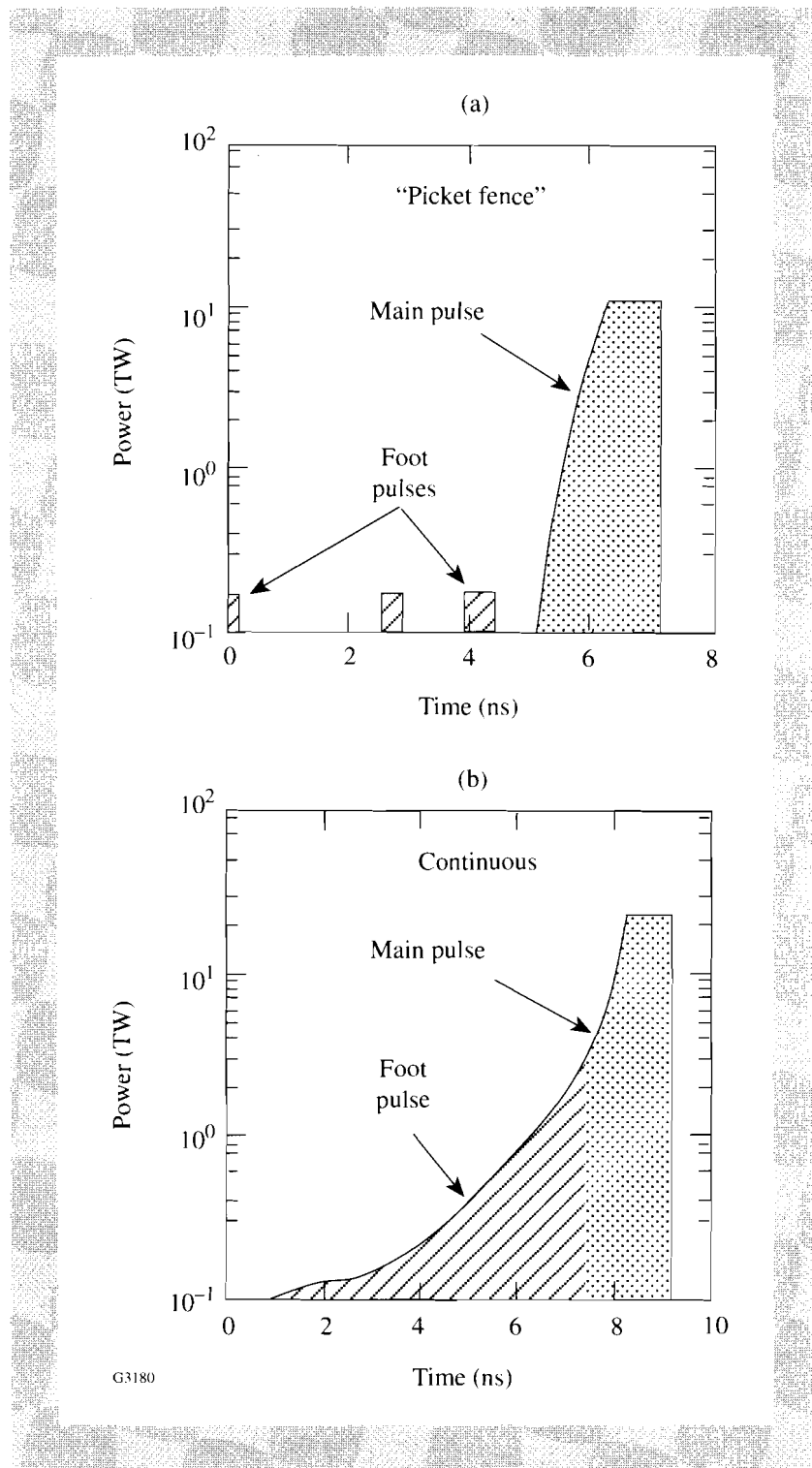


Fig. 55.35

The pulse shapes required for ignition-scaling experiments on the OMEGA Upgrade; (a) picket-fence pulse and (b) continuous pulse.

energy due to the UV damage threshold of the optical coatings. In the example of Fig. 55.35(b), the ratio of powers in the main and foot pulses of nearly 10:1 results in a ratio of intensities at the crystals of only  $\sim 1.4:1$ . This allows the use of a single-thickness KDP crystal for frequency conversion, the thickness of which is optimized primarily for the main pulse.

The overall energy performance predicted for the OMEGA Upgrade is shown in Table 55.IX. This table assumes a continuous pulse shape of the form shown in Fig. 55.35(b) and gives predictions for two peak powers, 23 TW and 39 TW. [The 39-TW pulse is a shortened version of the 23-TW pulse of Fig. 55.35(b) obtained by scaling the abscissa by a factor of 0.59 and keeping the energy constant.] That pulse shape is produced using a foot pulse with an approximately  $N$ th-order rise (with  $N \sim 2-4$ ) and a flat-topped main pulse with duration of 1.1 ns (23 TW) or 0.7 ns (39 TW). The laser performance for both the 23-TW and 39-TW cases was calculated by fixing the on-target UV energy, then working backwards through the system to obtain the IR performances for each case. The energies quoted are summed over the 60 beams and indicate that the IR system must produce  $\sim 1$  kJ per beam line. The UV numbers account for losses due to DPP's and the transport system. Since we expect that new technologies such as continuous phase plates<sup>2</sup> will have marked improvements in efficiencies, these values are quite conservative.

Table 55.IX: Energy performance of the OMEGA Upgrade.

	Main Pulse		Foot Pulse	
	23 TW	39 TW	23 TW	39 TW
Peak Power				
Beam area (cm <sup>2</sup> )	385		70	
UV: Energy on target (kJ)	26.5		3.5	
Energy on DPP (kJ)	33.5		4.4	
Energy after FCC (kJ)	36.9		4.9	
Average fluence after FCC	1.6 J/cm <sup>2</sup>		1.2 J/cm <sup>2</sup>	
Peak fluence after FCC	2.9 J/cm <sup>2</sup>		2.2 J/cm <sup>2</sup>	
Conversion efficiency (1.2-cm-thick crystals)	76.5%	84.6%	42%	52%
IR: Energy before FCC (kJ)	48.2	43.6	11.8	9.4
Avg. fluence before FCC	2.0 J/cm <sup>2</sup>	1.8 J/cm <sup>2</sup>	2.6 J/cm <sup>2</sup>	2.1 J/cm <sup>2</sup>
Peak fluence before FCC	3.6 J/cm <sup>2</sup>	3.2 J/cm <sup>2</sup>	4.7 J/cm <sup>2</sup>	3.8 J/cm <sup>2</sup>

G3500

The peak fluence in the UV portion of the system is limited by the damage fluence of the transport mirrors, which is  $2.9 \text{ J/cm}^2$  at  $0.7 \text{ ns}$ . This value is assumed to scale only weakly with temporal pulse width and is therefore applicable to both main pulses ( $23 \text{ TW}$  and  $39 \text{ TW}$ ). The average fluence is taken as  $0.56$  times the peak fluence based on experience at LLE and elsewhere.<sup>3</sup> Since the maximum fluence in the UV system occurs immediately after the FCC, the UV component most susceptible to damage is the first transport mirror immediately after the FCC.

### System Configuration

The overall layout of the upgrade is illustrated in Fig. 55.36. The need to fit all the hardware (including the extra amplifiers, the extra beamlines, and a larger target chamber) into existing building space has led to a substantial rearrangement of the OMEGA laser. The oscillators and preamplifiers, including the SSD and pulse-shaping hardware, are located in a room below the laser bay. The driver amplifiers will be located on the laser-bay level; there will be two sets of amplifiers, one each for the main and foot pulses. The apodizers and the mirror, which will combine the two beams into one, will also be located on the laser-bay level.

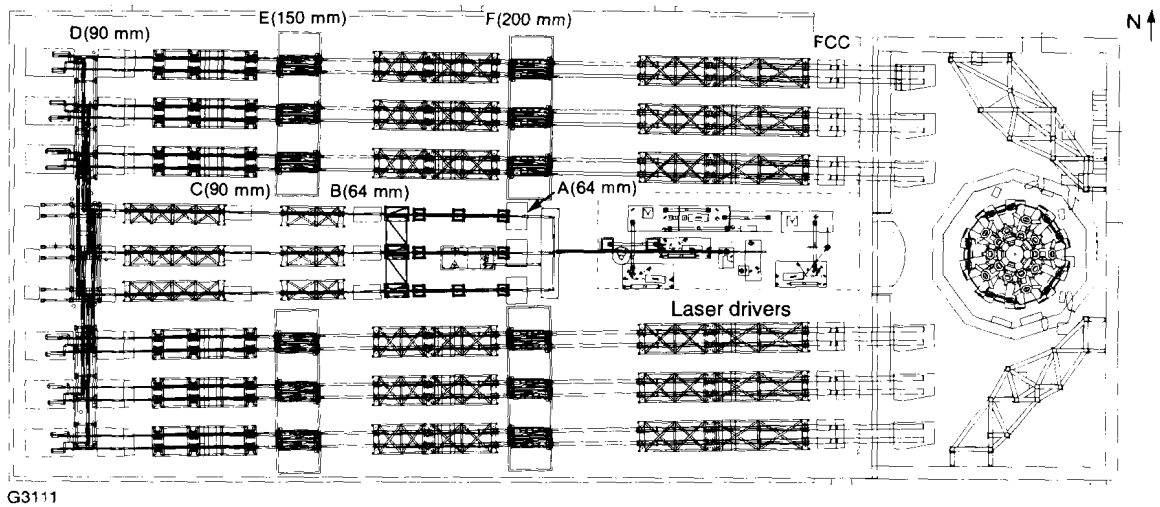


Fig. 55.36

Layout of the OMEGA Upgrade. The location of four stages of rod amplifiers (A–D), two stages of disk amplifiers (E, F), and the frequency-conversion crystals (FCC's) are indicated.

Once combined and amplified in the laser driver, the co-propagated beam is spatially filtered and then split three ways. Each beam is then amplified and split five ways, resulting in 15 beams. The amplifiers for both these stages (amplifier stages A and B of Fig. 55.36) are 64-mm rod amplifiers. All beam splitters are combined with an automated polarization-control wave plate that provides accurate energy balance between beams. The 15 beams are propagated through 90-mm OMEGA amplifiers (stage C) and spatial filters in the center of the bay in three stacks of five beams each. Each beam is split four ways at the end of the bay, at which point the 60 resulting beams pass through assemblies that permit  $\pm 1.5 \text{ m}$  of gross path-length adjustment needed to compensate for the inequality in transport paths to the target chamber and to provide precision beam-timing capability.

The 60 beams then propagate back along the outside of the laser bay in six clusters of ten beams (two wide, five high); each beam passes through another 90-mm rod amplifier (stage D) before being amplified by the stages E and F disk amplifiers (of diameters 150 mm and 200 mm, respectively). Both types of rod amplifiers (64 mm and 90 mm) are modified versions of the OMEGA amplifiers, which incorporate major portions of the parent assemblies. New glass laser rods will be installed on all amplifiers. The disk amplifiers have been designed and prototyped at LLE; their performance will be reviewed in the next issue of the LLE Review.

The outputs of the last amplifiers are spatially filtered, magnified, and passed through thin-film polarizers before reaching the frequency-conversion crystals. (The polarizers ensure that the correct linear polarization is incident upon the crystals in order to maximize conversion efficiency.) Back-reflected UV light is prevented from propagating backward through the laser system by a UV-absorbing window on the input of the frequency-conversion cells. After frequency conversion, the beams pass through the concrete shield wall and enter the target bay.

Next, the beam encounters the stage-F ASP, which is the alignment fiducial for the entire system. The ASP's are housed in six structures constructed of a cast epoxy/granite composite. These massive structures (10,000 kg each) are used to ensure the stability that facilitates alignment to 1- $\mu$ rad accuracy, which is required of the system. Also in these structures are the optical pick-offs, which distribute a fraction of the beam energy to the alignment and energy diagnostics. The harmonic-energy detectors (HED) are double-integrating spheres that measure the energies at the fundamental (1054-nm), second (527-nm), and third (351-nm) harmonics and provide individual measurements for the foot and main pulses. The alignment sensor package (ASP) provides the alignment reference to which IR and UV alignment beams are aligned; both beams are referenced to a position determined by the pulsed IR beam.

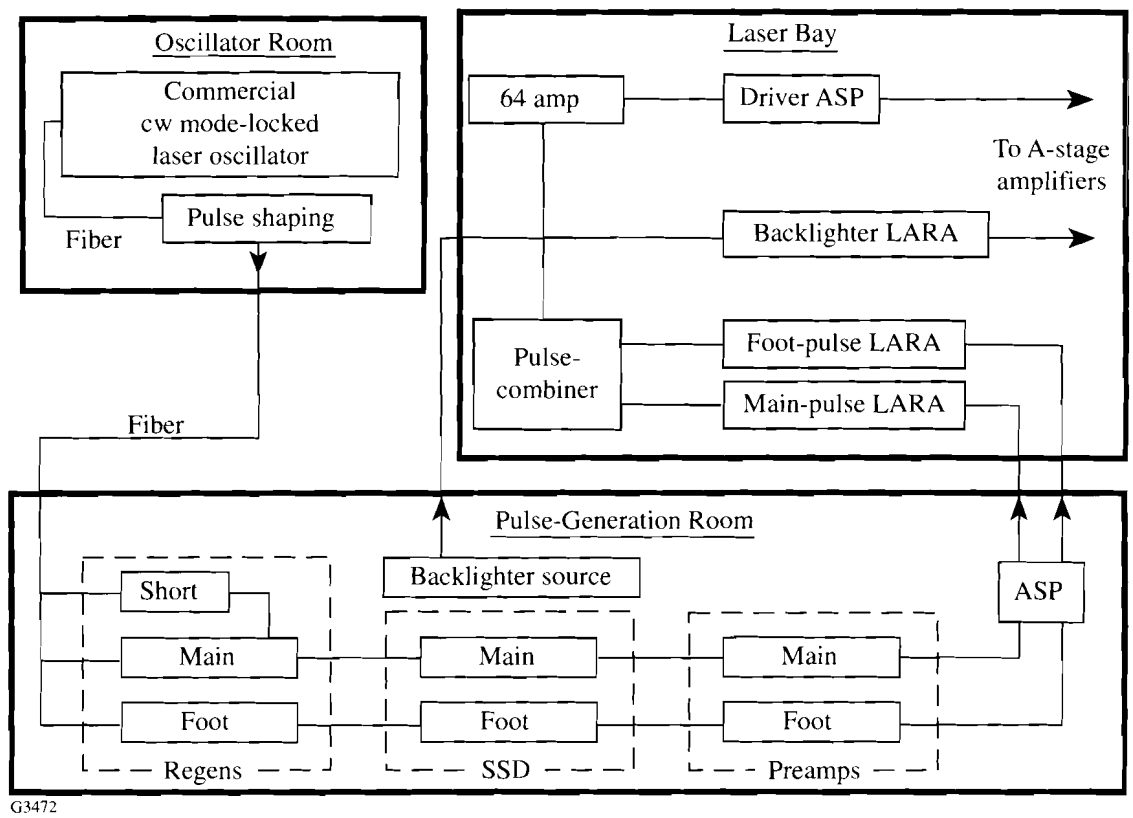
Beyond the stage-F ASP the beam is transported to the target chamber via two mirrors, the end mirror (on the beam axis) and the target mirror. The target mirror structure (TMS) supports the target mirrors plus the target chamber and its ancillary systems. These will be described in detail in a later section.

The 30 beams propagating toward the target bay on each side of the laser bay are all mutually parallel but angled at  $0.75^\circ$  toward the center of the laser bay. This angle is required to accommodate the nearly random mapping of the 60 beams onto the target chamber while limiting the incident angle on the end and target mirrors to  $60^\circ$  or less. Additional advantages of this wedged configuration are that it reduces the in-air path length of the UV transport system by 1.4 m (to 18 m), and it provides an additional 0.6 m between the outer beams and the shield wall in the target bay. The two-mirror UV-transport system was chosen to minimize the number of mirrors required and to reduce the path length of the UV beam. The former reduces cost; the latter reduces the chance that stimulated rotational Raman scattering (SRRS) will occur.

At each stage of the laser, spatial filtering is used to remove high-spatial-frequency noise in the beam and to ensure correct image relaying.<sup>4</sup> Image relaying is critical to the performance of laser beams with SSD because it prevents excessive excursions of different frequencies across the beam aperture. These deflections result from the frequency-dependent, grating-induced differences in propagation directions. It also prevents the formation of intensity modulations caused by interference effects. To further reduce interference effects, the size of the null zone between the foot and main pulses is chosen to be sufficient to prevent spatial overlap of the two pulses but is otherwise minimized to limit the aperture of disks and other optical components.

**Oscillators and Laser Drivers**

The driver for the Upgraded OMEGA laser will be comprised of several subsystems that supply co-propagated main and foot pulses for injection into the main beam lines, which contain the power amplifiers. Additional capability is provided to inject a third, backlighter pulse into 20 of the beam lines. The laser-driver subsystems, outlined in Fig. 55.37, are located in several areas: the oscillator room (OR), the pulse-generation room (PGR), and the *laser bay*.



G3472

Fig. 55.37 The laser-driver subsystem for the OMEGA Upgrade is located in three separate areas: the oscillator room, pulse-generation room, and central laser bay.

Pulses for the OMEGA system originate in the OR, where 80-ps-wide pulses, produced at a rate of ~76 MHz, originate from a commercially available mode-locked laser. At the outset of OMEGA operations these pulses will directly seed the regenerative amplifiers in the PGR. In addition to amplifying the pulses, those amplifiers will stretch the pulses to their desired lengths. Ultimately, the Upgrade will require complex pulse shapes that will be generated in the OR using either of two pulse-shaping methods: electro-optic or spectral filtering. Once implemented, these systems will generate the desired shape and length of the pulses (main and foot), and the regenerative amplifiers in the PGR will be used for amplification and timing only. The OR is physically remote (~20 m) from the PGR and is fiber optically coupled to the PGR. Fiber optics are used throughout the OR for flexibility and alignment insensitivity.

The PGR is a 36-ft × 19-ft room located below the laser bay and home of several major elements of the laser driver, including pulse switchout, regenerative amplification, pulse truncation, driver diagnostics, amplification, smoothing, and alignment. As shown in Fig. 55.37, the main-, foot-, and short-pulse regenerative amplifiers are seeded by pulses from the OR. The main and foot regenerative amplifiers increase the ~1.0-nJ energy of the input pulses to 0.1 mJ, using 40 round trips. The short-pulse regen creates a pulse of similar energy that can be used to fire electro-optic switches used to truncate the trailing edge of the main pulse. Various diagnostics measure the energy, timing, alignment, and stability of the regens. A master timing system, which is synchronously timed to the mode-locked seed laser, is used throughout the laser driver and laser system as a temporal reference.

Beyond the regenerative amplifiers the pulses encounter the electro-optic modulators and gratings required for the smoothing by spectral dispersion (SSD). These systems impress the bandwidth and angular dispersion required for high irradiation uniformity on target. To accommodate for any losses in these systems the pulses are further amplified (by as much as 10) in a preamplifier stage that is a single-pass, 7-mm amplifier in each of the main and foot pulse lines. The output of these amplifiers brings the pulses back up to the 0.1-mJ level.

To de-couple the sensitive PGR optical configuration from heat sources, much of the driver electronics are housed in a driver electronics room that has a separate HVAC system. Located in this room are the various timing circuits, high-speed Pockels cell drivers, and microwave generators needed by the PGR.

The PGR output (0.1 mJ) is directed, via a periscope, up to the next set of amplifiers, located on the laser-bay level. These amplifiers are 40-mm, large-aperture ring amplifiers (LARA's); one each is provided for the main, foot, and backlighter pulses. Each amplifier provides a gain of 5,000–10,000 in a total of four round trips, thereby producing a 0.6-J output pulse in each beamline. The foot and main pulses are coaxially combined co-propagation using a mirror that is reflective for the annular main pulse and transmissive for the circular foot pulse. Once combined, both beams are amplified to ~4 J each by a single 64-mm, single-pass amplifier (the last driver amplifier). Alignment of the pulses relative to the system and to each other is monitored at two separate locations. The first

alignment sensor package (ASP) is located in the driver area after the last amplifier. The laser-driver output is spatially filtered and propagated to the first beam splitter (stage A), where the laser-driver pulses are injected into the OMEGA power amplifiers. The stage-A ASP, located in this splitter, has a collimation monitor that is used to measure the collimation of the foot and main beams as well as that of the cw-IR alignment laser.

### Laser Amplifiers

A total of 93 rod amplifiers will be required for stages A–D. The 54 existing amplifier assemblies will be refitted with new glass rods and modified for use in the new system. The remaining 39 units will be fabricated from an updated design that will incorporate improvements to the existing amplifier. The disk amplifiers are of conventional box geometry<sup>5,6</sup> utilizing a 15-cm-diam stage E followed by a 20-cm-diam stage F, with each amplifier containing four disks. The clear aperture of the final amplifier is set by damage constraints, specifically the sol-gel anti-reflection coating on the input lens of the final spatial filter, which damages when the main pulse reaches  $9.8 \text{ J/cm}^2$ . The 15-cm stage provides a main-pulse saturated gain of 3.1, and the 20-cm stage a gain of 2.3. Saturated gains for the foot pulse are slightly lower because the longer pulse operates at a higher fluence. The performance of prototypes of the 15-cm and 20-cm disk amplifiers has recently been measured.<sup>7</sup> These prototypes have been used in the old OMEGA system and the recently completed GDL prototype beamline to verify that 1 kJ IR can be produced by these amplifiers.<sup>8</sup> These tests demonstrate that the upgraded OMEGA system will meet the IR energy specification.

For reasons of economy, the disk-amplifier design makes use of water-cooled flash lamps, which facilitate operation at a high storage efficiency. Both amplifier stages utilize the same power-conditioning and pulse-forming network. The cooling times for the disk amplifiers are sufficiently short to permit a 1-h shot cycle. The modular nature of the design allows for the rapid change of flash-lamp pump modules within this shot cycle.

### Target Area

The structure holding the target mirrors (see Fig. 55.38) is highly modular, with five-fold rotational symmetry about the vertical axis reflecting the soccer-ball symmetry, i.e., 20 hexagons and 12 pentagons. The 60 laser beams are located at the vertices of those polygons. The laser beams are directed through hexagonal tubes that are part of the structure. The design provides for segmented personnel platforms and integrates the optical mounts with structurally rigid, hexagonal beam tubes. The target mirrors are mounted on the ends of these beam tubes. The structure has a 6-m diameter, with the target mirrors centered on a 7.2-m diameter. The beam-transport geometry is such that no angle of incidence at either an end mirror or a target mirror exceeds  $60^\circ$ . The end mirrors are held on two, separate, space-frame structures (top and bottom of Fig. 55.36).

The target chamber, constructed of 5083-0 aluminum alloy, has an outer radius of 1.65 m and a 9-cm wall thickness. It has 60 beam ports (of 45-cm diameter) in the geometry mentioned; located at the centers of the soccer-ball polygons are 32 additional ports for diagnostics—20 of large diameter (60 cm)

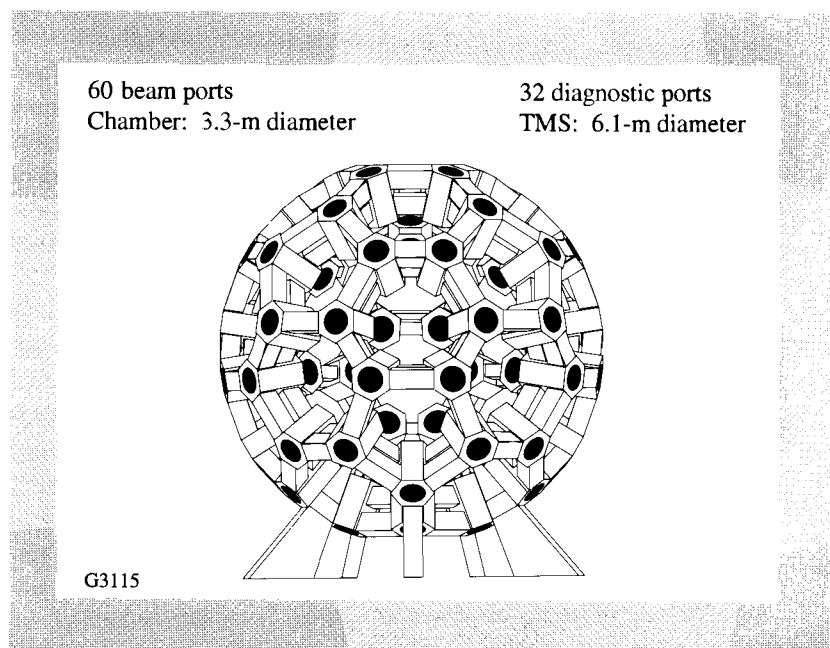


Fig. 55.38

The target-mirror support structure has a soccer-ball configuration and provides for diagnostic mounting and personnel access. The outer diameter is 6 m; the target mirrors will be mounted on a 7.2-m diameter.

on the hexagonal faces and 12 of smaller diameter (45 cm) on the pentagonal faces. The large diagnostic ports are particularly useful for instruments requiring a large, solid angle, such as a high-resolution, neutron time-of-flight spectrometer. Alternatively, these ports may be fitted with a reducing flange to allow use of existing OMEGA instruments or multiple, small diagnostics. The present complement of OMEGA diagnostics (with modifications where appropriate) will be available for the Upgrade. The Upgrade's target-area design actually allows a greater free volume for the placement of diagnostic instruments than is presently the case on OMEGA because in the Upgrade the beams are transported to the target-mirror structure from the outside rather than between the target mirrors and the target chamber.

### Alignment

The Upgrade alignment system uses two wavelengths, unlike the former system that was aligned in the IR from the oscillator to the target. While two wavelengths increase complexity, they eliminate the two disadvantages of single-wavelength alignment: the transport mirrors no longer need dual IR/UV coatings, and the focus lenses will not have to be translated ~109 mm after IR alignment to compensate for chromatic shift. The former improves the damage threshold of the UV coating; the latter improves the operational accuracy of alignment. The IR portion of the laser is aligned using a 1054-nm Nd:YLF laser, together with alignment sensor packages located at stages A, C, and F within each beam line. For alignment of the UV portion of the system, a full-aperture, 351-nm cw laser is injected into the beam just after the FCC's, using movable mirrors located in the target bay.

At the heart of the alignment system are 60, stage-F, alignment sensor packages, which utilize achromatic optics. Located in the target bay just prior to the beam-line end mirrors, these sensors view small fractions of the IR and UV beam energies reflected off the diagnostic pickoffs. These beams can be aligned

to each other and to a spatial fiducial. The injection of the UV beam is carried out sequentially by mobile injection mirrors located on the target-bay shield wall, each mirror servicing a column of five beam lines. After co-alignment with the IR beam, target alignment is performed by monitoring the UV reflections from a surrogate target transmitted back to a UV alignment table. This periscope mirror assembly (PMA) provides two beams (north and south) simultaneously, allowing the system to be aligned sequentially two beams at a time.

### **Laser Diagnostics and Control Systems**

The laser-alignment, diagnostic, and power-conditioning subsystems rely heavily on computer-control and data-acquisition systems. On the current OMEGA laser these systems have largely been independent; for the Upgrade, developments in network technology are used to facilitate high-speed communication between the different systems.

Central intelligence is distributed among three levels of computers: (1) a host computer (workstation), which is the core of the intelligence; (2) an intermediate computer (a PC), which performs network and translation functions; and (3) microprocessor-based controllers at the individual devices. The basis for this system is the use of a local operating network (LON), which places a Neuron<sup>®</sup> microprocessor from Echelon Corporation at each device. The configuration provides widespread parallel-processing capabilities, which facilitate rapid system alignment and operation. Global commands from the central computer are relayed by PC to the LON and out to the hardware devices. These devices act independently and are fully capable of carrying out relatively simple tasks without host intervention. The alignment system also uses an intermediate computer to operate clusters of frame grabbers. This computer processes the beam-alignment images obtained by the alignment sensor packages to determine alignment-error measurements. This information is sent back to the host computer where algorithms will command beamline realignment to remove the error. The power-conditioning system utilizes a similar hierarchy for subsystem control. Power conditioning has a separate LON, and each of the 213 laser amplifiers has its own microprocessor capable of managing the charging, firing, and diagnostics of the amplifier pulse-forming networks (PFN's). The laser-energy-measurement system will utilize a vendor data bus, such as VME or Fastbus, to acquire and reduce calorimetry and diode data acquisitions.

Beam-energy measurements are required at various points in the laser chain. The most important measurement is made just after the frequency-conversion crystals, where a Fresnel reflection from an uncoated surface of a pickoff transports 4% of the beam energy into a diagnostic package. The HED is similar to the multiwavelength, energy-sensing system currently used on OMEGA, except two integrating spheres are used, one for the main pulse and one for the foot pulse. The optical layout ensures that the co-propagated aperture is relayed to a hole in the rear surface of the first (main-pulse) integrating sphere, so that the foot pulse passes through to the second integrating sphere. Separate measurements are therefore possible for the main and foot pulses at all three wavelengths (1054 nm, 527 nm, and 351 nm).

To ascertain the UV energies actually incident on target, accurate measurements of the transport losses from the pickoff to the target are required for each beamline. The baseline is to measure the losses using a small, adjustable integrating sphere, which is inserted into the center of the target chamber and successively pointed in each of the 60 beam directions. A reference beam and ratiometer are used to characterize relative transmission of each beam line—the same method used in the old OMEGA system.

### Status of Project

Detailed design of the OMEGA Upgrade will be completed by October 1993. Contracts are in place for all of the major optical, laser, and structural components; shipments arrive daily. The building project is proceeding on schedule, toward completion in August. At the conclusion of the building project, integration will begin with the installation of the first structures. A detailed status report on the Upgrade will be presented in the next issue of the LLE Review.

### ACKNOWLEDGMENT

This work was supported by the U.S. Department of Energy Office of Inertial Confinement Fusion under Cooperative Agreement No. DE-FC03-92SF19460, the University of Rochester, and the New York State Energy Research and Development Authority. The support of DOE does not constitute an endorsement by DOE of the views expressed in this article.

### REFERENCES

1. R. S. Craxton, Ed., *OMEGA Upgrade Preliminary Design*, Laboratory for Laser Energetics Report DOE/DP 40200-101, University of Rochester (1989).
2. LLE Review **55**, 146 (1993).
3. J. Hunt, W. Simmons, R. Speck, W. Warren, and D. Eimerl, Lawrence Livermore National Laboratory Report UCID-19086 (1981).
4. J. T. Hunt, P. A. Renard, and W. W. Simmons, *Appl. Opt.* **16**, 779 (1977).
5. M. J. Lubin, J. M. Soures, and L. M. Goldman, *J. Appl. Phys.* **4**, 347 (1973).
6. G. J. Linford *et al.*, Lawrence Livermore National Laboratory Laser Program Annual Report 1977, UCRL 50021-77 (1978), pp. 2-142-2-145.
7. J. H. Kelly, M. J. Shoup III, M. D. Skeldon, and S. T. Bui, in *Solid State Lasers II* (SPIE, Bellingham, WA, 1992), Vol. 1410, pp. 40-46.
8. J. H. Kelly, M. M. Tedrow, K. A. Thorp, R. L. Keck, C. T. Cotton, and M. J. Shoup III, "Energy and Active-Wavefront Characterization of a Single Beamline of the OMEGA Upgrade," presented at CLEO '93, Baltimore, MD, 2-7 May 1993.



# **PUBLICATIONS AND CONFERENCE PRESENTATIONS**

## **Publications**

M. M. Cumbo, A. Lindquist, and S. D. Jacobs, "Assessment of Frictional Forces in Optical Polishing Using Atomic Force Microscopy," in *Optical Fabrication & Testing Workshop* (OSA, Washington, DC, 1993), Vol. 24, pp. 118–125.

D. Fried, J. D. B. Featherstone, R. Glens, B. Bordin, and W. Seka, "The Light-Scattering Properties of Dentin and Enamel at 543, 632, and 1053 nm," in the *Proceedings of Lasers in Orthopedic, Dental, and Veterinary Medicine II* (SPIE, Bellingham, WA, 1993), Vol. 1880, pp. 240–245.

T. Gong, L. X. Zheng, W. Xiong, W. Kula, R. Sobolewski, and P. M. Fauchet, "Femtosecond Optical Response of Y-Ba-Cu-O Thin Films: The Dependence on Optical Frequency, Excitation Intensity, and Electric Current," *Phys. Rev. B* **47**, 495 (1993).

D. Gupta, W. R. Donaldson, K. Kortkamp, and A. M. Kadin, "Optically Triggered Switching of Optically Thick YBCO Films," *IEEE Trans. Appl. Supercond.* **3**, 2895 (1993).

P. A. Jaanimagi and D. K. Bradley, "Neutron-Streak and Framing-Camera Diagnostics for ICF Implosions," in *20th International Congress on High-Speed Photography and Photonics* (SPIE, Bellingham, WA, 1992), Vol. 1801, pp. 710–717.

S. D. Jacobs, D. Golini, A. Lindquist, B. Puchebner, M. J. Cumbo, A. Feltz, W. Czajkokowski, J. Greivenkamp, D. T. Moore, and H. M. Pollicove, "Technical Advances in Process Science Research at the Center for Optics Manufacturing," in *International Progress in Precision Engineering*, edited by N. Ikawa, S. Shimada, T. Moriwaki, P. A. McKeown, and R. C. Spragg (Butterworth & Heinemann, 1993), pp. 1046–1050.

S. D. Jacobs, K. Kubath, and A. Maltsev, "Optical Fabrication Laboratory: Introductory Training for Optical Engineering Students," in *Optical Fabrication & Testing Workshop* (OSA, Washington, DC, 1993), Vol. 24, pp. 17–20.

J. Lambropoulos, M. J. Cumbo, and S. D. Jacobs, "The Effects of Material Properties and Process Parameters on Surface Quality during Microgrinding of Glass," in *Optical Fabrication & Testing Workshop* (OSA, Washington, DC, 1993), Vol. 24, pp. 50–53.

A. Lindquist, B. Puchebner, M. M. Cumbo, T. Rich, and S. D. Jacobs, "Bound Abrasive Polisher Concepts for the Center for Optics Manufacturing CNC Machining Centers," in *Optical Fabrication & Testing Workshop* (OSA, Washington, DC, 1993), Vol. 24, pp. 131–133.

C. J. McKinstrie and X. D. Cao, "Nonlinear Detuning of Three-Wave Interactions," *J. Opt. Soc. Am. B* **5**, 898 (1993).

G. M. Shimkaveg, M. R. Carter, B. K. F. Young, R. S. Walling, A. L. Osterheld, J. E. Trebes, R. A. London, R. R. Ratowsky, R. E. Stewart, and R. S. Craxton, "X-Ray Laser 'Oscillator-Amplifier' Experiments," in the *Proceedings of the International Conference on Lasers '92*, edited by C. P. Wang (STS Press, McLean, VA, 1993), pp. 97–104.

M. D. Skeldon and S. T. Bui, "Temporal Pulse-Width Control of a Regenerative Amplifier with Intracavity Etalons," *J. Opt. Soc. Am. B* **4**, 677 (1993).

W. E. Smith, T.-H. Bui, A. Lindquist, and S. D. Jacobs, "Non-Destructive Estimation of Subsurface Glass Damage Using Fluorescent Confocal Microscopy," in *Optical Fabrication & Testing Workshop* (OSA, Washington, DC, 1993), Vol. 24, pp. 148–150.

## Forthcoming Publications

A. I. Lobad, S. M. Mehta, B. C. Tousley, P. J. Rodney, and P. M. Fauchet, "The Starting Mechanism in Coupled-Cavity Mode-Locked Laser Systems," to be published in the *IEEE Journal of Quantum Electronics*.

F. J. Marshall, J. A. Delettrez, R. Epstein, and B. Yaakobi, "Diagnosis of Laser-Target Implosions by Space-Resolved Continuum Absorption X-Ray Spectroscopy," to be published in *Physical Review E*.

P. S. Maruthi Sai, M. J. Levene, T. Gillbro, R. S. Knox, R. H. Hwang-Schweitzer, and S. Mahajan, "Time-Resolved Fluorescence of Phycoerythrocyanin Containing Phycobilisomes from the Cyanobacterium *Westiellopsis Prolifica*," to be published in the *Biophysical Journal*.

R. L. McCrory, J. M. Soures, J. P. Knauer, S. A. Letzring, F. J. Marshall, S. Skupsky, W. Seka, C. P. Verdon, D. K. Bradley, R. S. Craxton, J. A. Delettrez, R. Epstein, P. A. Jaanimagi, R. L. Keck, T. J. Kessler, H. Kim, R. L. Kremens, P. W. McKenty, R. W. Short, and B. Yaakobi, "Short-Wavelength-Laser Requirements for Direct-Drive Ignition and Gain," to be published in *Laser and Particle Beams*.

R. L. McCrory, R. E. Bahr, D. K. Bradley, D. L. Brown, R. S. Craxton, J. Delettrez, R. Epstein, P. A. Jaanimagi, T. Kessler, J. P. Knauer, S. Letzring, F. Marshall, P. W. McKenty, W. Seka, S. Skupsky, J. M. Soures, C. P. Verdon, and B. Yaakobi, "Direct-Drive Implosion Experiments for Laser Fusion on OMEGA and the OMEGA Upgrade," to be published in *Laser and Particle Beams*.

R. L. McCrory, J. M. Soures, C. P. Verdon, T. R. Boehly, D. K. Bradley, R. S. Craxton, J. A. Delettrez, R. Epstein, R. J. Hutchison, P. A. Jaanimagi, S. D. Jacobs, J. H. Kelly, R. L. Keck, T. J. Kessler, H. Kim, J. P. Knauer, R. L. Kremens, S. A. Kumpan, S. A. Letzring, F. J. Marshall, P. W. McKenty, S. F. B. Morse, W. Seka, R. W. Short, M. D. Skeldon, S. Skupsky, and B. Yaakobi, "Direct-Drive Laser Fusion Target Physics Experiments," to be published in the *Proceedings of the 14th International Atomic Energy Agency (IAEA) International Conference on Plasma Physics and Controlled Nuclear Fusion Research*, 30 September–7 October, 1992, Wurzburg, Germany.

R. L. McCrory, "Progress Toward Ignition with Direct Drive," to be published in *Concerning Major Systems in Science and Technology*.

R. L. McCrory, "Direct-Drive Implosion Experiments for Laser Fusion on OMEGA and the OMEGA Upgrade," to be published in the *Proceedings of the 21st ECLIM*, Warsaw, Poland, 21–25 October 1991.

R. L. McCrory, "Irradiation Uniformity Requirements for Direct-Drive Laser Fusion," to be published in the *SPIE Proceedings of the XIV International Conference on Coherent and Nonlinear Optics*, St. Petersburg, Russia, 24–27 September 1991.

C. J. McKinstrie, X. D. Cao, and J. S. Li, "The Nonlinear Detuning of Four-Wave Interactions," to be published in the *Journal of the Optical Society of America B*.

D. D. Meyerhofer, H. Chen, J. A. Delettrez, B. Soom, S. Uchida, and B. Yaakobi, "Resonance Absorption in High Intensity Contrast, Picosecond Laser-Plasma Interactions," to be published in *Physics of Fluids*.

D. D. Meyerhofer and J. Peatross, "Angular Distributions of High-Order Harmonics," to be published in *SILAP (Super-Intense Laser Atom Physics)*.

E. A. Murphy, H. E. Elsayed-Ali, and J. W. Herman, "Superheating of Bi(0001)," to be published in *Physical Review B*.

E. A. Murphy, H. E. Elsayed-Ali, K. T. Park, and Y. Gao, "Temperature-Dependent X-Ray Photoelectron Diffraction of Pb(100): Experimental Results and the Single-Scattering Cluster Model," to be published in the *Journal of Vacuum Science and Technology A*.

J. Peatross and D. D. Meyerhofer, "Novel Gas Target for Use in Laser Harmonic Generation," to be published in *Review of Scientific Instruments*.

## Conference Presentations

D. Golini, M. Atwood, M. Bechtold, W. Czjakowski, A. Feltz, S. D. Jacobs, and A. Lindquist, "Deterministic Microgrinding of Spherical Surfaces on Optical Glasses," ASPE Spring Topical Meeting/Principles of Cutting Mechanics: Applications to Ultra-Precision Machining and Grinding, 13–15 April 1993, Tucson, AZ.

---

The following presentations were made at CLEO '93, Baltimore, MD, 2–7 May 1993:

S. Alexandrou, C.-C. Wang, T. Y. Hsiang, M. Y. Liu, and S. Y. Chou, "7.5-ps Crystalline Silicon Metal-Semiconductor-Metal Schottky Photodiodes."

D. L. Brown, I. Will, W. Seka, and M. Tracy, "Large-Aperture Ring Amplifier with Gains in Excess of 40,000 and Several-Joule Output Capability."

X. D. Cao and D. D. Meyerhofer, "Nonlinear Birefringence of Optical Fibers."

A. Denysenko, R. Sobolewski, S. Alexandrou, C.-C. Wang, T. Y. Hsiang, W. R. Donaldson, D. K. Bradley, and P. M. Bell, "Characterization of Microchannel-Plate Detectors for High-Speed Gated X-Ray Imaging by Electro-Optic Sampling."

J. H. Kelly, M. M. Tedrow, K. A. Thorp, R. L. Keck, C. T. Cotton, and M. J. Shoup III, "Energy and Active-Wavefront Characterization of a Single Beamline of the OMEGA Upgrade."

A. L. Rigatti, D. M. Dudek, R. G. Carnes, L. D. Lund, K. L. Marshall, S. Papernov, A. W. Schmid, D. J. Smith, and S. D. Jacobs, "Uniformity Issues in the Manufacture of Large-Aperture Liquid-Crystal Wave Plates."

M. D. Skeldon, "Generation and Characterization of Fast Rise-Time Pulses on the OMEGA Laser System."

S. Skupsky, "Strategies for Ultra-High Laser Uniformity Using Zero-Correlation Phase Masks."

R. Sobolewski, T. Gong, Y. Kostoulas, W. Xiong, W. Kula, and P. M. Fauchet, "Femtosecond Optical Measurements of the Position of the Fermi Level in Y-Ba-Cu-O Films with Different Oxygen Content."

J. D. Züegel, W. Seka, and G. Gretton, "Tuning a Cr:LiSAF Laser with a High-Efficiency Transmission Grating."

---

T. Gong, P. M. Fauchet, J. F. Young, and P. J. Kelly, "Electron-Hole and Electron Plasmon Interactions Near the Fermi Edge," QELS '93, Baltimore, MD, 2–7 May 1993.

---

The following presentations were made at the 22nd ECLIM, Paris, France, 10–14 May 1993:

R. L. McCrory, "Direct-Drive Target Experiments at the Laboratory for Laser Energetics."

W. Seka, R. S. Craxton, R. E. Bahr, A. V. Chirikikh, D. D. Meyerhofer, A. Simon, and R. W. Short, "Long-Scale-Length Laser-Plasma Interaction Experiments on OMEGA."

S. D. Jacobs, A. Lindquist, M. J. Cumbo, B. Puchebner, A. Feltz, W. Czajkowski, D. Golini, J. Greivenkamp, D. T. Moore, and H. M. Pollicove, "Technical Advances in Process Science Research at the Center for Optics Manufacturing," 7th International Precision Engineering Seminar, Kobe, Japan, 17–21 May 1993.

E. M. Epperlein, "Fokker-Planck Modeling of Electron Transport in Laser Fusion," Workshop on "Collisions: Physical Phenomena and Mathematical Models," Aussois, France, 27–28 May 1993.

S. H. Chen and S. Krishnamurthy, "Some Fundamental Issues Governing Thermotropic Chiral Nematic Copolymers," 42nd Society for Polymer Science, Kyoto, Japan, 31 May–2 June 1993.

-----

The following presentations were made at the 23rd Annual Anomalous Absorption Conference, Wintergreen, VA, 21–25 June 1993:

R. Betti, R. L. McCrory, and C. P. Verdon, "Hydrodynamic Stability of Unsteady Ablation Fronts."

R. Betti, R. L. McCrory, and C. P. Verdon, "Linear Growth Rate of the Ablative Rayleigh-Taylor Instability."

D. K. Bradley, J. A. Delettrez, P. A. Jaanimagi, S. Skupsky, and C. P. Verdon, "Measurements of the Effects of Pulse Shaping on Rayleigh-Taylor Growth in Burnthrough Targets."

A. V. Chirikikh, W. Seka, R. S. Craxton, R. E. Bahr, A. Simon, R. W. Short, E. M. Epperlein, H. Baldis, and R. P. Drake, "Stimulated Brillouin Scattering at 1.053  $\mu\text{m}$  in OMEGA Long-Scale-Length Interaction Experiments."

R. S. Craxton, R. Hoefen, F. S. Turner, C. Darrow, E. F. Gable, and Gar. E. Busch, "Plasma Density Profiles from Grid Image Refractometry."

E. M. Epperlein, "Implicit-Conservative Fokker-Planck Simulations of Heat Flow in Laser Fusion."

R. Epstein, C. P. Verdon, D. K. Bradley, J. Delettrez, F. J. Marshall, and B. Yaakobi, "Simulations of Spectral Signatures and Images of Core-Shell Mixing in Laser-Driven Implosions."

Y. Fisher, H. Chen, B. Soom, and D. D. Meyerhofer, "Suprathermal Electrons and Ions Produced in P-Polarized, Picosecond, Laser-Plasma Interactions."

A. C. Gaeris, R. E. Bahr, R. S. Craxton, W. Seka, and D. D. Meyerhofer, "Measurements of Backscattered Light Near 351 nm in Long-Scale-Length Plasma Experiments on OMEGA."

R. E. Giacone, C. J. McKinstrie, R. Betti, and H. Chen, "The Angular Dependence of Stimulated Brillouin Scattering in Homogeneous Plasma."

C. J. McKinstrie, J. S. Li, R. Betti, and E. A. Williams, "Simple Models of Source Terms Used in the Analysis of Parametric Instabilities."

W. Seka, R. S. Craxton, R. E. Bahr, A. V. Chirikikh, A. Simon, R. W. Short, E. M. Epperlein, H. Baldis, and R. P. Drake, "OMEGA Long-Scale-Length Laser-Plasma Interaction Experiments."

R. W. Short, "A Simple Calculation of the Effects of Beam-Smoothing Techniques on Stimulated Brillouin Scattering."

A. Simon, "Scattering of Laser Light Near  $\omega_0$  Caused by Jets of Accelerated Ions."

M. D. Tracy, E. A. Williams, K. G. Estabrook, and S. M. Cameron. "Eigenvalue Solution for the Ion-Collisional Effects on Ion-Acoustic and Entropy Waves."

---

The following presentations were made at the 9th IEEE International Pulsed Power Conference, Albuquerque, NM, 21–23 June 1993:

W. R. Donaldson and L. Mu, "Stimulating Photoconductive Switches in a Microwave Transmission Line."

D. Gupta, W. R. Donaldson, and A. M. Kadin, "Fast Inductively Coupled Superconducting Opening Switch Triggered by Short Laser Pulses."

---

The following presentations were made at the 6th International Conference on Multiphoton Processes (ICOMP VI), Quebec City, Canada, 25–30 June 1993:

M. Adams, M. V. Fedorov, V. Krainov, and D. D. Meyerhofer, "Comparison of Quasiclassical and Exact Dipole Moments for Bound-Free and Bound-Bound Transitions in Hydrogen."

B. Buerke and D. D. Meyerhofer, "High-Harmonic Generation and the Two-Level Atom."

D. D. Meyerhofer, J. Peatross, and X.-D. Cao, "Minimizing the Phase Mismatch for Laser Harmonic Generation in an Ionization Gas."

D. D. Meyerhofer. "High-Order Harmonics Emitted from Low-Density Gas Targets."

J. Peatross and D. D. Meyerhofer, "Measurement of the Angular Distribution of High-Order Harmonics Emitted from Ionizing Low-Density Gas."

#### ACKNOWLEDGMENT

The work described in this volume includes current research at the Laboratory for Laser Energetics, which is supported by New York State Energy Research and Development Authority, the University of Rochester, the U.S. Department of Energy Office of Inertial Confinement Fusion under Cooperative Agreement No. DE-FC03-92SF19460, and other agencies.

UNIVERSITY OF  
**ROCHESTER**